X-ray Single Photon Imaging Detectors using Superconducting Tunnel Junctions

A Dissertation

Presented to the Faculty of the Graduate School

of

Yale University

in Candidacy for the Degree of

Doctor of Philosophy

by

Liqun Li

Dissertation Director: Professor Daniel Prober

December 2002

Abstract

X-ray Single Photon Imaging Detectors using Superconducting Tunnel Junctions

Liqun Li

Yale University

December, 2002

X-ray detectors based on Superconducting Tunnel Junctions (STJ) provide high energy resolution with good absorption efficiency and imaging capabilities. The energy of an x-ray photon is measured by detecting the excess quasiparticles generated by the absorption of the photon. The number of quasiparticles is measured by the increase in the tunneling current of the STJ. With two STJs attached to the absorber, the x-ray detector is capable of achieving 1-D imaging. We present ways to improve the performance of such 1-D imaging x-ray spectrometers. With better quasiparticle cooling in the tunnel junction, one of our devices shows an energy resolution of 13 eV FWHM for 6 keV x-rays with a spatial resolution of 0.2 μm over a 20 μm range. The noise sources are quantitatively studied for the guidance of future improvements. The measured energy resolution is about twice the theoretical intrinsic energy resolution these detectors can achieve. Three devices with different absorber lengths are measured to study the quasiparticle dynamics in a Ta absorber. By fitting a numerical model to the experimental data, the quasiparticle diffusion constant and lifetime are obtained. These parameters are critical in determining the upper limit of the absorber size. The spatial uniformity of the Ta absorber is also studied. The introduction of a Nb ground contact in the center of the Ta absorber causes spatial non-uniformity in the contact region and leads to extra energy broadening. Using Ta as a ground contact to the Al trap eliminates this problem. In searching for 2-D imaging detectors, we propose using four-junction detectors. Simulations have been done on detectors that consist of a square absorber and four junctions on the sides or four junctions in the corners. Comparison shows that the detector with four junctions on the sides has better spatial performance.

Acknowledgement

As I finished the last page of my thesis, I was surprised by all the work that has been done in my six years of the Ph.D research. Without the help and support from my colleagues, I cannot have this much achievement.

First I thank my advisor Prof. Daniel Prober for his guidance through my research. He always encouraged me to have new ideas and gave me enough free space to work and to solve the problems independently. His optimism and confidence always supported me to pursue the best no matter in my research or in real life. His persistence in understanding the unknown phenomena helped me work hard to find out the explanation. Even though the experimental results are important, the research ability is the most precious gift that Dan was trying to lead me to possess.

I also thank my thesis committee members: Richard Chang, Rob Schoelkopf, Douglas Stone, and Andy Szymkowiak. I was very impressed by Prof. Richard Chang's thorough consideration from all aspects. He gave me a broader view of the photon detectors. Prof. Douglas Stone's deep insights to the physics of the problems helped me study them more carefully. Prof. Rob Schoelkopf's rich experience in the electronics and cryogenics helped me a lot too. I enjoyed the discussion with him about the quantum phenomena, which was very interesting and enlightening. Prof. Andy Szymkowiak gave me great support on this research work, especially his direction and inspiration.

I had a great time working with Luigi and did many experiments side by side with Chris Wilson. It was so much fun to discuss with them on broad subjects such as geology, politics, tradition, cultural difference, etc. during the boring cool-down time. We also had countless discussions about the measurements that helped me gain deeper understanding. They fabricated the x-ray devices that are presented in this thesis.

A lot of friends on the fourth floor in Becton brought me sunshine and smile. They let me forget all the frustration and worries met in the research. They made my life in Yale so delightful. I give my thanks to all of them: Veronica Savu, Jim Schuck, Lafe Spietz, Irfan Sidiqi, Aric Sanders, Matthew Reese, Alex Kozhevnikov, Qiang Wu, Minghao Shen, and other good friends: Min Qi, Zhiyong Duan, Jingpin Han, etc. I want to express my great appreciation to the staff at Yale, who were always there to help me from filling forms to placing orders.

Finally I would like to thank my parents and my husband, who give me so much love and support to get through the tough time of my research. Especially my husband Shichang has always been a source of strength and inspiration. I could not have this thesis work done without them. This thesis is dedicated to them.

Table of Contents

Acknowledgement i

Table of Contents iii

List of Figures vi

List of Tables ix

List of Symbols and Abbreviations x

Chapter 1 Introduction 1

1.1 Motivation 1
1.2 Current State of Research 2
1.3 Brief Review of Previous Work in this Group 4
1.4 This Thesis Work and Organization 5

Chapter 2 Theory of SIS Tunnel Junction Detectors 7

2.1 Physics of X-ray Detection 8
2.1.1 Quasiparticle Generation 9
2.1.2 Quasiparticle Recombination 10
2.1.3 Quasiparticle Diffusion 11
2.1.4 Quasiparticle Trapping and Scattering 11
2.1.5 Quasiparticle Tunneling (Back-tunneling) 12
2.1.6 Quasiparticle Outdiffusion 16
2.2 Josephson Effects 17
2.2.1 Critical Current 17
2.2.2 Fiske Resonance Modes 19
2.2.3 Annular Junction 21
2.3 STJ Detector Device Noise Sources 23
2.3.1 Quasiparticle Creation Noise 23
2.3.2 Absorber Loss 23
2.3.3 Trapping Multiplication 24
2.3.4 Backtunneling 24
2.3.5 Cancellation 25

Chapter 3 Device Fabrication and Experimental Setup 26

3.1 Device Materials and Fabrication 26
3.1.1 Absorber – Ta 27
3.1.2 Tunnel Junction – Al 28
3.1.3 Ground Contact – Nb or Ta 29
3.1.4 Substrate – SiO_2 on Si 29
3.2 Cryogenic Setup 30
3.3 DC and AC Electronics 33

Chapter 4 Optimization of Al Junctions 38

4.1 Junction Geometry Design 38
  4.1.1 Quartic and Diamond Shaped Junctions 40
  4.1.2 Annular Junctions 43
4.2 Improving Junction Performance 48
  4.2.1 Problems of Device A 48
    4.2.1.1 Incomplete Cooling 49
    4.2.1.2 Johnson Noise of the Feedback Resistor 52
    4.2.1.3 Shot Noise of the Junctions 52
  4.2.2 Junction Improvement — Device B 53
    4.2.2.1 The Junction Design of Device B 54
    4.2.2.2 The Performance of Device B 54
    4.2.2.3 Noise Source Analysis 57

Chapter 5 Non-equilibrium Quasiparticle Dynamics in the Ta Absorber 70

5.1 Spatial Uniformity 70
  5.1.1 Spatial Non-uniformity Caused by the Nb Contact 70
  5.1.2 Spatial Uniformity with Ta Ground Contact 73
  5.1.3 Spatial Resolution 76
5.2 Device Modeling 78
  5.2.1 Quasiparticle Diffusion in the Ta Absorber 78
  5.2.2 Quasiparticle Tunneling in the Al Junction 80
5.3 Experimental Results 82
  5.3.1 Charge Fitting 83
  5.3.2 Diffusion Constant and Lifetime 92
  5.3.3 Discussion 97

Chapter 6 Four-Junction Devices 100

6.1 The Quasiparticle Diffusion Process 100
6.2 Design with Junctions on Each of the Four Sides 101
6.3 Design with Junctions in Each of the Four Corners 104
6.4 Summary 105

Chapter 7 Long Decay of the Pulses 107

7.1 Characters of the Long Decays 108
7.2 Constrained Slow Out-Diffusion 109
7.3 Qualitative Study of the Slow Decay 111
7.4 Quantitative Study of the Slow Decay 112

Chapter 8 Other Device Issues and Perspectives 116

8.1 The Effects of Substrate Events 116
8.2 Backtunneling Device 122
8.3 Controlled Out-Diffusion 128
8.4 STJ Detectors Perspective 128

Appendix A: Device Parameters 132

Appendix B: Summary of Important Runs 134

Appendix C: Related Experimental Data Analysis 136
Appendix D: Substrate Event Effect and Count Rate 139
Bibliography 140

List of Figures

2.1. The schematic I-V curve of a superconducting tunnel junction 7
2.2. The quasiparticle processes in the detectors 9
2.3. Four tunneling processes of SIS junctions using semiconductor representation 13
2.4. Four tunneling processes of SIS junctions using excitation representation 15
2.5. The theoretical $I_c(H)$ for rectangular, diamond, and quartic junctions 18
2.6. $I_c(H)/I_c(0)$ vs. Φ/Φ_0 for an annular junction (r/R = 1/5) 21

3.1. The cross section of the device with a junction on the left side 26
3.2. The experimental setup and data acquisition instruments 31
3.3. Laser detrapping setup 32
3.4. Active voltage bias circuit with a AC current amplifier 35

4.1. I-V curves with and without trapped flux 39
4.2. I-V curves of quartic shaped and diamond shaped junctions 42
4.3. Schematic of the annular STJ with a single trapped flux 43
4.4. I-V characteristics of the annular STJ with and without a trapped flux 45
4.5. I_c vs. H of the annular STJ 46
4.6. The schematic of the electronic circuit with the electronic noise sources 49
4.7. Q_{total} vs. V_{bias} for completely and incompletely cooled quasiparticle system 50
4.8. I_{peak} vs. V_{bias} for completely and incompletely cooled quasiparticle system 51
4.9. The top views of device A and device B 53
4.10. Q_1 vs. Q_2 of device B 54
4.11. Q_{total} vs. x of device B 55
4.12. The energy spectrum over a 20×100 μm^2 range 56
4.13. ΔE^2 vs. i_n^2 of injection test for device B 61
4.14. The current noise spectra with warm and cold feedback resistor 63
4.15. I_{peak} vs. V_{bias} of device B 64
4.16. The circuit to measure the R_d of the junction 65
4.17. ΔE^2 vs. the square of the voltage noise of the series resistor $e^2_{n\_series}$ 65

4.18. Q_{total} vs. V_{bias} of device B 66
4.19. The 1/f noise of the amplifier 67

5.1. Location dependence of energy resolution for device A and B 71
5.2. Total charge as function of location for device A and device B 72
5.3. Energy histogram from the center and one side of device B 73
5.4. Device C with a Ta contact connected to the trap of one junction 74
5.5. The total collected charge vs. x-ray event location for device C 75
5.6. Energy histogram from the center of device C 75
5.7. Three devices with different absorber lengths 83
5.8. Q_1 vs. Q_2 for three devices with different lengths 85
5.9. Q_1 vs. Q_2 with uniform loss and a point Nb loss in the Ta 87
5.10. The loss parameter α as a function of the absorber length L 88
5.11. Q_1 vs. Q_2 of two devices and their fitting with and without the Nb loss 89
5.12. The current pulses at different locations of the three devices 91
5.13. The current pulses of one x-ray event and their fittings 94
5.14. Delay time vs. I_{peak} for all three devices 95
5.15. I_{peak1} vs. I_{peak2} for all three devices 96

6.1. The designs with junctions on each side and at each corner 101
6.2. Q_1/Q_0 collected in trap 1 with junctions on 4 sides vs. position (x,y) 102
6.3. The spatial resolution of the device with junctions on 4 sides 103
6.4. Q_1/Q_0 collected in trap 1 with junctions on 4 corners vs. position (x,y) 104
6.5. The spatial resolution of the device with junctions on 4 corners 105

7.1. The pulses from device A, B and C 107
7.2. The long decay of the pulses scales with the collected charge 108
7.3. The long decay of the pulses scales with the junction area 109
7.4. The current pulses of a photon event in the wiring pad 110
7.5. The wiring structure of device A and C 111
7.6. The wiring pad configuration used in the simulation 112
7.7. The simulation result of quasiparticle out-diffusion 113

8.1. Q_{total} vs. x of the 500 μm long device with different count rates 117
8.2. ΔE^2 vs. square of the count rate for the 500 μm long device 118
8.3. The histogram of device B and the 500 μm long device 119
8.4. The energy diagrams and cross sections of backtunneling devices 122
8.5. The I-V curve of the backtunneling device 124
8.6. The macroscopic model of the self-heating I-V curves 126

List of Tables

Table 4-1 Estimate of the first Fiske mode of diamond shaped junctions 41
Table 4-2 Device noise sources for device B and device A 60
Table 4-3 List of all the noise contributions in devices A and B (FWHM) 68

Table 5-1 Energy and spatial resolution vs. x of devices A, B and C 77
Table 5-2 Physical parameters of the three devices with different absorber lengths 83
Table 5-3 The loss parameter of quasiparticles in the Ta 87
Table 5-4 The diffusion constant and the lifetime of quasiparticles in the Ta 94

Table 8-1 Future prediction of device improvement 130

List of Symbols and Abbreviations

α	Loss parameter
β	A measure for the relative time scales of trapping and loss
β	the fraction of quasiparticle lost
c	Speed of light
C_f	Feedback capacitor
d	Insulating barrier thickness
d_{Al}	Al film thickness
d_{Ta}	Ta film thickness
Δ_1	Energy gap in the left electrode
Δ_2	Energy gap in the right electrode
Δ_{Al}	Al energy gap
Δ_{Nb}	Nb energy gap
Δ_{Ta}	Ta energy gap
Δ	Energy gap
D	Diffusion constant
D_{Al}	Aluminum diffusion constant
D_{eff}	Effective tantalum diffusion constant in non-equilibrium state
D_N	Tantalum diffusion constant in normal state
D_{sc}	Theoretical diffusion constant in superconducting state
$\Delta E_{amplifier}$	Energy width of electronic noise
ΔE_{β}	Energy width caused by quasiparticle loss
ΔE_{back}	Energy width caused by backtunneling
ΔE_{create}	Charge creation fluctuation energy width
ΔE_{device}	The energy width due to the device source
ΔE_{FWHM}	Full Width at Half Maximum energy resolution
ΔE_{γ}	Energy width caused by cancellation
ΔE_{multi}	Energy width caused by trapping multiplication

ΔE_{qusnt}	The energy width due to the electronic noise at quiescent state
ΔE_{source}	The energy width of the x-ray source
ΔE_{total}	Total energy width
ΔV	Bias voltage fluctuation
ΔV_{rms}	The RMS of the bias fluctuation
e	Electron. elementary charge (1.6×10^{-19} C)
e_n	Voltage noise density
ε	Effective quasiparticle creation energy
E	Quasiparticle energy
E_x	X-ray photon energy
f	Frequency
F	Fano factor
F_{eff}	Effective Fano factor
Φ	Magnetic flux
Φ_0	A flux quantum
FET	Field Effect Transistor
FWHM	Full Width at Half Maximum
γ	Cancellation factor
G	Effective backtunneling factor
G_{amp}	Amplifier open loop gain
G_{nn}	Normal state conductance of the tunneling barrier
Γ_r	Quasiparticle loss rate per unit density
h	Plank constant
I	Current
$I_c = I_c(0)$	Critical current. maximum supercurrent
I_{int}	Interface current
i_n	Amplifier current noise density
$i_{n,J}$	Johnson noise of the feedback resistor
$i_{n,s}$	Shot noise of subgap current
I_{nn}	Tunneling current of NIN junction

$I_s = I_c(H)$	Supercurrent as function of magnetic field
φ	Phase of the Ginzburg-Landau wave function
$J_c(x,y)$	Josephson critical current density
$J_n(x)$	*n*th Bessel function
K	Kelvin
κ	Trapping multiplication factor
K_α	Manganese emission duplet lines at 5895 eV
$\mathrm{K}_{\alpha1}$	Manganese emission duplet line at 5899 eV
$\mathrm{K}_{\alpha2}$	Manganese emission duplet line at 5888 eV
K_β	Manganese emission singlet line at 6490 eV
k_B	Boltzmann constant
k_I	Ratio of the energy resolution to the current noise
k_V	Ratio of the energy resolution to the voltage noise
λ	London penetration depth
L	Length of the Ta absorber. the length of the rectangular junction
λ_J	Josephson penetration depth
L_{trap}	Effective trapping length
n_{th}	Quasiparticle thermal density
N	Number of quasiparticles
N_0	Initial number of created quasiparticles
$N_1(0)$	Densities of states at Fermi surface in the left electrode
$N_{1s}(E)$	Density of states of the superconductor in the left electrode
$N_2(0)$	Densities of states at Fermi surface in the right electrode
$N_{2s}(E)$	Density of states of the superconductor in the right electrode
N_{ce}	Number of quasiparticles in the counterelectrode
N_{create}	Number of quasiparticles created
N_{loss}	Average loss quasiparticle number
N_{multi}	Number of Cooper pairs that are broken by trapping multiplication
N_{rev}	Number of tunneling events that transfer charge in reverse direction
N_σ	Single spin density of states at the Fermi level
N_{trap}	Number of quasiparticles in the trap

N_x	Number of excess quasiparticles
P_1	Probability of quasiparticle tunneling from trap to counter-electrode
P_2	Probability of quasiparticle tunneling from counter-electrode to trap
Q_1	Charge collected in junction 1
Q_2	Charge collected in junction 2
Q_{total}	Total collected charge from both junctions
ε_r	Relative dielectric constant
R	Recombination rate per unit density of quasiparticles
r	Inner radius of the annular junction
R^*	Outer radius of the annular junction
R_{bias}	Bias resistor
R_d	Dynamic resistance
R_f	Feedback resistor
ρ_N	Resistivity of the Ta film in normal state
R_{nn}	Resistance of the tunneling barrier
RRR	Residual resistance ratio
R_s	Series resistor
T_{12}	Tunneling matrix
T_c	Critical temperature of the film
τ_0	Material dependent characteristic time
τ_{loss}	Quasiparticle effective lifetime in the Ta absorber
τ_{out}	Outdiffusion time
τ_s	Quasiparticle scattering time
τ_{trap}	Tapping time in the Al
τ_{tun}	Tunnel time
$\tau_{tun.\ ce}$	Tunnel time from the counterelectrode
$\tau_{tun.\ tr}$	Tunnel time from the trap
$\tau_{tun.NIN}$	NIN junction tunnel time
$\tau_{tun.SIS}$	SIS junction tunnel time
V_{bias}	Bias voltage

V_{bias}	Bias voltage
V_{nm}	Fiske resonant voltage
Vol	Volume of the superconductor
Ω	Phonon energy
W	Width of the rectangular junction
Ω_{max}	Maximum phonon energy
Ω_{min}	Minimum phonon energy
x_0	Absorption location
ξ_{Al}	Al coherence length
ξ_{Ta}	Ta coherence length
$\bar{n}$	Average quasiparticle tunneling number
$N(E_i - \Omega)$	Density of the final electron states and the integral is taken over all possible phonon states.
$\bar{c}$	Electromagnetic wave velocity for a barrier

Chapter 1 Introduction

In recent years there has been tremendous research interest in low temperature detectors. One obvious advantage of working at cryogenic temperatures is the ability to achieve lower noise and better performance. One type of cryogenic detector is based on the superconducting tunnel junctions (STJ). This type of detector is designed to detect single photons in the energy range from a few eV up to ~10 keV. Not only can they measure the energy of each photon with high resolution, but they can also provide timing information for each photon. Moreover, imaging can be done with strip structure STJs [Kraus, 89], or with a four-junction detector [den Hartog, 00], or with an STJ array [Rando, 98].

1.1 Motivation

Different types of telescopes detect light of different wavelengths – ranging from microwaves to visible light to high energy x-ray photons and gamma rays. Each wavelength band is important to compose a full view of the universe. Optical telescopes, such as the Hubble Space Telescope, bring us brilliant images of remote stars and galaxies, while the most energetic explosion since the 'Big Bang' has been discovered by the high energy gamma-ray telescopes. In between the gamma-ray and the visible light detectors, x-ray detectors have become indispensable members of the detector family. With the development of all these detectors to cover the entire spectral range, astronomers are ready to study the evolution of the universe.

The opaqueness of the Earth's atmosphere to extraterrestrial x-rays poses challenges for astronomers. CCD detectors have been successfully sent into the outer space for doing x-ray imaging [Charles, 95], but they do not provide the necessary energy resolution. The ultimate goal of the x-ray telescope, which is going to be the core of the next generation x-ray observatory, is to measure the photon energy and timing information as well as to implement imaging. The excellent energy resolution that our STJ detectors can provide for x-ray photons is necessary for the study of black holes, active galactic nuclei, the life cycles of matter and energy in the universe, galaxy clusters and dark matter [Charles, 1995].

In the Chandra X-ray Observatory [Tucker, 01], an array of CCDs is used to implement high angular resolution and high detection efficiency for x-rays. But the energy resolution of the CCD detector is quite poor, ~100 eV for 6 keV x-ray photons. Compared with the CCD type detectors, the advantage of superconducting tunnel junction detectors (STJ) is its higher energy resolution, which is theoretically predicted to be ~3 eV (Section 2.3.1), a factor of 30 better than the one offered by the CCD detector. The STJ detector can also provide timing information for x-ray photons with a resolution better than a microsecond, which can be used to study pulsars. Therefore STJ detectors are one of the ideal candidates for future x-ray observatories. Other novel applications such as material analysis and fluorescence spectra of proteins in biophysics using low temperature detectors have also started to attract increasing attention [Hilton, 99; Friedrich, 02].

STJ detectors can provide not only high energy resolution, but also imaging. Using arrays of STJs to achieve imaging introduces difficulties in the design of electronic readouts (one readout setup per pixel/STJ). The power consumption, complexity, and heat dissipation of the amplifiers in the cryogenic environment become technical challenges for low temperature detectors working in outer space. On the contrary, our design uses a strip structure to implement one-dimensional (1-D) imaging with one STJ on each end of the detector. It only needs two electronic readouts. This can be easily expanded to 2-D imaging by using four STJs, one on each side of a square x-ray absorber. Such 2-D imaging design can be easily implemented by just four electronic readouts instead of n^2, where n^2 is the number of the pixels for an n by n array. Thus a four junction 2-D imaging detector would greatly simplify the electronic setup.

1.2 Current State of Research

A variety of cryogenic detectors have been developed to achieve high energy resolution for 1 to 10 keV x-ray photons. The three most important ones are microcalorimeters, transition edge sensors, and STJ detectors.

Microcalorimeters measure the temperature increase of the absorber after the absorption of an x-ray photon. The NASA/Wisconsin group developed the first detector with an energy resolution of 7.3 eV for the 6 keV photons using doped silicon thermometers with a HgCdTe absorber [McCammon, 91]. The intrinsic energy resolution of such detectors is determined by the thermodynamic fluctuations of temperature. The long thermal relaxation time of about a few milliseconds in the microcalorimeters limits the count rate of the detector.

Transition edge sensors (TES) are made of a metal absorber connected to a special thermometer. The thermometer is a superconductor having normal-superconductor bilayer structure and biased at its transition temperature. Using the superconducting transition edge bolometers, the group at NIST Boulder successfully measured an energy resolution of 4.5 eV for the 6 keV photons [Irwin, 99]. Because they use a thermal feedback technique, the thermal decay time of the absorber is greatly reduced to about 200 μs. However, the decay time is still far too long to achieve high count rate.

STJ detectors detect either phonons or quasiparticles created by the absorption of a single x-ray photon in the absorber. For the phonon creation type of detector the absorption of the x-ray photon creates energetic phonons in the absorber. The phonons diffuse from the absorber to the electrode of the tunnel junction, and those with energy above 2Δ break Cooper pairs and create quasiparticles in the STJ electrode. The STJ detector measures the quasiparticle tunneling current through the junction. The best measured energy resolution for this type of detectors is 12 eV [Angloher, 01]. They also have the problem of a long decay time of about 100 μs.

The quasiparticle creation type of STJ detectors measure the number of the quasiparticles directly created by the absorption of x-ray photons in the absorber. The energy resolution is intrinsically limited by the quasiparticle creation statistics inside the absorber. The theoretical limit for a Ta absorber is ~3 eV for the 6 keV photons, while that for Nb is ~4.2 eV (Section 2.3.1). Using the Nb based stack STJ detector the best measured energy resolution is 29 eV [Frank, 96; Mears, 96]. The count rate of the Nb based stack STJ detector can reach 10 kHz without degradation of the detector performance [Labov, 98].

The devices analyzed in this thesis use Ta as the x-ray photon absorber and an Al tunnel junction as the quasiparticle detector. The best energy resolution we have achieved is 13 eV FWHM (full-width-at-half-maximum) for the 6 keV photons [Li. 01a]. The response time of the quasiparticle detectors is much faster than that of the phonon detectors. For an absorber size of 200 x 100 μm^2 or 500 x 100 μm^2, the decay time of the tunneling current pulses is about 10 to 20 μs. The detectors we developed also implement 1-D imaging with only two readout channels. The theoretical spatial resolution of the detector is approximately 0.5 μm for a 200 μm long absorber.

1.3 Brief Review of Previous Work in this Group

X-ray detector research has been going on for the past 10 years in this group. We have made tremendous achievements in developing better measurement electronics, in improving device performance, and in understanding the device physics.

Michael Gaidis started the research work at Yale in STJ x-ray detectors. In his thesis [Gaidis, 94] he explored the physics of the detector and successfully designed and fabricated STJ detectors [Gaidis, 93]. The fabrication procedure, which we still follow today, can produce very good detectors. He also designed a current bias and charge amplifier electronics and did the cryogenic testing. His devices were made of a 200 μm long Ta absorber laterally connected by one Al tunnel junction to one side. He was able to achieve an energy resolution of 190 eV FWHM for the 6 keV x-ray photons.

Stephan Friedrich did the first testing of a two- junction detector [Friedrich, 97b]. He designed a DC active voltage bias and a current amplifier, which allowed more stable voltage biasing and lowered the energy broadening caused by the electronic noise from 45 eV down to 13 eV when there is no x-ray events [Friedrich, 97a]. The two-junction detector provided an improved energy resolution of 54 eV over a 30 μm range of the absorber. The best energy resolution of the detector was measured at points very close to the side of the absorber, while the worst energy resolution was in the center. This was believed to be caused by the Nb ground contact in the center of the Ta absorber. The diffusion constants of Ta and Al were successfully extracted from the two-junction detector [Friedrich, 97c].

Kenneth Segall continued Friedrich's work with more extensive modelling and testing of the same device. He found out two main noise sources that limit the energy resolution [Segall, 00b]. He further improved the energy resolution of the device to 26 eV over a 20 μm range near the edge of the absorber [Segall, 99]. He also measured the excess noise due to incomplete quasiparticle cooling and quantitatively explained the noise sources of the 26 eV energy broadening [Segall, 00a].

1.4 This Thesis Work and Organization

The major achievements of the present work are several large improvements in detector performance and measurement methodology. The quasiparticle dynamics in the Ta absorber are also studied. Based on the current research results we offer some suggestions for future improvements.

In Chapter 2 we review the basic working principles of superconducting tunnel junction detectors and quasiparticle dynamics theory. An introduction to some intrinsic noise sources of the detector is presented.

In Chapter 3 we introduce the experimental set-up and give a brief review of the device fabrication and its effects on the detector performance.

Chapter 4 discusses the processes involved in the optimisation of the Al junction design. The first part describes how the junction geometry and size affect the detector performance. The I-V curves for the junctions with different geometries are compared. A novel junction design, the annular junction is also presented [Frunzio, 01]. The interesting feature of the annular junction is the implementation of x-ray detection without applying a magnetic field.

In the second part of Chapter 4 we introduce a new device (device B). This device utilizes better quasiparticle cooling to significantly reduce two dominant noise sources that were present in the device designed by Friedrich (device A). In addition, by cooling the feedback resistor, the electronic noise is also dramatically reduced. The best energy resolution is improved significantly – by a factor of two over that of device A [Li, 01a]. The noise sources of device B are carefully studied and quantified to provide useful information on future improvements [Li, 01b].

In Chapter 5 we first discuss the spatial non-uniformity of the Ta absorber caused by the Nb contact and its solution [Li, 01b; Li, 02a]. We then study the quasiparticle non-equilibrium dynamics in the Ta film [Li, 02a]. Two parameters, the diffusion constant and the lifetime of quasiparticles, are derived by fitting the experimental results [Li, 02b]. Their comparisons with theoretical values and their effects on astronomy applications are also discussed.

The simulation of 4-junction detectors with 2 different configurations for 2-D imaging [Li, 00] is presented in Chapter 6. By assuming constant electronic noise, we compare the spatial resolution performance for the two different configurations. The device with four junctions on the sides of the Ta absorber shows better spatial performance than that with four junctions in the corners.

In Chapter 7 we discuss the long decay time of the pulses in device B. It is caused by a narrow lead connected to the wiring pad that constrains the quasiparticle outdiffusion. The long decay time limits the count rate of the devices. But it can be solved by changing the wiring design.

In Chapter 8 we discuss the effects of substrate events and backtunneling on the detector performance. We conclude that the lateral backtunneling device is not a good candidate for future energy resolution improvements because of self-heating and the low frequency noise due to thermal quasiparticle fluctuations [Wilson, 01]. We offer a general outlook for the future development of STJ detectors and what could be the best possible performance of the x-ray single photon imaging STJ detectors.

Chapter 2 Theory of SIS Tunnel Junction Detectors

The phenomenon of superconductivity was first discovered by Kamerlingh Onnes in 1911. He observed the disappearance of the electrical resistivity of mercury when its temperature was below a characteristic temperature T_c. After almost half a century Bardeen, Cooper and Schreiffer (BCS) [Bardeen, 57] came up with an explanation for the superconductivity phenomenon. In certain metals when temperature is below T_c, electrons are condensed into bound Cooper pairs at the Fermi surface by an attractive phonon mediated interaction. The least energy required to break a Cooper pair and generate two quasiparticles is 2Δ, where Δ is the energy of the lowest quasiparticle energy level relative to the Fermi surface, typically referred to as the energy gap of the superconductor.

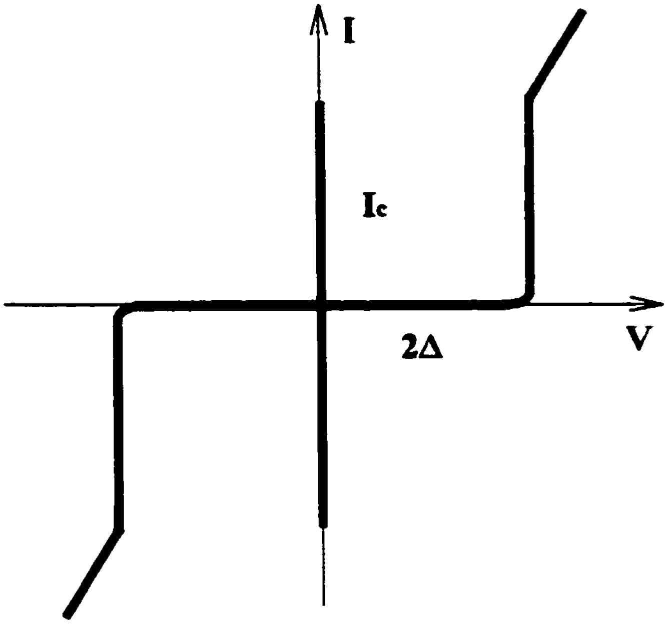

Fig. 2.1 The schematic I-V curve of a SIS tunnel junction with no magnetic field. The current at zero bias voltage is a dc Josephson current.

A superconducting tunnel junction (STJ) is formed by two superconducting electrodes separated by a thin insulator layer. The quasiparticles in one of the superconducting electrodes can tunnel through the insulator layer into the other electrode and give rise to a tunneling current. The schematic I-V curve of a STJ is shown in Fig. 2.1. When the bias voltage applied between electrodes is below twice the energy gap voltage $2\Delta/e$, only the thermally excited quasiparticles can tunnel through and contribute to the tunneling current. When the bias voltage is higher than $2\Delta/e$, there is a sharp increase in the tunneling current caused by Cooper pair breaking and the divergent density of states. When the bias voltage increases further, the I-V curve asymptotically approaches that of the junction in the normal state. The Cooper pairs can also tunnel through the barrier. This is the so-called Josephson effect [Josephson, 62]. The Cooper pair tunneling gives rise to a *dc* supercurrent at zero bias voltage that can be modulated by magnetic fields applied parallel to the tunnel barrier. More details of the superconductor-insulator-superconductor (SIS) theory can be found in Refs. [Van Duzer, 81; Tinkham, 96].

2.1 Physics of X-ray Detection

Our 1-D imaging STJ detectors have a Ta absorber with a superconducting tunnel junction connected to each end. The Al layer that is directly connected to the absorber servers as a quasiparticle trap. Once an x-ray photon is absorbed in the Ta layer, it breaks Cooper pairs and creates millions of quasiparticles that diffuse towards the ends of the Ta absorber. After reaching the Al trap, they scatter down to lower energy levels by emitting phonons and are trapped inside the Al trap. After tunneling through the insulator barrier, the quasiparticles will either tunnel back into the trap or diffuse out into the wiring pads, leaving the junction region. During the whole processes, some of them may recombine into Cooper pairs. Fig. 2.2 depicts many possible quasiparticle processes in our STJ detectors.

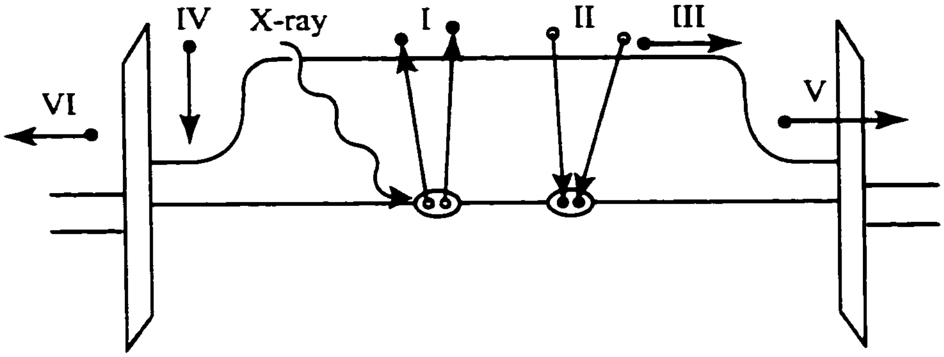

Fig. 2.2 The energy band diagram of the 1-D imaging STJ detector. The quasiparticle processes in the detector are: (I) quasiparticle generation, (II) quasiparticle recombination, (III) quasiparticle diffusion, (IV) quasiparticle trapping, (V) quasiparticle tunnelling, (VI) quasiparticle outdiffusion from the junction.

2.1.1 Quasiparticle Generation

When an x-ray photon is absorbed in the Ta superconducting absorber, a few energetic photoelectrons are created. As the photoelectrons travel through the Ta absorber, they lose their energy by exciting electrons along the path through Coulomb interaction on a very short time scale (~10^{-15} second) [Chi, 81]. These electrons in turn excite more electrons. After the cascade process the energy is shared among many electrons. Once the average energy of the electrons is comparable to the Debye energy, phonons start to join the relaxation process to cool down the excited electrons. Thus the energy of the x-ray photon relaxes into low energy quasiparticle excitations and phonons by electron-electron, electron-phonon interaction and phonon pair breaking process in about a hundred picoseconds [Friedrich, 97]. In the relaxation process, approximately 60% of the incident photon energy is converted into the energy of the quasiparticle system, while the rest is lost to the subgap phonon system [Kurakado, 82]. The number of quasiparticles that are created, N_{create}, is equal to the x-ray energy E_x divided by the effective excitation energy ε.

$$N_{create} = \frac{E_x}{\varepsilon}. \tag{2.1}$$

The effective excitation energy $\varepsilon \approx 1.74\,\Delta$ was first calculated in [Kurakado, 82] using Monte Carlo simulations. ε is larger than Δ because part of the photon energy, about 40%, is lost into the phonon system.

2.1.2 Quasiparticle Recombination

Excess quasiparticles in a non-equilibrium system will eventually recombine into Cooper pairs so that the system can go back to equilibrium. The characteristic time of the recombination process is the quasiparticle lifetime. If the number of excess quasiparticles injected into a superconducting film is small, the number of quasiparticles will decay exponentially. The non-equilibrium state created by the absorption of an x-ray photon has a large number of excess quasiparticles. For such a state far from equilibrium, there are $N(N-1)/2 \sim N^2/2$ ways to recombine quasiparticles into Cooper pairs out of N quasiparticles. If we define $\boldsymbol{R}$ to be the recombination rate per unit density of quasiparticles, the recombination rate of quasiparticles is then

$$\frac{\partial N}{\partial t} = -N(N-1)\frac{R}{Vol} \approx -N^2\frac{R}{Vol}, \tag{2.2}$$

where $\boldsymbol{Vol}$ is the volume of the superconductor. The factor of $1/2$ is lost because each recombination event eliminates two quasiparticles. We can identify the quasiparticle loss rate per volume due to quasiparticle recombination as

$$\Gamma_r = -\frac{\partial n}{\partial t} = -\frac{\partial(n_{th} + N_x/Vol)}{\partial t} \approx \left(2N_x n_{th} + N_x^2/Vol\right)\frac{R}{Vol}, \tag{2.3}$$

where n_{th} is the thermal quasiparticle density and N_x is the number of excess quasiparticles. The first term represents the excess quasiparticles recombining with the background thermal quasiparticles, called the quasiparticle thermal loss. The second term represents the self-recombination among the excess quasiparticles themselves, which is called the quasiparticle self-recombination loss. n_{th} is given by [Eisenmenger, 81]

$$n_{th} = 2N_\sigma\sqrt{2\pi\Delta k_B T}\,e^{-\Delta/k_B T}, \tag{2.4}$$

where N_σ is the single spin density of states at the Fermi level and k_B is Boltzmann constant. The recombination rate constant $\boldsymbol{R}$ can be then calculated theoretically from [Kaplan, 76; Eisenmenger, 81]

$$R = \left(\frac{2\Delta}{k_B T_c}\right)^3 \frac{1}{4N_\sigma \Delta \tau_0}, \qquad (2.5)$$

where τ_0 is a material dependent characteristic time and depends on the strength of the electron-phonon coupling. [Kaplan, 76] has calculated τ_0 for several materials.

When two quasiparticles recombine, they emit a phonon with energy at least 2Δ. These phonons may break Cooper pairs and recreate quasiparticles unless they escape into the substrate or decay anharmonically. This effect is called the phonon trapping [Cray, 71]. It can enhance the quasiparticle lifetime significantly. Considering the trapping effect, the effective lifetime of the quasiparticles created by x-ray photons in the Ta absorber is estimated to be about a few milliseconds [Gaidis, 94].

2.1.3 Quasiparticle Diffusion

Inside the superconducting Ta absorber quasiparticles propagate through diffusion. The quasiparticle mean free path (tenths of microns) is much smaller than the typical device dimensions (> 200 μm), so if there is no edge loss the one-dimensional diffusion equation can be used to describe the dynamics of quasiparticle distribution $n(x,t)$ inside the Ta film.

$$\frac{\partial n(x,t)}{\partial t} - D\frac{\partial^2 n(x,t)}{\partial x^2} = -\frac{n(x,t)}{\tau_{loss}}, \qquad (2.6)$$

with the following initial condition

$$n(x,t=0) = N_0 \delta(x - x_0). \qquad (2.7)$$

where D is the diffusion constant of the quasiparticles. τ_{loss} is the quasiparticle effective lifetime in the Ta absorber, and N_0 is the initial number of created quasiparticles.

2.1.4 Quasiparticle Trapping and Scattering

After quasiparticles with energy higher than the Ta gap energy Δ_{Ta} diffuse from the Ta absorber into the Al trap, they scatter down inelastically to lower energy levels in the Al trap by phonon emissions. Once the quasiparticle energy is lower than Δ_{Ta}, they are trapped in the Al. The expression for such quasiparticle scattering rate can be derived from Fermi's Golden Rule. For an electron with energy E in the limit of zero temperature the scattering rate is [Kaplan, 76]

$$\frac{1}{\tau_s}=\frac{1}{\tau_0}\left(\frac{1}{k_B T_C}\right)^3\int_{\Omega_{\min}}^{\Omega_{\max}}\Omega^2 N(E_i-\Omega)\left[1-\frac{\Delta^2}{E_i(E_i-\Omega)}\right]d\Omega. \tag{2.8}$$

Here T_c is the critical temperature of the film, Ω is the energy of the phonon being emitted, $N(E_i-\Omega)$ is the density of the final electron states and the integral is performed over all possible phonon states. The factor inside the brackets is a coherence factor that describes the nature of the electron-electron interaction in the superconducting state. The integral can be solved analytically [Kaplan, 76]. If we apply the following change of variable

$$y=\sqrt{\left(\frac{E_i-\Omega}{\Delta}\right)^2-1},$$

the integral can be solved as

$$\frac{1}{\tau_s}=\frac{1}{\tau_0}\left(\frac{1}{k_B T_c}\right)^3\times$$
$$\left[\frac{y^3}{3}+(3+\frac{E_i}{\Delta})y-\left(\frac{E_i}{\Delta}+\frac{\Delta}{2E_i}\right)y\sqrt{y^2+1}-\left(2\frac{E_i}{\Delta}+\frac{\Delta}{2E_i}\right)\ln\left(y+\sqrt{y^2+1}\right)\right]_{y(\Omega_{\min})}^{y(\Omega_{\max})}. \tag{2.9}$$

If the quasiparticle energy E is well above the Al gap energy, the scattering rate varies as $(E/\Delta)^3$ because of the total number of phonon states available. If the quasiparticle energy E is near the gap edge, the phase space for phonon emission and the coherence factor decrease and scattering slows down. The scattering occurs preferentially into states close to the gap where the electron density of states diverges. In the Al trap the inelastic scattering time of the quasiparticles with energy $=\Delta_{Ta}$ is fast (10 ns) compared to all other time scales that affect the detector response, such as the quasiparticle lifetime in Al and tunnel time. But the quasiparticle scattering time becomes very slow (~ µs) when the quasiparticle energy is near Δ_{Al}.

2.1.5 Quasiparticle Tunneling (Back-tunneling)

If two normal metals are separated by a thin insulator layer (NIN tunnel junction) and are voltage biased at low temperature, the tunneling current is given by

$$I_{nn} = A|T_{12}|^2 N_1(0)N_2(0)eV = G_{nn}V. \tag{2.10}$$

Here V is the bias voltage, G_{nn} is the conductance of the tunneling barrier, and T_{12} is the tunneling matrix. $N_1(0)$ and $N_2(0)$ are the densities of states at the Fermi surface of the two electrodes. At a low bias voltage the tunneling matrix and the densities of states can be approximated by their values at the Fermi surface. The Fermi function can be further approximated by a step function. Under these approximations the tunneling current varies linearly with the voltage. We define the tunnel time τ_{tun} by

$$I = \frac{eN}{\tau_{tun}}, \tag{2.11}$$

where $N = N(0)\cdot eV \cdot Vol$ is the total number of quasiparticles which can tunnel. Vol is the volume of the electrode. The tunnel time for the NIN tunnel junction is then

$$\tau_{tun,NIN} = e^2 N(0) R_{nn} Vol, \tag{2.12}$$

where $R_{nn} = 1/G_{nn}$ is the resistance of the tunneling barrier.

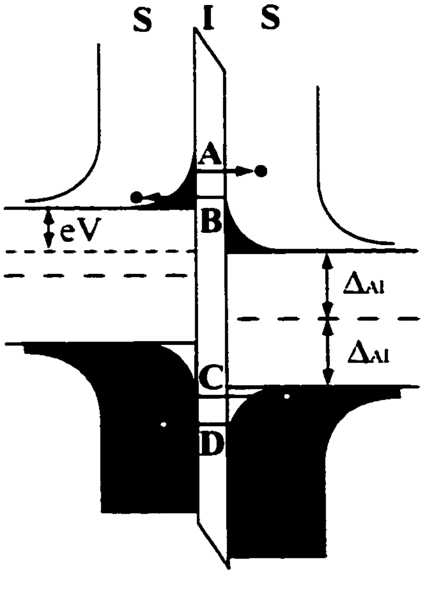

Fig. 2.3 The four tunneling processes for the SIS junction using semiconductor representation. A is direct tunneling, B is reverse tunneling. A and B are the electron-like quasiparticle tunnelings. C is the hole-like quasiparticle tunneling (reverse backtunneling) and D is the hole-like quasiparticle reverse tunneling (backtunneling).

If both metals are superconducting (SIS), the tunneling processes in the semiconductor representation are shown in Fig. 2.3. The tunneling current is given by

$$\begin{aligned} I_{SIS} &= \frac{G_{nn}}{e}\int_{-\infty}^{\infty}\frac{N_{1s}(E)}{N_1(0)}\frac{N_{2s}(E)}{N_2(0)}\left[f(E)-f(E+eV)\right]dE \\ &= \frac{G_{nn}}{e}\int_{-\infty}^{\infty}\frac{|E|}{\left[E^2-\Delta_1^2\right]^{1/2}}\frac{|E+eV|}{\left[(E+eV)^2-\Delta_2^2\right]^{1/2}}\left[f(E)-f(E+eV)\right]dE, \end{aligned} \quad (2.13)$$

where E is the quasiparticle energy relative to the Fermi surface, $N_{1s}(E)$ and $N_{2s}(E)$ are the density of states of the two superconducting electrodes. At finite temperature, there are thermally excited quasiparticles in the junction. If the junction is voltage biased, they will contribute to the tunneling current. This is the thermal subgap current, or subgap current. If the two electrodes have the same energy gap, the tunneling current can be estimated as [Van Duzer, 81]

$$I(V,T)=\frac{2(V+\Delta/e)}{R_{NN}}\sqrt{\frac{2\Delta}{eV+2\Delta}}\sinh\left(\frac{eV}{2k_BT}\right)K_0\left(\frac{eV}{2k_BT}\right)e^{-\Delta/k_BT}. \quad (2.14)$$

The number of quasiparticles with energy between E and $E+dE$ on the left side of the junction (Fig. 2.3) is $N_1(0)\frac{|E|}{\left[E^2-\Delta_1^2\right]^{1/2}}f(E)dE$. If we apply the same definition of the tunneling time Eq. (2.11) to the SIS junction, the quasiparticle tunneling time for the SIS junction can be written as [deKorte, 92]

$$\tau_{tun,SIS}=2e^2N_1(0)R_{nn}Vol\frac{\sqrt{(E+eV)^2-\Delta^2}}{|E+eV|}. \quad (2.15)$$

The factor of 2 arises from the fact that the quasiparticles have two branches, (one branch represents electron like quasiparticles ($k > k_F$), while the other represents hole like quasiparticles ($k < k_F$)), and if the bias voltage is high enough ($eV \gg kT$, for the case of quasiparticle in thermal equilibrium) only the electron-like branch of quasiparticles can tunnel. If we want to consider N in Eq. (2.15) to be the total number of quasiparticles with the energy between ***E*** and ***E+dE***, then the average tunnel time per quasiparticle is twice as long as we derived in Eq. (2.12).

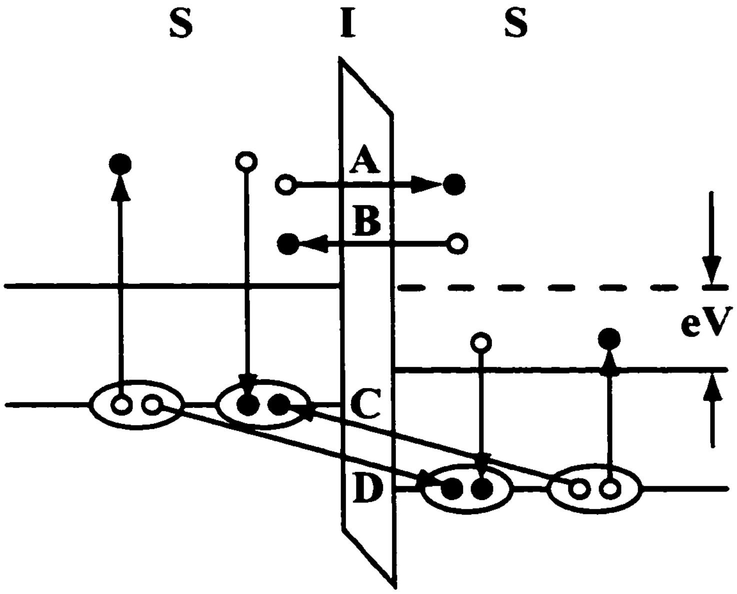

Fig. 2.4 The four tunneling processes of quasiparticles in an SIS junction using the excitation representation. A is direct tunneling, B is reverse tunneling, C is reverse backtunneling and D is backtunneling.

The x-ray photon induced current pulse is given by the net charge transferred across the tunnel barrier. There are four processes that contribute to the total current as shown in Fig. 2.4. All quasiparticles in the trap (left electrode) can directly tunnel into the counter-electrode (process A). All quasiparticles in the counter-electrode can backtunnel via the Gray effect by breaking a Cooper pair in the trap (process D). If the energy of quasiparticles is above eV_{bias}, quasiparticles can reversely tunnel from the counter-electrode into the trap (process B) or quasiparticles in the trap can reversely backtunnel into the counter-electrode by breaking a pair in the counter-electrode (process C). Both direct tunneling (A) and backtunneling (D) contribute to the charge flow in the forward direction, while reverse tunneling and reverse backtunneling cause a charge flow in the opposite direction. The net current is the current in the forward direction minus the current in the opposite direction.

The tunneling current depends on the number of quasiparticles in the trap N_{trap} and in the counter-electrode N_{ce}, as well as their energy distribution. For example, if the number of quasiparticles in the trap with energy relative to the energy gap Δ higher than eV increases, the reverse tunneling current increases and the net forward current decreases.

The tunneling time depends on the volume of the electrode from which the quasiparticles tunnel. The forward tunneling time and the reverse tunneling time are different since the volumes of the electrode and the counter-electrode are different in our detectors. It also depends on the density of states of the final quasiparticle energy, which increases towards the gap edge. Thus even for quasiparticles having the same energy in the trap, the tunnel time can be different for direct tunneling and reverse backtunneling. The same holds for backtunneling and reverse tunneling when the quasiparticles are in the counterelectrode.

In Fig. 2.3 the four tunneling processes are shown in the semiconductor representation, while in Fig. 2.4 they are shown in the excitation representation. The tunneling processes A and B look the same for both representations. Only processes C and D look different. In the semiconductor representation the processes C and D are called hole tunneling. We assume all hole-like quasiparticles have positive charges. The hole tunneling gives an opposite current to the electron tunneling.

For a junction at temperature T, if $k_B T \gg e\mathrm{V}_{\mathrm{bias}}$, both electrons and holes can tunnel from either side of the barrier and all four tunnel processes are possible. If $k_B T \ll e\mathrm{V}_{\mathrm{bias}}$, only electrons from the left side and holes from the right side can tunnel (process A and D). In order to get a maximum current out of the tunneling and reduce the reverse cancellation current, we have to bias the junction at high voltage.

2.1.6 Quasiparticle Outdiffusion

After quasiparticles tunnel through the junction into the counter-electrode, they can diffuse out into the wiring pad and no longer stay in the junction region. This process is called quasiparticle outdiffusion. After the quasiparticles diffuse out from the junction region, they can no longer be involved in the backtunneling process. So the outdiffusion process reduces the possibility of backtunneling.

2.2 Josephson Effects

Our detectors use Al-AlOx-Al SIS tunnel junctions as quasiparticle detectors. The tunnel junctions show various Josephson effects. The Josephson effects were extensively discussed in other literature such as Ref. [Barone, 82]. We give a brief review of them and discuss their influence on our measurements.

2.2.1 Critical Current

At zero bias voltage, the supercurrent flowing between the two superconducting electrodes separated by a thin insulating barrier is

$$I_s = I_c \sin\Delta\varphi, \tag{2.16}$$

where $\Delta\varphi$ is the difference of the gauge-invariant phase of the Ginzburg-Landau wave function between the two electrodes, and the critical current $I_c = I_c(H=0)$ is the maximum supercurrent that the junction can support.

The maximum supercurrent of an extended junction can be modulated by a magnetic flux Φ that penetrates the junction in the plane of the junction. For ease of discussion, we use a coordinate system such that the electrode surfaces are parallel to the xy plane, the ambient magnetic field H lies along the y direction, and the tunnel current is along the z direction. The local magnetic field in the barrier is equal to the ambient magnetic field H provided that screening by the Josephson current can be neglected. If the two electrodes are thick compared to the London penetration depth λ and separated by an insulating barrier of thickness d, the phase difference between the two electrodes as a function of location is $\Delta\varphi = \gamma_0 + kx$, where $k = 2\pi\Phi/\Phi_0 = 2\pi H(2\lambda + d)/\Phi_0$, and Φ_0 is a flux quantum. The supercurrent is then given by

$$I_s \equiv I_c(H) = \iint J_c(x,y)\sin(\gamma_0 + kx)dxdy \tag{2.17}$$

where $J_c(x, y)$ is the Josephson critical current density. The peak current can be seen as the Fourier transform of the junction shape function $\int J_c(x,y)dy$.

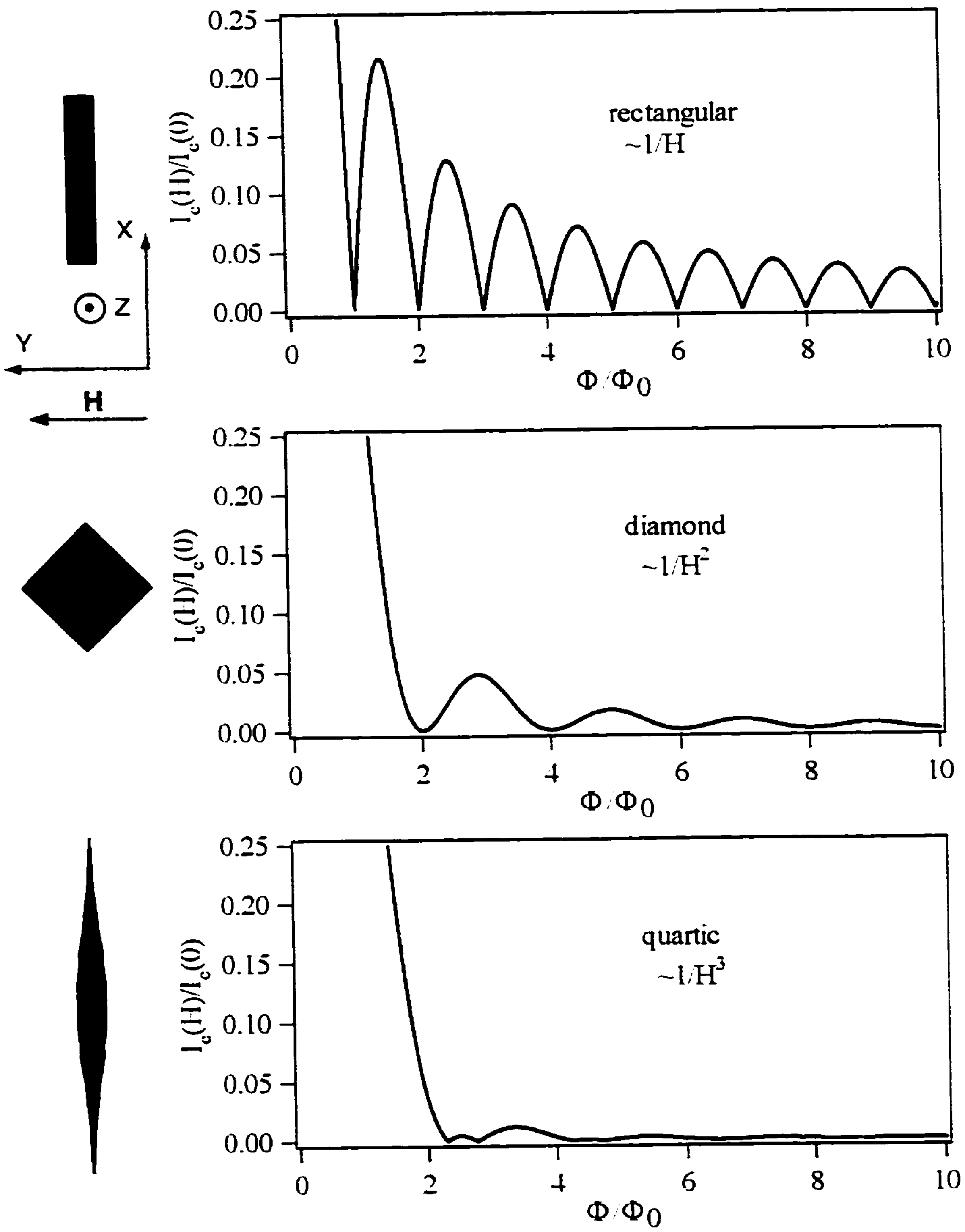

Fig. 2.5 The theoretical supercurrent $I_c(H)$ as a function of magnetic flux for rectangular, diamond, and quartic shaped junctions.

Fig. 2.5 shows theoretical $I_c(H)$ curves for three different shaped junctions. The quartic shaped junction is described by a shape function $f(x) = 9(1-4y^2+4|y|^3-y^4)$. The critical current of the quartic shaped junction as a function of the magnetic field H falls faster ($\sim 1/H^3$) than the critical current of the rectangular ($\sim 1/H$) and diamond ($\sim 1/H^2$) shaped junctions.

For quasiparticle measurements the supercurrent has to be suppressed in order to stably bias the junction in the subgap region. We want to use minimum magnetic field to suppress the supercurrent in order to avoid trapped flux. To achieve the best detector performance the shape of the junction has to be carefully designed.

2.2.2 Fiske Resonance Modes

Fiske resonance modes arise when the Josephson frequency matches one of the frequencies of the various electromagnetic cavity modes in the junction barrier. For voltage biased junctions they are observed as resonance peaks in the I-V curve, occurring at a voltage that is related to the resonance frequency [Fiske, 64; Eck, 65].

The *ac* Josephson effect describes the time evolution of the phase difference $\Delta\varphi$. When a voltage difference V is maintained across the junction, $\Delta\varphi$ will change at a rate

$$d(\Delta\varphi)/dt = 2eV/h, \tag{2.18}$$

and the current oscillates with a frequency $\nu = 2eV/h$.

If the effect of the Josephson current on the time-dependent electromagnetic fields in the barrier is taken into account, the phase difference $\Delta\varphi$ will vary in both time and space. Using the *sine-Gordon* equation one can solve for $\Delta\varphi$. The fields and currents in the junction can be further calculated from $\Delta\varphi$. Combining Maxwell's equations with the Josephson equations and eliminating the Josephson current and voltage, we arrive at the following *sine-Gordon* equation [Barone, 82]

$$\left(\frac{\partial^2}{\partial x^2}+\frac{\partial^2}{\partial y^2}-\frac{1}{\bar{c}^2}\frac{\partial^2}{\partial t^2}\right)\Delta\varphi = \frac{\sin\Delta\varphi}{\lambda_J^2}, \tag{2.19}$$

where λ_J is the Josephson penetration depth and is calculated from

$$\lambda_J = \left[\frac{c\Phi_0}{8\pi^2 J_c (2\lambda + d)} \right]^{1/2}, \tag{2.20}$$

where λ is the London penetration depth and $\bar{c}$ is the electromagnetic wave velocity for a barrier with a relative dielectric constant ε_r

$$\bar{c}^2 = \frac{c^2}{\varepsilon_r \left(1 + 2\lambda / d\right)}. \tag{2.21}$$

If λ_J is very large, the solutions to Eq. (2.19) are simply plane waves with velocity $\bar{c}$. These electromagnetic waves will couple strongly to the Josephson current if the frequency of the Josephson current matches the frequencies of the various electromagnetic cavity modes. Once the frequency match occurs, there will be current steps in the I-V curves (current bias) as observed by Fiske [Fiske 64]. These are the so-called Fiske steps or Fiske resonance modes. For junctions with a simple shape, the voltage steps (or peaks) of the Fiske modes can be calculated analytically. The two-dimensional Fiske modes in rectangular junctions occur at voltages

$$V_{nm} = \frac{h\bar{c}}{4e} \left(\frac{n^2}{L^2} + \frac{m^2}{W^2} \right)^{1/2}, \tag{2.22}$$

where W and L denote the width and length of the rectangular junction respectively and integers m and n denote the order of the Fiske modes. Fiske modes in junctions with a special shape such as quartic or diamond are hard to calculate analytically. A numerical approach is typically required. From Eq. (2.22) we see that the Fiske resonance voltages are inversely proportional to the junction's dimension. Since the Fiske modes cause excess current and unstable bias, their existence in the subgap region will limit the voltage bias range. Proper designs of the junction geometry can eliminate the Fiske modes in the subgap region.

Both *dc* and *ac* Josephson effects play negative roles in the detector performance as will be shown in Chapter 4. The *dc* Josephson current affects the stable *dc* bias of the junction and the Fiske modes limit the effective voltage bias range. Although both effects can be eliminated separately in the design, reducing one effect will typically cause an increased effect of the other for a given device geometry. In reality we have to optimize the junction geometry to minimize their total effect on the measurement.

2.2.3 Annular Junction

An annular junction is a doughnut shaped junction. This type of junctions are of particular interest because they offer the possibility to suppress the Josephson current with one or more flux quanta trapped in the junction without applying an external magnetic field.

For our research purposes, we focus our attention on small annular junctions. The circumference of the outer ring is typically chosen to be shorter than the Josephson penetration depth λ_J. This ensures that there will be no traveling soliton generated in the ring and the magnetic field of the trapped fluxons will be uniformly distributed. The inner radius r of the junction is chosen to be much smaller than the outer radius R in order to maximize the absorption area.

When a uniform magnetic field is applied parallel to the junction plane, I_s as a function of H can be calculated from Eq. (2.17) for the annular shape to be

$$\frac{I_s}{I_0} = 2\left|\frac{kRJ_1(kR) - krJ_1(kr)}{k^2R^2 - k^2r^2}\right|, \tag{2.23}$$

where $k = 2\pi H(2\lambda + d)/\Phi_0$ and λ is the London penetration depth.

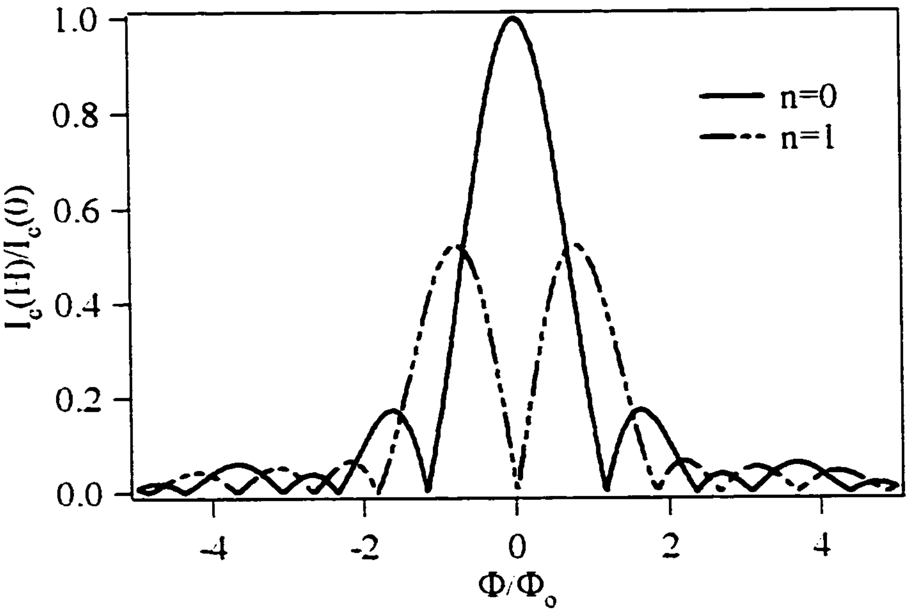

Fig. 2.6 $I_c(H)/I_c(0)$ vs. Φ/Φ_0 for an annular junction (r/R = 1/5) with zero (solid line) and one (dashed line) trapped fluxon in the central hole.

If there are n trapped vortices. $n = 0, 1, 2, \ldots$ in the annular junction. I_s as a function of H now becomes [Nappi. 97]

$$\frac{I_s}{I_0} = \left| \frac{2}{\left(1 - r^2 / R^2\right)} \int_{/R} x J_n \left(x \pi H / H_0 \right) dx \right| . \tag{2.24}$$

where $J_n(x)$ is the nth Bessel function. and H_0 is the characteristic field $H_0 = \Phi_0 / 2R (2\lambda + d)$. The $I_s(H)$ curve for $r/R = 0.2$ is shown in Fig. 2.6. We can see that when there is one fluxon trapped in the junction. the Josephson current is completely suppressed without any external magnetic field.

Due to the interaction between the Josephson current and the electromagnetic field. there exist Fiske resonance modes in the annular junctions. The amplitudes and positions of the Fiske modes can be calculated using a perturbation technique [Nappi. 98]. The positions are obtained by first solving the following equations for c_{km} and χ_{km}.

$$\begin{aligned} J_k'\left(\chi_{km} R\right) + c_{km} N_k'\left(\chi_{km} R\right) = 0 \\ J_k'\left(\chi_{km} r\right) + c_{km} N_k'\left(\chi_{km} r\right) = 0 \end{aligned} \tag{2.25}$$

where J_k and N_k are the kth-order Bessel function and Neumann function respectively. the primes indicated the derivative with respect to the argument. The Fiske modes are present at the resonance voltages $V_{nm} = \chi_{nm} \dfrac{\Phi_0}{2\pi} \left(\dfrac{2\lambda + d}{d} \right)^{1/2}$. In the absence of external magnetic field and with n trapped flux quanta. only the nth azimuthal mode is selected and all other modes ($k \neq n$) are suppressed. The amplitudes of the Fiske modes in general decrease rapidly with the order of the Fiske modes in the absence of external magnetic field.

If the Josephson current can be suppressed low enough by trapping n fluxons in the hole of the junction and the resonance voltage of the Fiske mode is above Δ / e. the junction can be stably biased without any external magnetic field. This is very promising for astronomy applications. but there is still much to do to further study and improve this novel technology. In Chapter 4.1.2 we will present some preliminary results of the Nb based Al annular junction as well as some associated problems.

2.3 STJ Detector Device Noise Sources

In order to improve the performance of our STJ detectors, especially their energy resolution, we have to understand well the noise sources. The device noise sources set the lower limit of the energy resolution of the detector even with perfect electronic measurement circuits. Several known device noise sources are discussed here.

2.3.1 Quasiparticle Creation Noise

Microscopically the quasiparticle creation process is a Poisson-like statistical process. The fluctuation in the number of the created quasiparticles ΔN_{create} is proportional to $\sqrt{N_{create}}$. This imposes a fundamental limitation on the ultimate energy resolution of our detectors. The Full-Width-at-Half-Maximum (FWHM) of a spectral line due to the creation noise is given by

$$\Delta E_{create} = 2.355\sqrt{F\varepsilon E_x}, \tag{2.26}$$

where F is the Fano factor [Fano, 47], E_x is the incident photon energy, and $\varepsilon \approx 1.74\,\Delta$ is the effective (or average) energy required to create a quasiparticle. The Fano factor measures the correlation degree of the Poisson-like quasiparticle creation process. A Fano factor less than one means that there is correlation in the creation process so that the energy resolution is better than that for a pure Poisson-like process. For most superconductors, including Ta, the Fano factor is around 0.22 [Kurakado, 82]. Since the superconducting energy gap Δ is of the order of meV, which is about 1000 times smaller than that of a semiconductor, the intrinsic energy resolution of the superconductor detectors is about 30 times better than that of the conventional semiconductor detectors. The energy resolution due to the quasiparticle creation process in the Ta absorber (Δ_{Ta} =700 μV) is $\Delta E_{create} = 3$ eV for the 6 keV photons.

2.3.2 Absorber Loss

The quasiparticles created by an x-ray photon can be lost in the Ta absorber by recombining with other quasiparticles before they reach the Al trap. If each quasiparticle has the same loss probability in the absorber per unit time, then the number of lost quasiparticles obeys the binomial distribution. We define $\beta = N_{loss}/N_0$, where N_0 is the initial number of quasiparticles and N_{loss} is the average number of lost quasiparticles. The energy resolution caused by the quasiparticle loss in the Ta absorber is given by [Segall, 00]

$$\Delta E_{\beta} = 2.355\sqrt{\varepsilon E\left(\frac{\beta}{1-\beta}\right)}. \tag{2.27}$$

The parameter β depends on the dimensions of the absorber (see Chapter 5).

2.3.3 Trapping Multiplication

After the quasiparticles diffuse from the Ta absorber (Δ_{Ta}= 700 μV) into the Al trap (Δ_{Al}= 180 μV), they scatter down inelastically from the Ta energy gap to lower energy levels in the Al trap by emitting phonons. Some of the phonons are energetic enough to break Cooper pairs in the Al trap and generate new pairs of quasiparticles. This way of creating quasiparticles in the Al trap is called trapping multiplication. We assume that each quasiparticle in the absorber has the same probability to create a pair of quasiparticles in the Al trap and the process follows the binomial distribution. If the average number of quasiparticles to break Cooper pairs in the Al trap is N_{multi}. The initial quasiparticle number is N_0. The energy resolution due to the trapping multiplication is then [Segall, 00]

$$\Delta E_{multi} = 2.355\sqrt{\varepsilon E\left(\frac{(\kappa-1)(3-\kappa)}{\kappa^2}\right)}, \tag{2.28}$$

where $\kappa = 1 + 2N_{multi}/N_0$.

2.3.4 Backtunneling

In the Al junction, quasiparticles may tunnel and backtunnel several times before they are lost by recombining into Cooper pairs or leaving the junction. We assume that each quasiparticle has a probability P_1 to tunnel from the trap and P_2 to tunnel back to the trap. If we define $\bar{n}$ to be the average number of times that a quasiparticle tunnels, the mean and the statistical noise of $\bar{n}$ are calculated as [Goldie, 1994]

$$\bar{n} = \frac{P_1(1+P_2)}{(1-P_1P_2)}, \tag{2.29}$$

and

$$\Delta E_{back} = 2.355\sqrt{G\varepsilon E} = 2.355\sqrt{\varepsilon E\left(\frac{P_1 - P_1^2 + 3P_1P_2 + P_1^2P_2}{P_1^2(1+P_2)^2}\right)}, \tag{2.30}$$

where G is defined as the effective backtunneling factor.

2.3.5 Cancellation

If the quasiparticles have an energy higher than eV_{bias}, they can reversely tunnel from the counter-electrode or reversely backtunnel from the trap. The two tunneling processes will partially cancel each other. At the same time their current noises add up to the measurement. We assume that each quasiparticle has the same probability to reversely tunnel and follows the binomial distribution. We define N_{rev} as the number of tunneling events that transfer charge in the reverse direction. The total number of tunneling events is $\bar{n}N_0$. The total charge after cancellation is then $(1-2\gamma)e\bar{n}N_0$, where $\gamma = N_{rev}/(\bar{n}N_0)$. The statistical noise caused by the cancellation of the reverse tunneling is then given by [Segall, 00]

$$\Delta E_{\gamma} = 2.355\sqrt{\varepsilon E\frac{4\gamma(1-\gamma)}{(1-2\gamma)^2}}. \tag{2.31}$$

After combining all five device noise sources listed above, the total energy resolution due to the quasiparticle statistical processes in the device is

$$\Delta E_{FWHM} = 2.355\left(F + \frac{\beta}{1-\beta} + \frac{(\kappa-1)(3-\kappa)}{\kappa^2} + G + \frac{4\gamma(1-\gamma)}{(1-2\gamma)^2}\right)^{1/2}(\varepsilon E)^{1/2}. \tag{2.32}$$

Chapter 3 Device Fabrication and Experimental Setup

Making the best possible device and setting up the right measurement circuits are essential to the success of our project: a good device starts from a good design which includes the choice of the right material and the right junction geometry. A elaborate fabrication process has to be followed to produce the desired device. The performance of our system is determined not only by the device, but also by the performance of the measurement circuits. We will discuss the *dc* and *ac* electronic setups and their noise performance. We also present several technical improvements in our measurement. In the end we will briefly mention the data acquisition and processing technique.

3.1 Device Materials and Fabrication

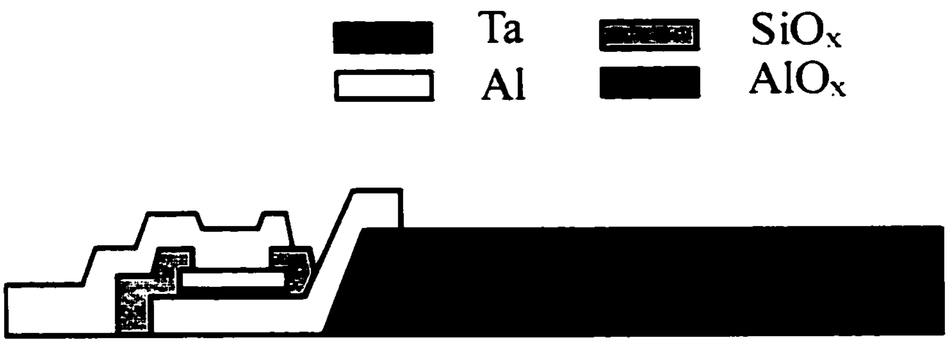

Fig. 3.1 The cross section of the device with a junction on the left side. Ta film is used as the x-ray photon absorber. Al-AlOx-Al forms the superconducting tunnel junction as the quasiparticle detector.

To design high performance single photon x-ray detectors, there are several factors that need to be considered: (1) the x-ray absorption efficiency, (2) the energy resolution, (3) the time response to a single photon, (4) the durability of the device, (5) the spatial resolution and the number of the pixels if the imaging capability is considered. In this section, we mainly discuss the choice of materials, device parameters, and fabrication procedure. The cross section of the device with one junction is shown in Fig. 3.1. The entire device is fabricated on a Si substrate with SiO_2 on the top of the Si substrate. An Al junction is laterally connected to the Ta absorber. An insulating layer of SiO separates the Al trap from the Al wiring pad. The devices presented here other than device A were fabricated by L. Frunzio and C. Wilson. The details of the fabrication procedures and conditions can be found in Ref. [Gaidis, 94].

The detectors we measured are capable of performing 1-D imaging with two tunnel junctions. Later on in Chapter 6 we will propose designs of 2-D imaging detectors with four tunnel junctions.

3.1.1 Absorber – Ta

The high atomic number material Ta (Z=73) is chosen as the x-ray absorber for our detectors because it has shorter absorption length and higher absorption efficiency compared to other materials such as Al and Nb. Ta, as a refractory material, also demonstrates very good durability as an absorber material. Other alternative superconducting materials with short absorption lengths, such as lead and tin, degrade rapidly with thermal cycling [Kraus, 98]. One of our devices (device A), which was fabricated eight years ago, still shows very good performance.

The lifetime of quasiparticles created in the Ta absorber is about 80 μs [Li, 02b], which is much longer than that in the Nb (~ 2 μs) [Le Grand, 97]. One reason is that the Ta oxides cannot form quasiparticle trapping centers while Nb oxides can [Halbritter, 87]. For a 200×100 μm^2 Ta absorber, the quasiparticle loss is negligible. For the Nb based detectors, a stack structure with a thin Al trapping layer [Booth, 87] has to be used because of the short quasiparticle lifetime. In addition, Ta has better spatial uniformity than Nb does [Li, 02a; den Hartog, 02], which is also very important in achieving high energy resolution and good imaging.

Fabrication: 6000Å thick Ta films are deposited on the Si substrate by *dc* magnetron sputtering at a rate of 40Å/s. The Si substrate is kept at a temperature of 700°C during the deposition process. This produces bcc Ta films with a transition temperature T_c above 4.2K. The absorber pattern is defined by wet etch in a 3:1 solution of $FeCl_3/HCl$ and HF. The wet etch makes sloped edges for good contact with the 1500Å thick Al trap. The thickness of the absorber and the response time of the detectors are limited by the diffusion constant and the quasiparticle lifetime in the Ta film. The measured values of these two parameters are discussed in Chapter 5 and are found to be much smaller than theoretical predictions.

Even though Ta has a short x-ray absorption length, the absorption efficiency of the 6000Å thick Ta film is about 25% for the 6 keV x-ray photons. By increasing the thickness of the Ta absorber, we expect to increase the absorption efficiency. The absorption efficiency will be even higher if the detector is used to measure lower energy x-ray photons.

3.1.2 Tunnel Junction – Al

Al–AlO$_x$–Al is chosen as a tunnel junction due to several advantages it has. (1) Al oxides are very robust and can form high quality junctions. (2) The energy gap of Al (Δ_{Al}=180μV) is lower than that of Ta (Δ_{Ta}=700μV), so it can form an effective quasiparticle trap for the Ta absorber. Due to the large gap difference between the two materials we can use gap engineering to implement the trap structure to independently optimize the dimension and geometry of the absorber and the junction. (3) Al has a much smaller atomic number than Ta has so that it reduces the number of unwanted photon events absorbed in the Al junction.

Fabrication: The Al trap is thermally evaporated at a rate of 200 Å/s for a thickness of about 1500Å after the Ta absorber is cleaned by ion beam to ensure good interface. Then it is thermally oxidized at room temperature for 3 hours in 600 mTorr of oxygen. The counter-electrode is then thermally evaporated at a much lower rate of 15Å/s to prevent the impinging atoms from damaging the barrier. This process can produce tunnel junctions with a normal state resistance of R_{NN}=0.5Ω and a current density of 30A/cm^2. The junctions are defined by wet etching. Then a 1500Å thick SiO film is thermally evaporated to passivate the junction edges and to insulate the wiring from the Al trap. After an ion beam cleaning, the Al wiring is deposited on the counter-electrode. The thickness of the wiring is about 4000Å to ensure a rapid outdiffusion and to reduce backtunneling.

We found out that the dominant noise sources of the previous detector were due to incomplete cooling of quasiparticles in the junction [Segall, 99]. The quasiparticle tunneling time is related to the volume of the Al trap and the transparency of the barrier. By changing the trap volume, the barrier transparency, and the junction geometry we can improve the quasiparticle cooling and therefore the energy resolution. The design of the junction geometry and its effect on the energy resolution will be discussed in more detail in Chapter 4. It is also expected that the use of wide wiring pads would effectively reduce the backtunneling and backtunneling noise. But in practice, there is no noticeable large improvement.

3.1.3 Ground Contact – Nb or Ta

A ground contact is constructed to make electrical contact to the absorber in order to voltage bias the two junctions separately. To prevent quasiparticles from diffusing out into the ground contact itself a large energy gap material has to be used as the electrical ground contact. One possible configuration is to use a thin strip of Nb (Δ_{Nb}=1.5mV) of about 1500Å thick in the middle of the Ta absorber as the ground contact. The Nb contact is sputtered at room temperature and is patterned by reversal photoresist liftoff. However the detectors using this design show worse performance for the events in the center of the absorber around the ground contact than at the edges of the absorber. One possible reason is the formation of trapping sites by the Nb metallic oxides at the Ta-Nb interface. To solve the problem another configuration can be used. We use a Ta ground contact to connect to the Al trap of one of the two junctions. The Ta contact is fabricated at the same time as the Ta absorber. Its size is made small to reduce the absorption area. Such device gives spatially uniform performance within a large range of the absorber. The experimental results will be presented in Chapter 5.

3.1.4 Substrate – SiO_2 on Si

Si is chosen as the substrate for our detectors. The Si substrate is oxidized to form a SiO_2 layer before the device fabrication. The whole detector is then fabricated on top of the SiO_2 layer.

When an x-ray photon is absorbed in the Si substrate, it generates lots of phonons. If these phonons are able to break Cooper pairs and excite quasiparticles in the Ta absorber and/or the Al trap, they will generate current signals during the x-ray detection, which are called substrate events. If these substrate events overlap with real signals, they can deteriorate the energy resolution of the detectors. The SiO_2 layer acts as a buffer layer. It attenuates the coupling of the substrate events to the device. It also reduces the phonon loss from the Ta absorber into the substrate to prolong the quasiparticles' lifetime. Chapter 8 shows some evidence of the substrate events and how they affect the detector performance and possible solutions.

3.2 Cryogenic Setup

The use of the Al superconducting tunnel junction requires an operating temperature below 0.3 K for good noise performance and small thermal quasiparticle loss. The lower temperature also reduces the thermal subgap current and increases the dynamic resistance of the junction. Thus the shot noise of the thermal subgap current and the effective current noise caused by the voltage noise is reduced (see Chapter 4).

The detectors are enclosed in a 2-stage ^3He cryostat. Fig. 3.2 shows the cryogenic setup. This cryostat is able to attain a base temperature of about 0.21K lasting for about 11 hours. Liquid N_2 and liquid ^4He are used to first cool down the two stages of the cryostat to about 1.5K. After the condensation of the ^3He at the two cold stages, two charcoal absorption pumps begin to lower the vapor pressure above the liquid ^3He in order to bring the temperature down. The first stage is cooled to about 0.3K. The second stage is further cooled to 0.21K through a pumping line cooled at the first stage. We use the calibrated subgap current of the Al tunnel junction and a Germanium Resistance Thermometer (GRT) to determine the temperature of the device. After the temperature is measured the thermometer is turned off during the rest of the measurement to prevent current from flowing near the junctions that could cause trapped flux in the junctions. Apiezon N thermal grease is used to ensure good thermal contact of the device to the second cold stage. A more detailed description of the cryostat structure can be found in Ref. [Friedrich, 97b].

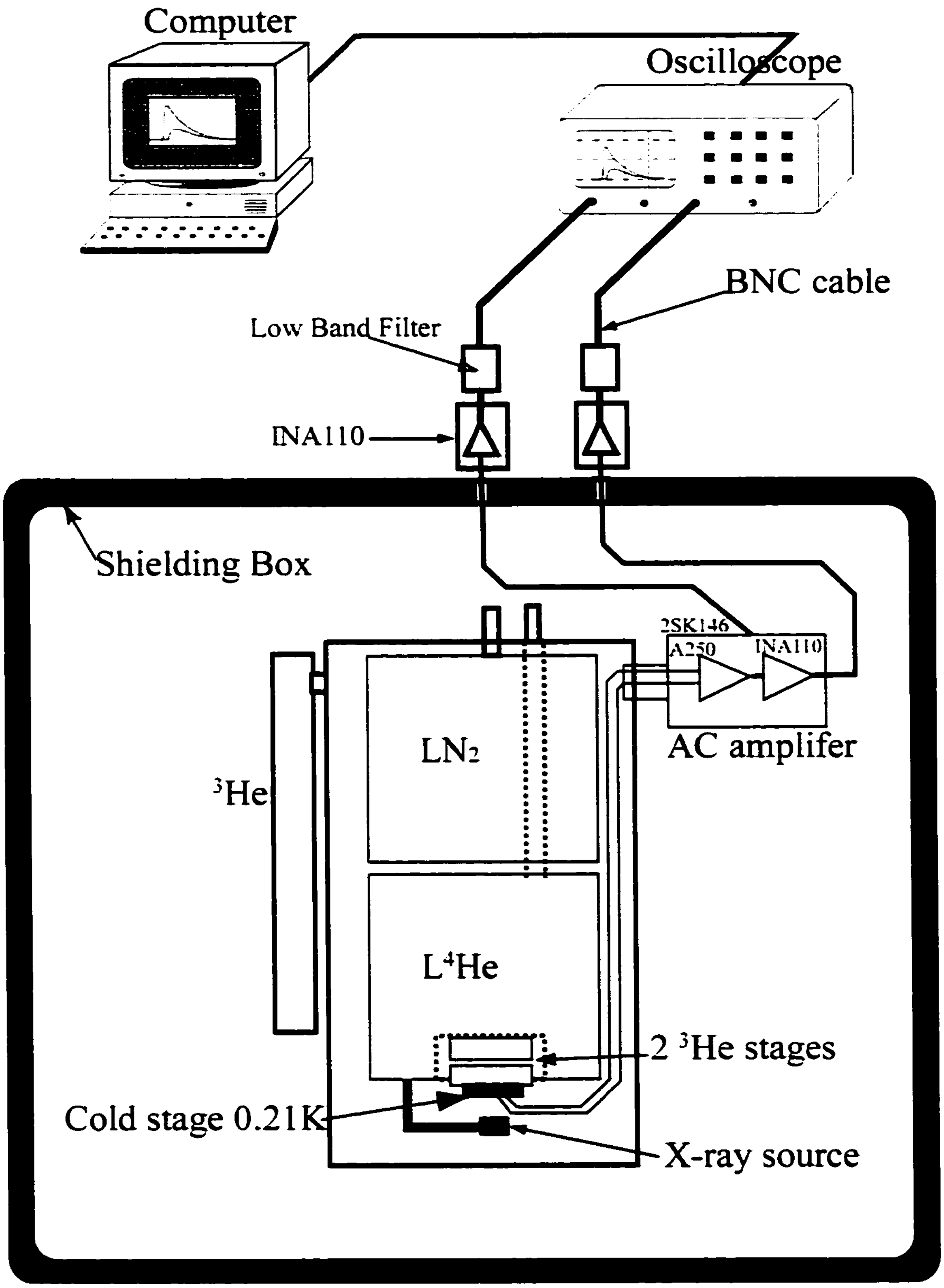

Fig. 3.2 The cryogenic setup and data acquisition instruments.

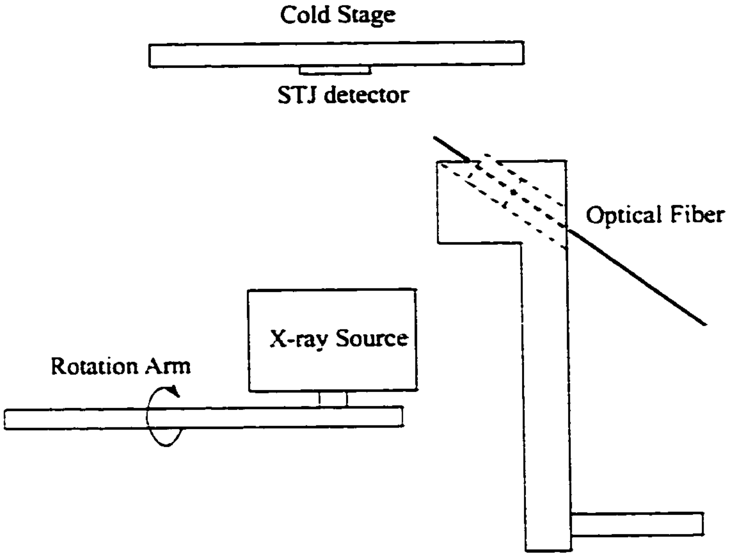

Fig. 3.3 Laser detrapping setup. The laser is sent through an optical fiber that is aligned to the STJ detector. The x-ray source is mounted on a rotation arm under the detector.

There are two major improvements in this setup compared to the previous one. The first one is that we successfully cooled the feed back resistors to 1.5K at the pumped liquid ^{4}He stage. This improvement allows us to dramatically reduce the Johnson noise of the feedback resistors that were operated at room temperature in the old setup. Less noise leads to better energy resolution.

The second improvement is the laser detrapping technique that was discovered in the optical photon measurement. Trapping flux in the junction can seriously degrade the device performance. Once the junction traps flux the electronic noise becomes dramatically worse, and it is usually too bad to continue the test. Without a proper detrapping technique the experiment would normally be terminated because of the trapped flux. The laser detrapping technique enables us to continue the experiment. In the setup shown in Fig. 3.3, an Al coated optical fiber is aligned to the detector. The optical fiber is fed through the vacuum tight tube and taped down to the cold stages. Whenever the junctions trap flux, the light from a laser pointer is sent through the optical fiber down to the device. The "strong" laser light drives the junctions from the superconducting state to the normal state immediately. After the laser is turned off, the junctions cool back to the superconducting state and the trapped flux is driven out of the junction by the

Meissner effect. It takes about 30 minutes to cool the junction back down to 0.21K after the laser detrapping which is much better than the several hours used to warm the whole cold stage above Al T_c and then cool it back down to 0.21 K in the old setup. Thus with the laser detrapping technique much less liquid ^{4}He is consumed. Another advantage over the detrapping by electric heating is the "cleanness" of the light. That means there is no electric current flowing near the junctions to create magnetic field that could cause trapped flux when the junctions are cooled down again. By using this laser detrapping technique the measurement efficiency is improved by a factor of about 6.

The x-ray source we use is a 50 μCi radioactive ^{55}Fe x-ray source, which is mounted on a rotating arm on the cold stage. The x-ray source is kept 2 cm away from the device. It can be turned towards or away from the device to verify if the current signals are generated by the x-rays from the ^{55}Fe source. The count rate of x-ray photons hitting the detectors can be controlled by changing the facing angle of the source to the device. The ^{55}Fe x-ray source decays into manganese by emitting two Mn lines: 88% Mn K_α line with an energy of 5890 eV, and 12% Mn K_β line with 6490 eV. The Mn K_α line is composed of two lines that are $K_{\alpha 1}$ (5898.73 eV) and $K_{\alpha 2}$ (5887.65 eV). The relative strength ratio of these two K_α lines is $K_{\alpha 1} : K_{\alpha 2} = 100 : 51$.

The magnetic field is produced by one pair of superconducting coils made of NbTi superconducting wire. The device is located in the center of the two coils so that the magnetic field is parallel to the junction. The magnetic field is controlled by the current flowing through the NbTi superconducting wires.

3.3 DC and AC Electronics

Proper setup of the *dc* and *ac* electronics is crucial to the success of this work. One important requirement is to be able to stably *dc* bias the junction in the subgap region (<180μV). Due to the highly non-linear I-V characteristics and various Josephson effects present in the tunnel junctions, it is very difficult to achieve stable biasing when doing *ac* measurements. Chapter 2 briefly introduced how to adjust the shape of the junction to suppress the Josephson current by a small magnetic field and eliminate the Fiske modes from the subgap region. In practice, we apply a magnetic field of about 20 Gauss parallel to the junction to suppress the *dc* Josephson effect.

Our 1-D imaging detector requires that the two junctions be biased simultaneously for proper photon detection. One way is to current bias both junctions with the Josephson current suppressed below the subgap current (~ 20 nA). However it is extremely difficult to find one magnetic field to perfectly suppress the Josephson current of both junctions at the same time. Another choice is to use a *dc* voltage bias which can keep the bias stable even though there is a large residual Josephson current. Due to the large dynamic resistance in the subgap bias region, the active voltage bias is used to reduce the *ac* current flowing through the *dc* path. In doing the experiment, a combination of current bias and voltage bias is used.

However it is difficult to start the active voltage bias from zero voltage when there is residual current in the junctions. There are at least two factors causing this problem. If the source impedance is low the active voltage bias is unstable and saturated. The easy solution to this is to add a cold resistor of 100Ω in series with the junction. If the load line of the voltage bias is not stiff enough to avoid crossing the *dc* Josephson current, the switching between the Josephson current and the subgap current can cause the electronics to be unstable and trap flux inside the junction. To bootstrap the voltage bias, we resort to the current bias first since the electronics is perfectly stable for current bias. First we use current bias to find the best possible magnetic field to almost completely suppress the Josephson current of both junctions. Then we adjust the field to current bias one junction to achieve perfect suppression of its Josephson current. We then active voltage bias the first junction at high voltage (>80 μV). Since the high voltage bias is stable, we can further adjust the magnetic field and current bias the second junction without affecting the first one that has been voltage biased. Once the Josephson current in the second junction is perfectly suppressed we switch to active voltage bias for the second junction.

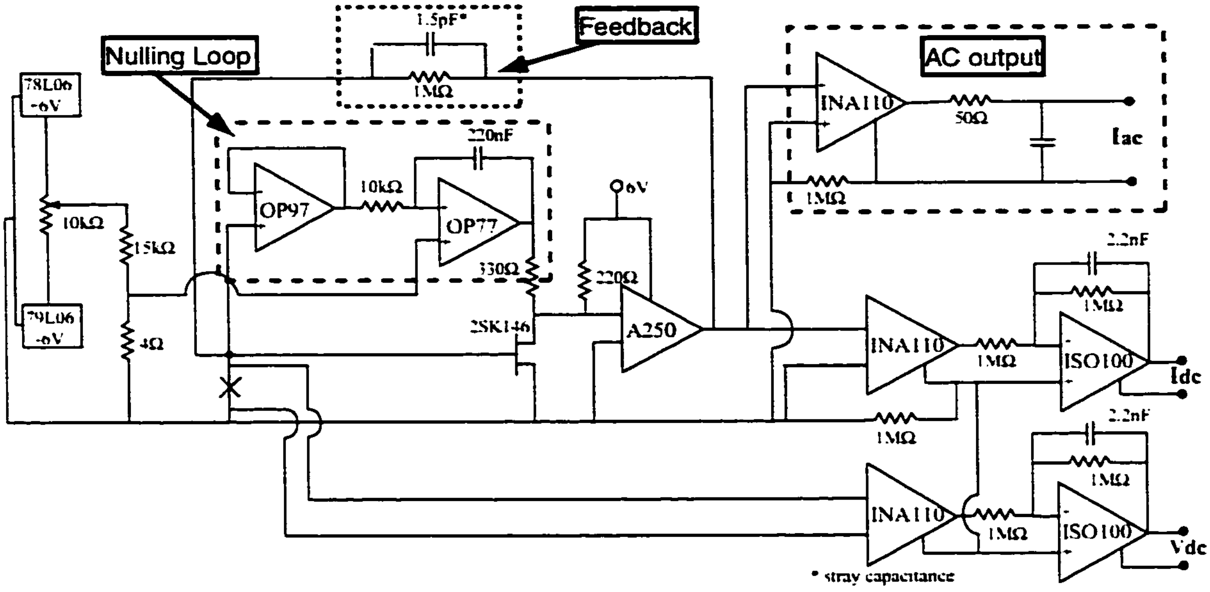

Fig. 3.4 Active voltage bias circuit with an AC current amplifier.

The whole electronic setup is shown in Fig. 3.4. The active voltage bias is implemented through a feedback loop called the nulling loop, which consists of a follower OP97 and an integrator OP77. The nulling loop keeps the bias voltage of the junction stable through the *dc* feedback. The nulling loop must have low input offset voltage and low current noise in order to keep the bias voltage fluctuation low. The OP97 has a voltage offset of 25μV and a current noise of $20 fA/\sqrt{Hz}$. The voltage noise of the junction at frequencies above 70Hz is filtered out by the follower and the integrator.

The current signal is measured by the *ac* current amplifier [Friedrich, 97]. Compared to charge amplifiers, the current amplifier is capable of noise filtering and allows the study of the quasiparticle dynamics. Chapter 5 discusses some physical properties of the quasiparticles that are derived from the shape of the current pulses. Depending on the photon absorption position, the maximum amplitude of the current pulses from a device with a 200 x 100μm^2 Ta absorber is about 200nA, while the thermal subgap current is only about 20 nA for a 2000 μm^2 Al junction at 0.21K. The bandwidth of the current signal is less than 100 kHz.

The junction is *dc* coupled to the *ac* current amplifier, one end of the junction is connected to the circuit ground, the other end is connected to the gate of a JFET, and its voltage is adjusted by the nulling loop following the voltage reference which is connected to the OP77. The current amplifier consists of a separate JFET followed by a transimpedance amplifier. The JFET we chose is the Toshiba 2SK146 JFET which is one of the JFETs with the lowest input voltage noise of $0.4\ \mathrm{nV}/\sqrt{\mathrm{Hz}}$ and negligible current noise of about $18\ \mathrm{fA}/\sqrt{\mathrm{Hz}}$ [Gaidis, 94]. The transimpedance amplifier is the Ampek A250, which is a preamplifier with a low noise and a large bandwidth. The combination of the two can form a very good composite amplifier. Depending on the feedback resistance value, the amplifier becomes either a current amplifier or a charge amplifier. The open loop gain of the amplifier is about 2×10^4. The feedback resistance $R_f = 1\mathrm{M}\Omega$ and stray capacitance C_f of about 1.5pF set the bandwidth of the amplifier to about $1/2\pi R_f\ C_f = 100$ kHz, which is acceptable for the signals we measure. At room temperature the $1\mathrm{M}\Omega$ feedback resistor contributes $\sqrt{4k_B T / R_f} = 0.13 pA/\sqrt{Hz}$ Johnson noise to the energy resolution. This noise can be reduced by cooling down the feedback resistor to a lower temperature. The input of the A250 must be sustained at about 3 V. This constrains the source-drain voltage and the bias current of the FET. The nulling loop senses the gate voltage of the FET, compensates the source-drain current of the FET and keeps the voltage at the input of the A250 at about 3 V.

The output of the A250 is amplified by an INA110 instrumentation amplifier with a gain of 10. The *dc* voltage is measured by an INA110 amplifier with a gain of 500. The *dc* current signal is the output of the A250 followed by an INA110 amplifier with unity gain. Both *dc* signals are followed by an ISO100 optical isolation amplifier with unity gain to keep the noise from feeding back into the electronic circuit.

The cryostat and the electronics are put into a $1.6\times1.6\times1.6\mathrm{m}^3$ electromagnetic shielding box. The shielding box reduces the electronic pickup in the superconducting coils and keeps the magnetic field stable. But it cannot effectively reduce the noise below 1 kHz. In the future the magnetic shielding can be used to eliminate the 60 Hz noise from the power line.

The *dc* outputs are connected to the shielding box by BNC cables. After passing through a T filter with a bandwidth of 20 kHz outside the shielding box they are displayed on an XY recorder. The *ac* outputs sent out by triax cables go through the shielding box and get amplified by other op-amp INA110s with a gain of 10 to reduce the effect of the ground loop noise outside the shielding box. Following each INA110 there is a T filter with a bandwidth of 200 kHz. The final amplified signals are sent to an oscilloscope.

We use a Nicolet Integra 40 digital oscilloscope. The Integra 40 has twelve bits of voltage resolution and a sampling frequency of 200 MHz. The noise contribution from the digitized noise of Integra 40 is negligible compared with other noise sources. The Integra 40 also has a long memory length which allows us to study low frequency noise and bias voltage fluctuations. But this oscilloscope generates a digitized 200 MHz noise from the digital system. Even though this noise is not in the signal band, without the 200 kHz T filter it could have propagated through the triax cable and coupled to the electronics inside the shielding box to cause the marginally stable A250 to oscillate and trap flux inside the junctions. The T filter protects the electronics from the noise higher than 200 kHz. The current signals or the electronic noise are downloaded from the oscilloscope to a computer by LabVIEW or Igor acquisition software. The data is saved to the disk and can be studied in an unfiltered form or by applying digital filtering routines to filter out the electronic noise and attain the optimum energy resolution. The noise spectra are obtained after applying the Fourier transform to the electronic noise.

To test the electronics noise we inject current pulses from an HP33120A waveform generator through a 1MΩ resistor into the amplifier input with the junction connected. To find the relation between the current noise and the energy resolution, first we test the electronic current noise without signals, and then inject the signals into the electronics. Following the same procedure that is used for analyzing real x-ray signals, we analyze the energy broadening of the injected pulses caused by the electronic noise.

Chapter 4 Optimization of Al Junctions

Al junctions are used to detect the number of quasiparticles created by the x-ray photons in a Ta absorber. The optimization of the Al junctions is critical in improving the detector performance. This chapter analyzes the current designs and how to improve on them.

The first half of this chapter discusses the design issues related to the junction geometry. The optimization of the junction geometry can effectively reduce the Josephson effects (Josephson current and Fiske mode) on the junction voltage biasing. The measurement results of the junctions with different geometries are discussed. We also show some results of a Nb based annular junction.

The second half discusses possible junction designs that can increase the quasiparticle tunneling time. Longer quasiparticle tunneling time improves the quasiparticle cooling in the junction. One design has an increase in the Al trap volume relative to the junction size. A recently designed device B has a smaller junction size than device A, but it has a larger ratio of trap volume to junction area than device A. By thoroughly analyzing the noise sources of devices, we find the new design reduces two noise sources – voltage noise and bias voltage fluctuations [Li, 01b], which are the dominant noise sources of device A due to incomplete quasiparticle cooling in the junction. The energy resolution of the detector is improved by a factor of two. Another possible way to improve quasiparticle cooling is to reduce the barrier transparency by increasing the thickness of the junction insulator layer.

4.1 Junction Geometry Design

Josephson current and Fiske modes are the two major issues that we have to deal with in designing the geometry of the tunnel junctions. In order to *dc* voltage bias the junction, the Josephson current has to be suppressed by applying a magnetic field parallel to the junction. The existence of a high magnetic field increases the probability of trapping flux in the junctions. Any component of the magnetic field perpendicular to the junction plane can cause magnetic flux to be trapped inside the superconducting film. Once there is trapped flux in the superconducting film, the energy gap in the trapped region is reduced. The quasiparticles in the trapped flux region will eventually be lost by recombination. So trapped flux reduces the quasiparticle lifetime.

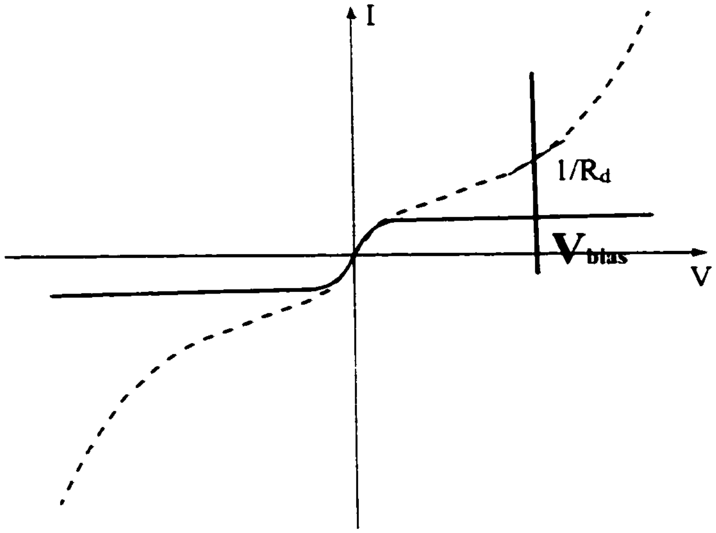

Fig. 4.1 I-V curves with and without trapped flux. The dashed line is the I-V curve with trapped flux, the solid line without trapped flux.

The trapped flux in the junctions also increases the subgap current substantially. The comparison of the I-V curves with and without trapped flux is shown in Fig. 4.1. The dashed line is the I-V curve with trapped flux, while the solid line is without trapped flux. The tunneling current with trapped flux is much bigger than the current with no trapped flux. This increase worsens the shot noise, which is proportional to $\sqrt{2eI}$. In addition, the trapped flux increases the current noise caused by the amplifier voltage noise e_n, because the dynamic resistance R_d of the I-V curve with trapped flux is much smaller than that without trapped flux.

Generally speaking trapped flux seriously degrades the performance of the devices. The energy resolution can be dramatically worse when there is trapped flux in the junction. Trapped flux can be generated not only by a magnetic field perpendicular to the junctions, but also by a transient current flowing through or near the junctions. To reduce the chances of trapping flux in our detectors, we need to use the smallest field possible and improve the stability of the electronics.

The second design issue of the junction geometry is the Fiske modes. The maximum practical bias voltage is Δ_{Al} = 180 μV because the multi-quasiparticle tunneling current increases sharply at Δ_{Al} [Schreiffer, 63]. The existence of Fiske modes in the I-V curve below Δ_{Al} limits the voltage bias region. If the junction is biased in the Fiske mode region, the noise is dramatically higher. The resonance in the junction causes the electronics to be unstable and the amplitude of the Fiske modes changes with the magnetic field. For device A the first Fiske mode is at about 100μV, which limits the bias voltage region to be below 80μV. The low voltage bias induces both the voltage noise and the bias voltage fluctuations (see Sec 4.2.1) due to the incomplete cooling of quasiparticles in device A. The solution to this problem is to move the first Fiske mode close to or above 180 μV so that the junction can be biased at a higher voltage. Therefore we need to first understand the relation between the Fiske modes and the geometries of the junctions.

The voltage where Fiske resonance modes are located is related to the electromagnetic cavity modes of the junction. From Eq. (2.22) we know that the longer and wider the junction, the lower the resonant frequency and the lower the voltage of the Fiske modes.

4.1.1 Quartic and Diamond Shaped Junctions

To avoid the trapped magnetic flux, we try to use the smallest possible magnetic field to suppress I_c. A lot of efforts have been devoted to finding the optimal STJ geometry to suppress I_c by a small parallel magnetic field [Peterson, 91; Gijsbertsen, 95; Nappi, 91; Kikuchi, 00]. Fig. 2.5 shows how different geometries of the junctions produce different I_c profiles for the same magnetic field. The I_c of the quartic shaped junction decreases much more quickly than that of the rectangular shaped and diamond shaped junctions. For the junctions with the same area, the longer the junction in the direction perpendicular to the magnetic field, the easier I_c can be suppressed. That is why we initially chose the 200 μm long quartic junctions (device C). But in the long junction the Fiske modes occur in the region where we want to bias the junction.

The 200 μm long junction (device C) is easily suppressed by a small magnetic field, but it shows a Fiske mode at 90 μV. After improving the fabrication and experimental techniques, the dc Josephson current of the junctions can be suppressed by a magnetic field up to 70 Gauss without increasing the probability of trapping flux. After the improvements of the electronics (Chapter 3), the transient current is better controlled and the chance of getting trapped flux becomes lower. This gives us space to reduce the longitudinal dimension of the junction so that the Fiske mode can be shifted to a higher voltage. Consequently the first Fiske mode of device B is successfully moved up to 150 μV since device B has the same shape as device C, but smaller tunnel junctions. The bias voltage range is almost increased by a factor of two.

If the junction area and the trap volume become small enough, the self-recombination effect has to be considered since it reduces the charge collected and causes a nonlinear response for high energy x-ray photons. So there is a lower bound limit on the junction dimension. It is important to keep the junction area and the trap volume above the self-recombination limit while reducing the longitudinal length of the junction to eliminate the Fiske modes. Since the shape of the junction might change, we have to recalculate the location of the Fiske modes. The quartic shaped junction has a complicated boundary. It is very difficult to solve the differential equation (2.19) exactly. Thus we approximate the Fiske mode voltages of the quartic shaped junctions by the diamond shaped junctions with the same width and length. We use this approximation to find the length of the junctions so that there is no Fiske mode lying below Δ_{Al}. Table 4-1 lists the numerically calculated results with the assumption that the first Fiske mode of a 200 × 18.6 μm^2 diamond shaped junction is at 90 μV. The first Fiske mode of a 64 × 64 μm^2 diamond shaped (square) junction is then 230 μV, which is well above Δ_{Al}.

Junction length [μm]	200	120	64
Junction width [μm]	18.6	11.2	64
First Fiske Mode [μV]	***90******	150	237

Table 4-1 Estimates of the first Fiske mode of diamond shaped junctions. *The first Fiske mode of the junction with dimension 200 x 18.6 μm^2 is assumed to be 90 μV according to experimental measurements.

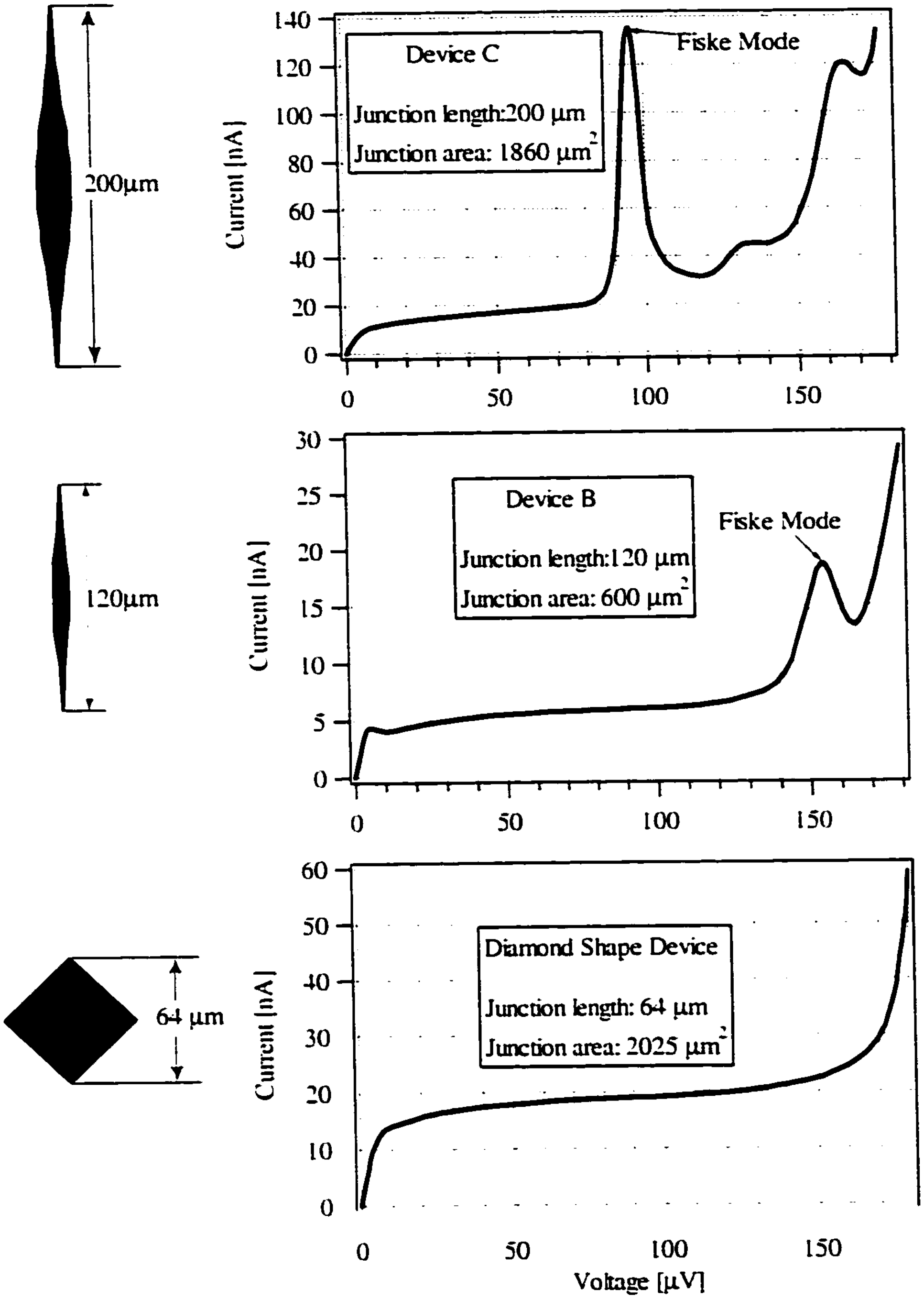

Fig. 4.2 I-V curves of quartic shaped and diamond shaped (square) junctions. The Fiske mode of the 200 μm long junction is at 90 μV, and the Fiske mode of the 120 μm long junction is at 154 μV. There is no Fiske mode below Δ_{Al} = 180 μV for the 64 × 64 (square) junction. (device B, 5/17/00; device C, 7/26/00; device F (diamond shaped junction), 3/6/01)

The quartic and diamond shaped junctions with the geometries mentioned in Table 4-1 have been tested and the I-V curves are shown in Fig. 4.2. The 64×64 diamond shaped junction shows no Fiske mode below the aluminum energy gap 180 μV as we calculated. Since the subgap current starts to increase at 150 μV, the practical junction bias voltage range is below 150 μV. A sharp current jump at 180 μV is related to two-quasiparticle tunneling [Schreiffer, 63]. The onset of the current increase depends on the base temperature. It will be closer to 180 μV as the base temperature becomes lower and the bias voltage region can be extended higher. But there is little room to go above 150μV.

4.1.2Annular Junctions

Maintaining a continuous and stable magnetic field to suppress the Josephson current during the x-ray detection adds complexity to the measurement, especially for applications that will go into the space.

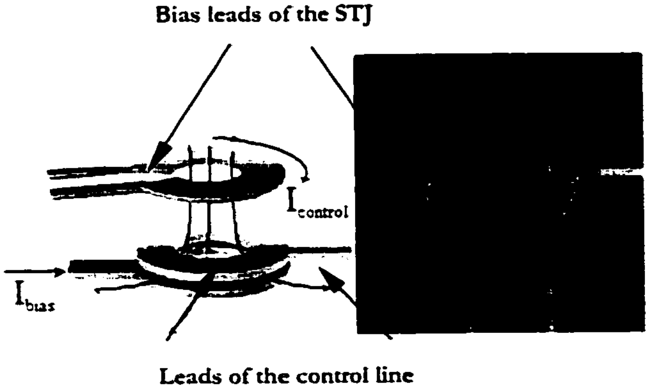

Fig. 4.3 Schematic "exploded view" of the annular STJ with a single trapped fluxon. The film thickness is not to scale. The control line coil is on top of the STJ. The magnetic field lines threading the barrier are shown.

The annular junction provides an alternative for achieving the suppression of I_c without any external field. It traps fluxons inside the central holes as shown schematically in Fig. 4.3. The magnetic fluxons trapped inside the annular junction are quantized because the phase of the junction follows the periodic boundary condition. The n trapped fluxons in the tunnel barrier causes the superconducting phase difference, $\Delta\varphi$, to increment by exactly $2n\pi$ around the loop. I_c is zero because it is the integral of the current density $J_c \sin\varphi$ along the loop. Thus the Josephson current can be completely suppressed by the magnetic fluxons even without any external magnetic field.

Fig. 4.3 shows the exploded view of an annular tunnel junction. These kind of junctions have a stack structure with four layers Nb/Al-AlO$_X$/Nb fabricated on an oxidized Si wafer at HYPRES Inc. [Radparvar, 95]. The critical current density is J_c=100A/cm^2. The radius ratio is $\delta = R_{in}/R_{ext}$ = 0.5 with R_{ext}=16 μm. The estimated Josephson penetration depth is λ_J = 37 μm. Theoretically the self-fields of the junction can be ignored if the STJ is "small". In the annular junction case, the necessary condition is $R_{ext} < \lambda_J$ for an externally applied parallel magnetic field or $R_{ext} < n\lambda_J \sqrt{\frac{\ln\delta}{\delta^2 - 1}}$ for n trapped magnetic fluxons [Nappi, 96]. Both conditions are satisfied in our device. The detector has 3.5 μm wide leads connecting the electrodes to the external read-out electronics. The STJ normal resistance is R_V =3.5Ω.

A Nb control line in the form of a single turn coil is deposited coaxially on top of the annular junction. The control line is used either to supply a perpendicular magnetic field to the device for trapping fluxons during the cooling, or to heat the device above T_c. A SiO$_2$ layer insulates the control line from the detector. The integration of the control line on the chip is intended to avoid using external coils to generate the perpendicular magnetic field required to trap fluxons.

In the x-ray photon detection measurement we use two different field configurations. In the first configuration, we use an external magnetic field applied parallel to the junction to suppress the Josephson current as typically done for other junctions. Then the annular STJ detector is voltage biased. The field remains during the photon detection process. In this configuration, there is no trapped fluxon in the junction. The measured I-V curve of the device is shown in Fig. 4.4 as the dashed line with condition T = 0.21 K and a parallel magnetic field of H=60.6 Gauss. We voltage bias the device at V = 680 μV. The maximum charge collected from the STJ is 1.1×10^5 electrons without filtering.

This is only about 4% of the predicted total quasiparticle charge. Similar charge losses are seen for other Nb-based STJs [Cristiano, 95] that use a thin Al layer.

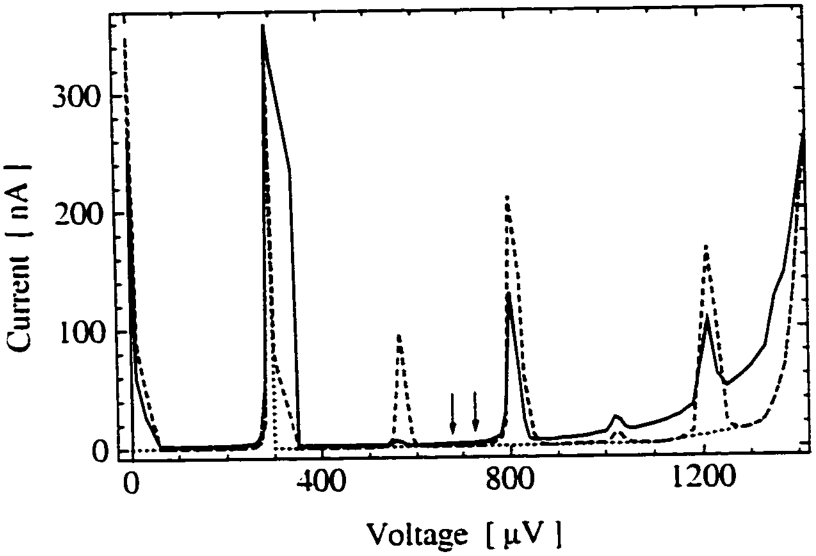

Fig. 4.4 I-V characteristics of the annular junction. The dashed line is measured at 0.21 K without trapped flux and a parallel magnetic field of 60.6 Gauss. The solid line is measured at 0.24 K with one trapped fluxon and a parallel field of 63.4 Gauss. The dotted line is the expected curve without the parallel field. The two arrows represent the voltage bias points used.

In the second configuration [Vernik, 96], a flux quantum is trapped in the annular junction to suppress the Josephson current and no external field is applied during the x-ray photon measurement. To trap a magnetic fluxon in the STJ barrier, we first apply a large current to the control line at $T = 4.2$ K to drive it into the normal state and then use it as a local heater to drive the STJ normal. Then we quickly reduce the control line bias to a smaller current. This allows the annular junction to become superconducting in the presence of a perpendicular magnetic field in the order of 0.2 Gauss produced by the control line. The magnetic field would have been enough to produce two fluxons in the area of the STJ hole if the field only threads through the barrier.

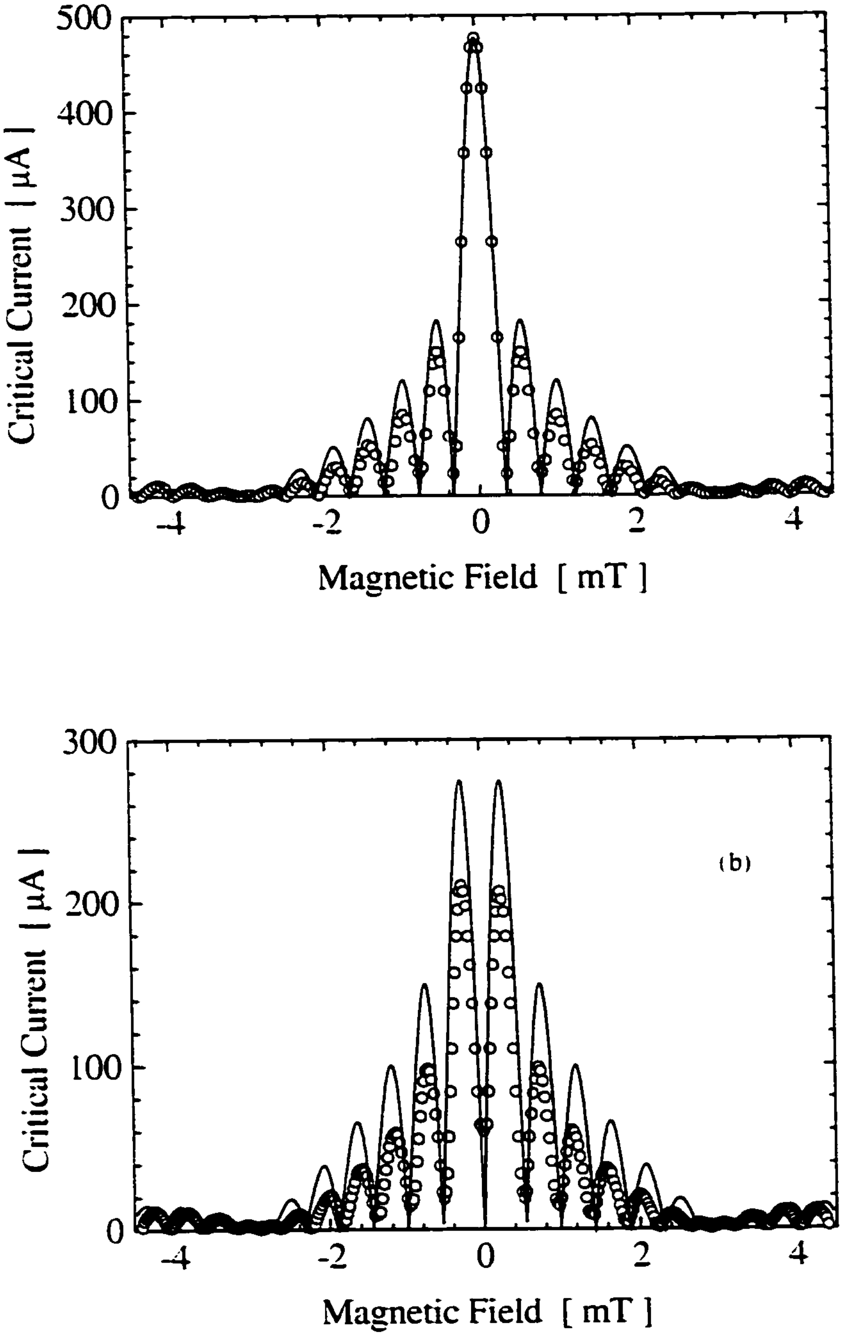

Fig. 4.5 I_c vs. H of the annular junction. The dots represent the experimental data and the solid line the theoretical prediction. Panel (a) is at $T = 0.21$ K without trapped fluxons and (b) at $T = 0.24$ K with a single fluxon trapped in the STJ barrier.

We successfully trapped one fluxon in the annular junction barrier during the transition to the superconducting state, as shown schematically in Fig. 4.3. However, the trapping procedure is not fully repeatable. To obtain more repeatable results, we expect that annular STJs without a hole in the base electrode will be helpful.

To check whether a single fluxon was trapped in the annular junction, we measure both the $\boldsymbol{I_c}$ vs. $\boldsymbol{H}$ and the I-V curve. The signature of a single trapped fluxon trapped in the annular STJ barrier is an almost completely suppressed $\boldsymbol{I_c}$ and the presence of only the first Fiske resonance on the I-V curve without magnetic field [Cristiano, 99]. Fig. 4.5a shows $\boldsymbol{I_c}$ vs. $\boldsymbol{H}$ (dots) at $\boldsymbol{T} = 0.21$ K with no trapped flux in the annular junction compared to the theory (solid line) [Nappi, 97]. This shows a quite good agreement. Fig. 4.5b shows the observed $\boldsymbol{I_c}$ vs. $\boldsymbol{H}$ (dots) with a single fluxon trapped in the junction compared to the theoretical prediction (solid line) [Nappi, 97]. $\boldsymbol{I_c}$ has been reduced to about 2.5% of $\boldsymbol{I_c}$ at zero bias voltage and zero magnetic field, but does not achieve the ideal value of zero. Also the measured maxima are lower than expected. These minor disagreements can be attributed to the presence of some Abrikosov vortices trapped in the electrodes [Cristiano, 99]. With a single fluxon trapped in the junction, the first Fiske mode stays in the I-V curve shown in Fig. 4.4. Other Fiske modes have not been completely suppressed. This is probably caused by the Abrikosov vortices.

Once we observe these signatures, we cool the device to $\boldsymbol{T} = 0.24$ K. Because $\boldsymbol{I_c}$ is finite without a magnetic field, we have to initially use an external parallel magnetic field to suppress the residual $\boldsymbol{I_c}$ and then switch to voltage bias the annular STJ. The I-V curve of the device is shown as solid line in Fig. 4.4 at $\boldsymbol{T} = 0.24$ K and $\boldsymbol{H} = 63.4$ Gauss. The expected curve with no parallel field (dotted line) is also shown as a comparison.

To detect photons with one trapped fluxon, we bias the detector at $\boldsymbol{V} = 725\ \mu$V and have the externally applied parallel magnetic field turned off during the measurement. We acquire single photon current pulses. These pulses appear to be just like those observed in the first configuration. The fluxon stays trapped during the x-ray irradiation. The maximum collected charge is $1.7\text{x}10^5$ electrons without filtering. The energy resolution obtained is very poor, which is typical for such Nb-based STJs. The worse performance is mainly caused by the following factors: quasiparticle loss in the polycrystalline Nb electrodes, outdiffusion into the leads, self-recombination, and the presence of substrate events that overlap in time with the x-ray current pulses. There are several steps that can improve the performance. The use of Al traps [Booth, 87; Mears, 93] can reduce the quasiparticle loss in the polycrystalline Nb electrodes and accelerate quasiparticle tunneling. Inserting a short section of higher energy gap superconductor into each of the leads can reduce outdiffusion [Wilson, 00].

In summary we have successfully trapped one fluxon in the annular junction to suppress the Josephson current. Without applying external magnetic field the x-ray photon detection has been done with the one trapped fluxon. However, we need to develop a repeatable procedure to trap fluxons. We expect such a procedure can be helped by fabricating an annular junction without a hole in the base electrode. Using Ta as a photon absorber and Al annular junctions as quasiparticle detectors can reduce the quasiparticle loss that happens in Nb based junctions.

4.2 Improving Junction Performance

The STJ detector research in this lab has gone through the processes of device fabrication, electronics design, and improvement of performance. After understanding the various noise sources and mastering new experiment techniques, we have improved our device energy resolution step by step from 190 eV (one junction) [Gaidis, 94], to 54 eV [Stephan, 97], to 26 eV [Segall, 00], and to 13 eV [Li, 01].

4.2.1 Problems of Device A

The best energy resolution of the previous device A is 26 eV. The noise sources were well studied in Ref. [Segall, 00]. In addition to the device's intrinsic noise sources that were introduced in Chapter 2, the two dominant electronic noise sources in measuring device A are the amplifier voltage noise e_n and the bias voltage fluctuations ΔV. The equivalent current noise of the amplifier voltage noise is given by e_n/R_d while the bias voltage fluctuation ΔV leads to the change of charge response ΔQ. The cause of these two noises is due to the incomplete cooling of quasiparticles in the Al junction region. The other noise sources, such as Johnson noise of the feedback resistor i_{nJ} and the shot noise of subgap current $i_{n,s}$, contribute about 10 eV to the energy broadening. In Fig. 4.6 we show the schematic of the electronic circuit with electronic noise sources in it.

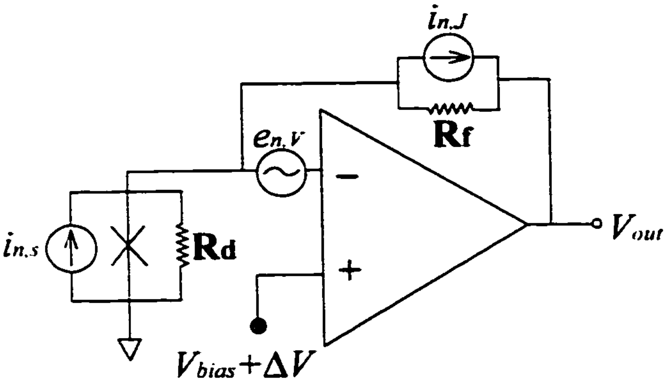

Fig. 4.6 The schematic of the electronic circuit together with the corresponding electronic noise sources. e_n is the voltage noise of the amplifier. V_{bias} is the bias voltage and ΔV is the bias voltage fluctuation. $i_{n,J}$ is the Johnson noise of the feedback resistor. $i_{n,s}$ is shot noise from the tunnel junction. R_d is the dynamic resistance of the junction during the signal pulse.

4.2.1.1 Incomplete Cooling

After the quasiparticles diffuse from the Ta absorber into the Al trap, the quasiparticles scatter down to lower energy levels in the Al trap by emitting phonons. If the scattering time of the quasiparticles in the Al trap is too long, incomplete cooling of the trapped quasiparticles results. The scattering time in the Al trap is on the order of μs when the quasiparticle energy is close to the Al gap energy (180 μV) even though the scattering time is about 10 ns when the quasiparticle has the Ta gap energy (700 μV). If the tunneling time of the quasiparticles is shorter or comparable to the quasiparticle scattering time or cooling time, the quasiparticles can tunnel before they completely cool down. If the quasiparticle energy is higher than eV_{bias}, the hole-like quasiparticles can tunnel from the trap to the counter-electrode and quasiparticle can reverse tunnel from the counter-electrode to the trap (see Fig. 2.3). They then cancel the forward tunneling current. The higher the bias voltage, the less the reverse current (called cancelling current), and the more the net current. For the incompletely cooled quasiparticle system the total measured charge increases as a function of the bias voltage, while in the equilibrium case or completely cooled situation the measured charge is almost independent of the bias voltage. So for incompletely cooled quasiparticle tunneling, any fluctuations in the bias voltage will cause fluctuations in the measured charge as depicted in Fig. 4.7. Since the charge vs. bias voltage has a slope in the incomplete cooling situation, a change in the bias voltage ΔV corresponds to a change in measured charge ΔQ. For the same amount of bias voltage fluctuation the change in the measured charge becomes smaller when the bias voltage is higher.

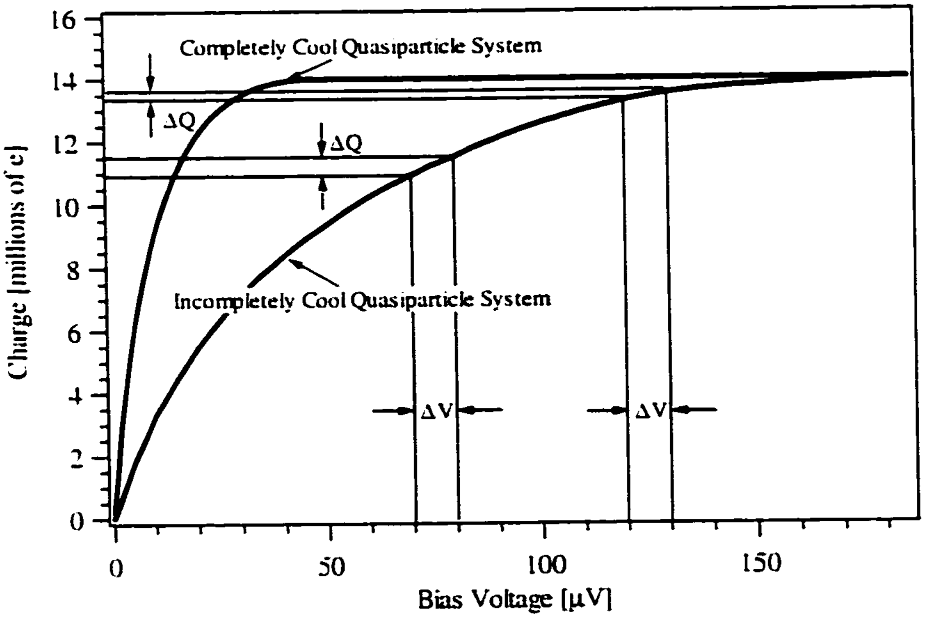

Fig. 4.7 The total collected charge as a function of bias voltage for completely and incompletely cooled quasiparticle system [Segall, 00b].

When there is no x-ray event, the dynamic resistance R_d is larger than 10kΩ in the bias region. Corresponding to the voltage noise of $e_n = 0.4\ \mathrm{nV}/\sqrt{\mathrm{Hz}}$, the equivalent current noise is $i_n = e_n/R_d = 40\ \mathrm{fA}/\sqrt{\mathrm{Hz}}$, which is negligible compared to the Johnson noise of the 1M Ω feedback resistor $\sqrt{4kT/R_f} = 130\ \mathrm{fA}/\sqrt{\mathrm{Hz}}$. But when there are x-ray events, because the quasiparticles are not completely cooled in the junction, the tunneling current of the excess quasiparticles will increase as the bias voltage increases. The effective I-V curve is shown in Fig. 4.8 for $eV_{bias} < kT^*$, where T^* is the effective temperature of the quasiparticle system in the junction. Therefore for device A the dynamic resistance R_d is about 1.5 kΩ which is much smaller than that at the quiescent state (no x-ray events). The effective voltage noise is about 6 times larger than that at the quiescent state. Since there is no x-ray signal during the injection test, neither the charge fluctuations nor the voltage noise can be measured by the injection test that is used to calibrate the electronic noise of the circuit. These two noise sources account for the majority of the discrepancy between the measured energy resolution of 26 eV and the electronic noise of 13 eV.

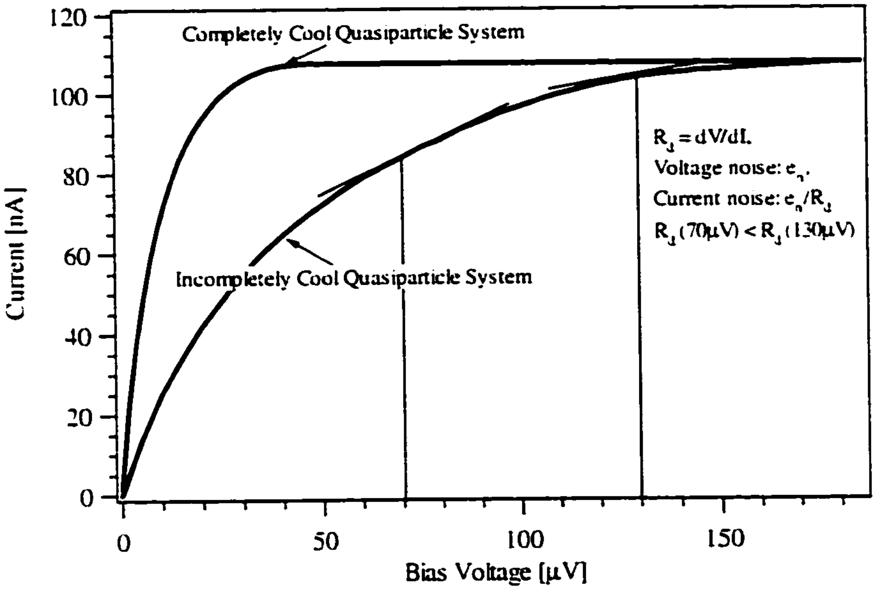

Fig. 4.8 The peak current as a function of the bias voltage for the incompletely cooled quasiparticle system [Segall, 00b].

There are two ways to reduce those two noise sources. The dQ/dV value decreases as bias voltage V_{bias} increases, while the dynamic resistance $R_d = dV/dI$ increases as V_{bias}. By increasing the bias voltage, we can reduce the noise caused by the bias voltage fluctuation and the voltage noise of the amplifier. However, the bias voltage of device A is limited to 80 μV because of the existence of the first Fiske mode at 100μV. In order to increase the bias voltage, we must resort to the possible ways discussed in 4.1 to eliminate the Fiske modes below the Al energy gap (180μV). The second way is to increase the thickness of the AlO_x insulator layer. Since the tunneling probability is inverse exponentially proportional to the barrier thickness, reducing the transparency of the barrier leads to increased tunneling time. We can also have longer quasiparticle tunneling time by increasing the ratio of the trap volume to the junction area. So by changing the design of the junction, we can increase the quasiparticle tunnel time to better cool the quasiparticles before they tunnel.

4.2.1.2 Johnson Noise of the Feedback Resistor

The feedback resistor R_f at room temperature adds a large current noise to the measurement. The feedback resistor in this setup is chosen to be 1MΩ. The Johnson noise of the feedback resistor $i_{n,J}$ is given by $\sqrt{4kT/R_f}$. The higher the resistance, the lower the noise. This noise is about 130 fA/$\sqrt{\text{Hz}}$ at room temperature and is one of the dominant electronic noises at the quiescent state. It seems that by just increasing the feedback resistance, the noise can be further reduced. But there are two limiting factors, the signal bandwidth and the slope of the load line. Because the feedback circuit has a stray feedback capacitor C_f of about 1pf, increasing the feedback resistor will reduce the signal bandwidth that is limited to $f = 1/(2\pi R_f C_f)$. The second factor is the load line resistor, which is equal to $R_{bias} + R_f / G_{amp}$, where $R_{bias} = 4\ \Omega$ is the bias resistor and $G_{amp} = 5\times10^5$ is the *dc* open loop gain of the current amplifier [Friedrich, 97]. When $R_f = 1$ MΩ, the load line has a slope of 6 Ω. The load line of a 100 MΩ feedback resistor becomes about 200Ω. The voltage bias with a load line of 200 Ω is much more restrained by the Josephson current and less stable than a 6 Ω load line (see Section 3.3). Considering all the factors we chose a 1MΩ feedback resistor. So instead of increasing R_f to reduce the Johnson noise of the feedback resistor, the alternative is to cool the resistor down to low temperature.

4.2.1.3 Shot Noise of the Junctions

At the measurement temperature $T = 0.21$ K, there are some thermally excited quasiparticles in the Al junction. The tunneling of these thermal quasiparticles creates the subgap current. The subgap current I gives rise to the shot noise $i_{n,s} = \sqrt{2eI}$. The shot noise of device A is about 100 fA/$\sqrt{\text{Hz}}$, which is the second known dominant electronic noise in the quiescent state. If the area of the junction is reduced, the tunneling current becomes smaller as does the shot noise. Because the subgap current exponentially decreases as a function of the temperature (see Eq. (2.14)), lowering the working temperature of the junction reduces the shot noise. One group [Gubrud, 01] has measured the subgap current of Al junctions as a function of temperature. They observe that the current follows BCS theory down to 0.15 K. By lowering the temperature down to 0.15 K the subgap current can be reduced by at least a factor of 10.

4.2.2 Junction Improvement — Device B

After we understand all the major problems of device A, the design of the junctions can be optimized accordingly.

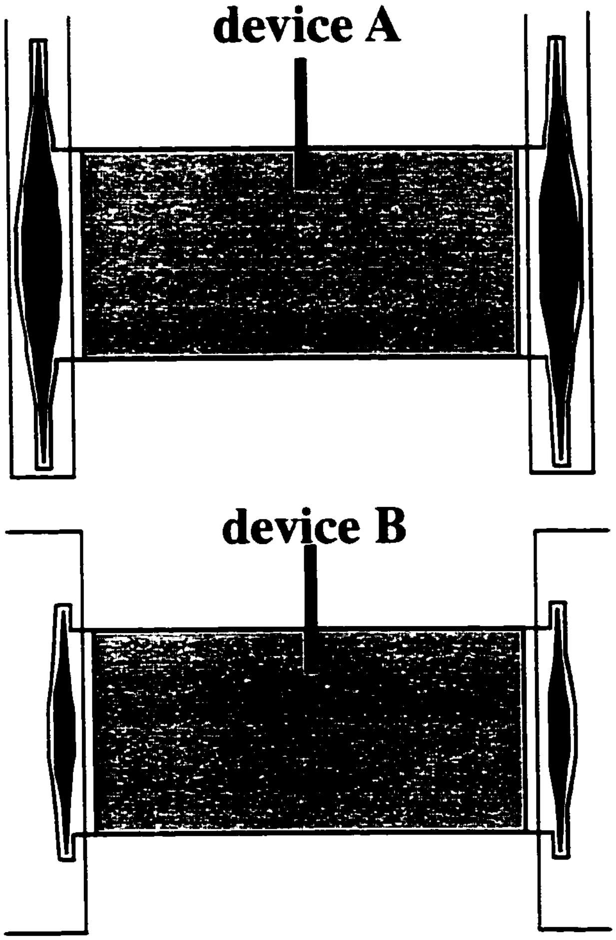

Fig. 4.9 The top views of device A and device B. The light gray area is the Ta absorber. The black region is the junction. The white region is Al. A thin Nb lead ground contact connects to the center of the absorber.

4.2.2.1 The Junction Design of Device B

Based on the understanding of various noise sources, device B is designed to improve the quasiparticle cooling. The top views of device A and B are shown in Fig. 4.9. Both devices have the same sized Ta absorber and Nb lead ground contact at the center of the absorber. Compared to device A, the linear dimension of the junctions of device B is scaled down by a factor of 1.67. So the junction area of device B is only about 1/3 of that of device A. The longitudinal dimension of the junctions in device B is 120 μm, while it is 200 μm in device A. The Al trap volume of device B is about 70% of the trap volume of device A. So device B has a relatively larger ratio of trap volume to trap area. Device B also has a wider wiring pad to allow fast outdiffusion to reduce the backtunneling noise.

4.2.2.2 The Performance of Device B

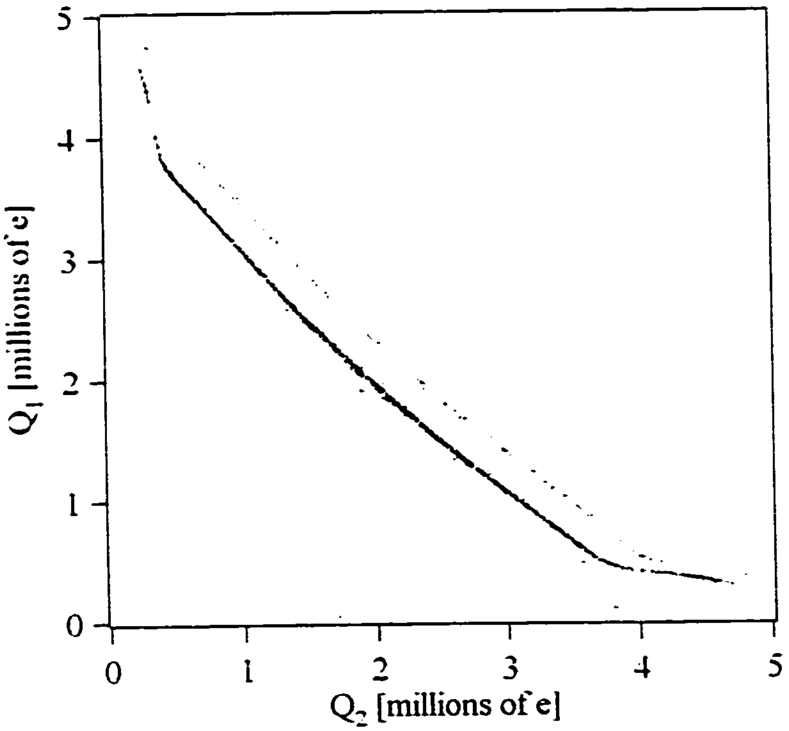

Fig. 4.10 Q_1 vs. Q_2 for device B after the signals are band pass filtered to achieve the best energy resolution. (device B, 6/4/00; Filter: Chebysshev, 4th order, 4-86 kHz)

By changing the junction design, we not only improved the quasiparticle cooling in the junctions, but also increased the bias voltage from 80 μV to 120 μV with the first Fiske mode at about 150μV. These two major improvements dramatically reduced the two dominant electronic noises. We also reduced the Johnson noise of the feedback resistors by cooling down the resistors to 1.5 K. With all the improvements device B demonstrated a very good performance. We achieved 13 eV energy resolution for the 5890 eV x-ray photons in a 20 μm region near one side of the Ta absorber. Fig. 4.10 shows the Q_1 vs. Q_2 data after filtering out high and low frequency current noises. Each black dot represents a single x-ray photon event. There are two lines in the figure, one is the K_α line with less total charge but more events and the other is the K_β line with more total charge but fewer events. The events that are lower than the K_α line are the substrate events. There is no event below 1.5 million electrons due to the trigger level. The up-bending at the two ends of the K_α and K_β line is due to the absorption events that occurred in the Al and Ta absorber overlapping region. Because the energy gap of the proximitized Al is lower than Ta energy gap (section 5.3.1), x-ray photons generate more quasiparticles in the overlapping region than in the Ta absorber.

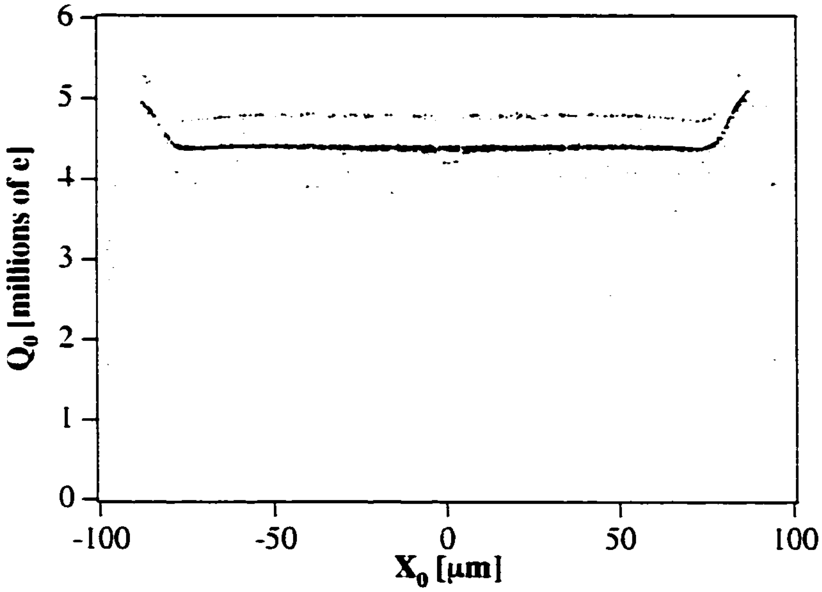

Fig. 4.11 Total charge as a function of absorber location, corrected for the quasiparticle loss. (device B, 6/4/00)

To analyze the data, we convert the Q_1 vs. Q_2 plot to Q_{total} vs. x (Fig. 4.11) by applying the Kraus formula [Kraus, 89]. After adjusting the loss parameter α(see Eq. (5.5)) to restore the quasiparticle loss in the Ta absorber, we pick a region from –55 μm to –75 μm to build the energy histogram as shown in Fig. 4.12. In this region, the detector shows the best energy resolution. It becomes worse when the events are closer to the center. We believe the broadening of the energy resolution in the central region is caused by the Nb contact. More discussion about the spatial non-uniformity caused by the Nb ground contact is given in Section 5.1. The energy resolution on the other side of the detector is a little worse, which is due to the excess low frequency electronic noise of the amplifier used for that tunnel junction. This appears to be due to the individual performance of the A250 amplifier.

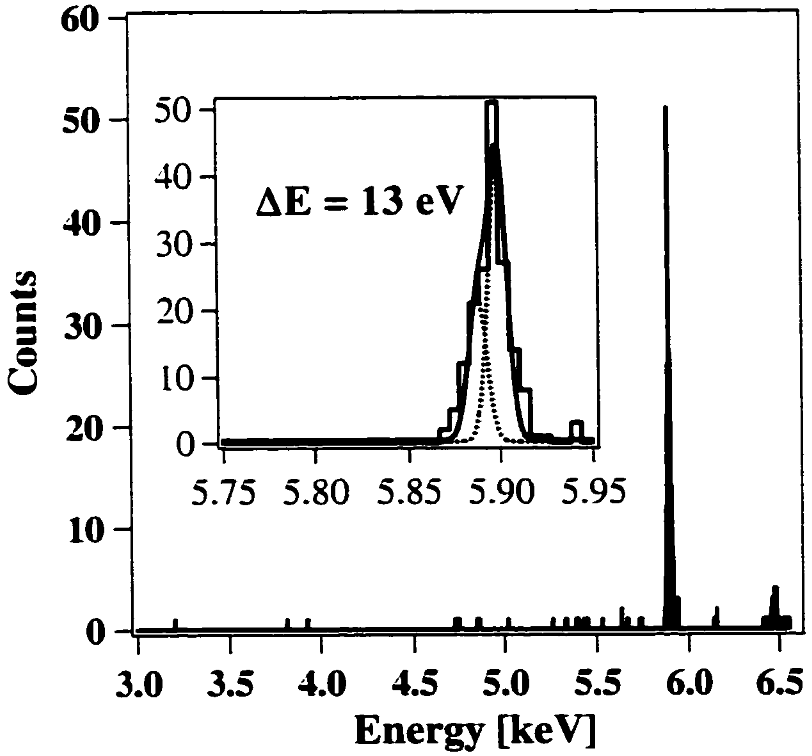

Fig. 4.12 The energy spectrum over a 20 × 100 μm^2 range of the Ta absorber illuminated by the ^{55}Fe source. The inset shows the magnification of the Mn K_α line and the fitting of the double peaks of $K_{\alpha 1}$ and $K_{\alpha 2}$. (device B, 6/4/00)

The measured energy resolution is 36eV FWHM if all events in the whole absorber are considered. The energy resolution of 13eV in the selected $20\times100\mu m^2$ range on one side of the absorber is about twice the intrinsic energy resolution of about 6 eV that this kind of devices can achieve. The performance of device B is one of the best of a recent study of different STJ detectors [Angloher, 01]. The energy spectrum in the selected $20 \times 100\ \mu m^2$ range with the energy resolution of 13 eV is shown in Fig. 4.12. The inset shows the double peak fitting of the Mn $K_{\alpha1}$ and the Mn $K_{\alpha2}$ line. In the next section we will quantitatively study each noise source contributing to the 13 eV energy resolution in hope of suggesting possible future improvements.

4.2.2.3 Noise Source Analysis

1) Device noise sources

The main device noise sources were introduced in Chapter 2. Let's now calculate them one by one for device B.

(1) Creation noise

The statistical noise caused by quasiparticle creation in the Ta absorber is given by Eq. (2.26). The Fano factor for Ta is $F = 0.22$, the average quasiparticle energy is $\varepsilon = 1.74\Delta$, where $\Delta = 700\ \mu V$ is the energy gap of Ta. For the photon energy of $E = 5895$ eV, the energy resolution given by the creation noise is $\Delta E_{FWHM} = 2.355\sqrt{F\varepsilon E} = 2.96\ \text{eV}$.

(2) Absorber loss

The statistical noise due to the quasiparticle loss in the absorber is given by Eq. (2.27). Device B shows a very small quasiparticle loss in the Ta absorber compared to device A. This is because the quasiparticle loss is caused by the Nb contact and the contact on device A is evaporated twice. Section 5.3 shows the experimental results of the quasiparticle lifetime. Assuming no quasiparticle loss in the Nb contact, the number of quasiparticles lost in the Ta absorber is about 4% of the initial charge assuming a loss parameter $\alpha = 0.75$. So the probability β that a quasiparticle is lost is 4%. The energy broadening due to the quasiparticle loss in the Ta absorber is thus 1.3 eV.

(3) Trapping Multiplication

When quasiparticles are trapped in the Al trap, the phonons emitted by the quasiparticles may break Cooper pairs to create more quasiparticles (trapping multiplication process). The statistical noise of the trapping multiplication process is given by Eq. (2.28). The trapping multiplication factor κ is obtained from the measured quasiparticle number and a numerical simulation with the assumption that there is no trapping multiplication (see Chapter 5). By fitting the actual pulse shape, we can infer the initial charge. The difference between the theoretically created charge and the simulated initial charge is the charge created in the trapping multiplication. The trapping multiplication factor is found to be $\kappa = 1.6$. The statistical noise of the trapping multiplication process is then $\Delta E_{multi} = 2.355\sqrt{\varepsilon E\left(\left(\kappa-1\right)\left(3-\kappa\right)/\kappa^{2}\right)}$ =3.6 eV.

(4) Backtunneling

The backtunneling noise is given by Eq. (2.29). Device B has a wider wiring pad than device A. The backtunneling and the noise due to backtunneling are expected to have less effect in device B than in device A. By analyzing the pulses the tunneling probability from the trap is $P_1 = 0.96$, while the tunneling probability from the counterelectrode is $P_2 = 0.19$. So in device B the average number of times that each quasiparticle tunnels is $\bar{n} = P_1(1+P_2)/(1-P_1P_2) = 1.40$ and the backtunneling factor is $G=0.58$. The backtunneling noise is then $\Delta E = 2.355\sqrt{G\varepsilon E}$ = 4.8 eV. Though the wide wiring pads help reduce backtunneling noise, the performance has not been as good as we have expected considering the backtunneling noise of device A is 5.9eV. Future improvements include putting normal metal on the wiring pad close to the junction. The normal metal will prevent quasiparticle backtunneling because once the quasiparticles are in the normal metal they will be trapped and flow away.

(5) Cancellation

The cancellation noise is given by Eq. (2.31). It depends on the bias voltage and the tunneling time. Because the first Fiske mode of device B is at approximately 150 µV, device B can be biased at 120 µV which is higher than that of device A. The tunneling time is also longer in device B than in device A so that the quasiparticles can cool down better. The cancellation factor γ for device B is about 5% to give a cancellation noise of $\Delta E_\gamma = 2.355\sqrt{\varepsilon E\left(4\gamma(1-\gamma)/\bar{n}(1-2\gamma)^2\right)} = 2.5$ eV.

(6) Self-recombination noise

In device B the measured charge ratio of K_β to K_α line is 1.09 instead of 1.10. The nonlinear charge response is caused by quasiparticle self-recombination.

We begin with a simple particle loss rate of $1-p$. Assume the number of particles at the beginning is N_0, at time t the number of quasiparticles becomes $N(t) = pN_0$. We use $n_i(t)$ ($i = 1 \ldots N_0$) to denote the existence of each particle at time t. $n_i(t)$ is either 0 or 1 depending on the loss probability $1-p$ and $n_i(0) = 1$. So

$$N(t) = \sum_{i=0}^{N_0} n_i(t). \tag{4.1}$$

In the self-recombination situation, two particles recombine into one pair, so these two particles are correlated. But they don't have any correlation with other particles. Now let us calculate $\sum_{j=0}^{N_0}\sum_{i=0}^{N_0}\overline{n_i(t)n_j(t)}$. If particle m and particle n recombine, then $\overline{n_m(t)n_n(t)} = p$ instead of p^2 because they are completely correlated, which means they disappear at the same time. At time t there are on average $\overline{N(t)} = \sum_{i=0}^{N_0}\overline{n_i(t)} = p(t)N_0$ particles left. The number of particles recombined is $(1-p)N_0$. So

$$\sum_{i,j}^{recombined}\overline{n_i(t)n_j(t)} = \left(N_0 - N(t)\right)\times p \le pN_0 \tag{4.2}$$

the variance of $N(t)$ in the recombination system is

$$\begin{aligned}
&\overline{\left(N(t)-\overline{N(t)}\right)^2} = \overline{N(t)^2} - \overline{N(t)}^2 \\
&= \sum_{i=0}^{N_0}\overline{n_i^2(t)} + \sum_{j=0}^{N_0}\sum_{i=0}^{N_0}\overline{n_i(t)n_j(t)} - \left(\sum_{i=0}^{N_0}\overline{n_i(t)}\right)^2 \\
&= \left[pN_0 + \sum_{j=0}^{N_0}\sum_{i=0}^{N_0}\overline{n_i(t)}\;\overline{n_j(t)} - \left(\sum_{i=0}^{N_0}\overline{n_i(t)}\right)^2\right] + \sum_{i,j}^{recombined}\overline{n_i(t)n_j(t)} - \sum_{i,j}^{recombined}\overline{n_i(t)}\;\overline{n_j(t)} \\
&\le p(1-p)N_0 + pN_0 - p^2N_0 = 2p(1-p)N_0
\end{aligned} \tag{4.3}$$

The energy resolution caused by self-recombination noise is

$$\Delta E_{self} \leq 2.355\sqrt{\varepsilon E \frac{2(1-p)}{p}} \tag{4.4}$$

which is about 5 eV for device B.

Process	F_{eff}	Device B Statistical noise	Device A Statistical noise
Creation	F	2.96 eV	2.96 eV
Absorber Loss	$\frac{\beta}{1-\beta}$	1.3 eV	2.3 eV
Trapping Multiplication	$\frac{(\kappa-1)(3-\kappa)}{\kappa^2}$	3.6 eV	3.6 eV
Backtunneling	G	4.8 eV	5.9 eV
Cancellation	$\frac{4\gamma(1-\gamma)}{\bar{n}(1-2\gamma)^2}$	2.5 eV	4.1 eV
Recombination	$\frac{2(1-p)}{p}$	5.2 eV	0 eV

Table 4-2 Intrinsic device noise sources for device B and device A.

Putting all the noise sources together, Table 4-2 lists the intrinsic noise sources for both device A and device B. The total statistical device noise for device B is 8.9 eV, while the total statistical noise for device A is 8.9 eV. Device B shows about 5 eV self-recombination noise. But it can be reduced by keeping the junction area the same and increasing the trap volume. At the best estimate the minimum statistical noise from this kind of detectors is around 5.4 eV with zero backtunneling and zero self-recombination noise.

*2) **Electronic noise sources:***

In the previous section we reviewed the noise sources for device A. We knew that the two dominant electronic noise sources are the voltage noise of the amplifier and the bias voltage fluctuations. There are other electronic noise sources such as the Johnson noise of the feedback resistor and the shot noise of the junction, which can be calibrated by the injection test.

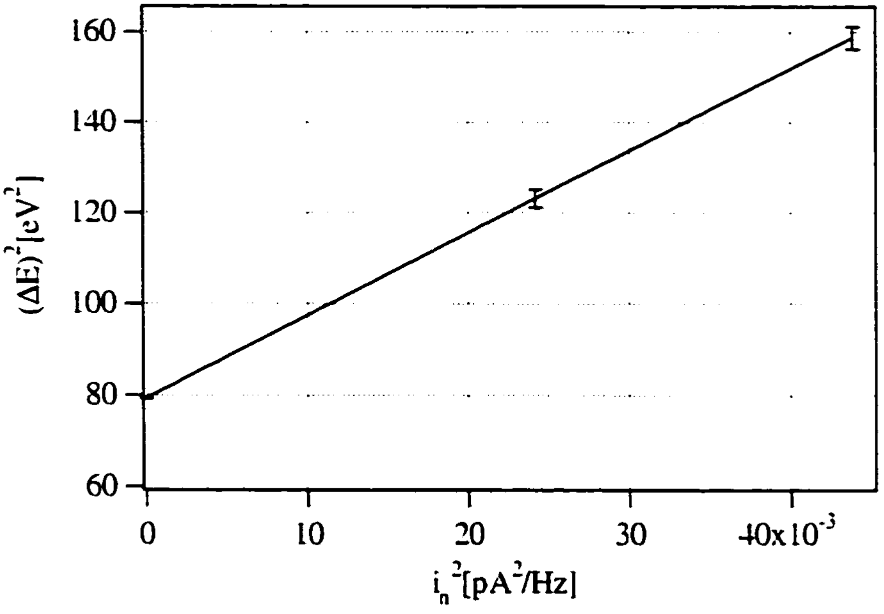

Fig. 4.13 The energy width square as a function of the current noise square of the injection test for device B. The intercept is due to the pick-up noise from the function generator. The test condition is voltage bias V_{bias} = 120 μV and T = 0.21 K. The feedback resistor temperature is at T_R = 1.5 K and T_R = 300 K for the two test points. (device B, 6/6/00)

By scaling down the size of the junction and cooling the feedback resistor, the electronic noises of device B are greatly reduced. Before probing into the details of each electronic noise source of device B, let us give some discussion on how to determine the relationship between the energy width and the total current noise density by doing injection tests. First we measure the electronic current noise. Then the electronic pulses from a HP function generator are injected through a 1MΩ resistor into the input of the electronic circuit with the junction connected. Following the same procedure that is used in the real data acquisition and analysis, we find the energy resolution of the injected pulse. Since the injected pulses are supposed to be identical and noiseless, the injection test provides us the relationship between the energy resolution and the electronic noise.

Two injection tests are done. In one test the feedback resistor is kept at normal room temperature, while in the other one the feedback resistor is cooled down to 1.5 K. The two test results are shown in Fig. 4.13, in which we plot the square of energy width as a function of the square of the current noise. The higher the temperature of the feedback resistor, the bigger the energy width. The ratio of the energy width to the current noise is found to be $k_t = \Delta E / i_n = 42 \pm 4\ \mathrm{eV}/\left(\mathrm{pA}/\sqrt{\mathrm{Hz}}\right)$, which is numerically obtained by taking the square root of the slope of the line in Fig. 4.13.

(1) Johnson noise and shot noise

It is known from Sec. 4.2.1.2 that the Johnson noise of R_f at room temperature is one of the dominant noise sources of the quiescent state and why a 1 MΩ feedback resistor is chosen. The equivalent current noise of the R_f is $\sqrt{4k_B T / R_f} = 130\mathrm{fA}/\sqrt{\mathrm{Hz}}$ at room temperature. In order to reduce this noise to a negligible level in actual measurement, we cool R_f to 1.5 K.

The other electronic noise source at the quiescent state is the shot noise of the junction $\sqrt{2eI}$, where I is the subgap current of the junction at voltage bias point. By scaling down the junction area, the tunneling current can be reduced to minimize the shot noise effect. The area of device B is about 1/3 of device A. The subgap current of device B is 6 ± 1 nA while it is 20 ± 3 nA for device A. So the shot noise of device B, 44 $\mathrm{fA}/\sqrt{\mathrm{Hz}}$ at 0.21K, is only about one half of device A.

Fig. 4.14 shows the electronic current noise spectra of the junction with the feedback resistor at the room temperature and at 1.5 K. In the kHz frequency range, the total current noise with R_f at room temperature is 160 $\mathrm{fA}/\sqrt{\mathrm{Hz}}$, while it is only about 90 $\mathrm{fA}/\sqrt{\mathrm{Hz}}$ when R_f is lowered to 1.5 K. In the low frequency range below 1 kHz, the *1/f* frequency noise has a noticeable presence. When the frequency becomes higher, the noise increases a bit. This may be caused by the nulling DC bias loop or the input capacitance. In the very high frequency region, the noise drops dramatically due to the bandwidth cutoff of the amplifiers. The current noise is about 90 $\mathrm{fA}/\sqrt{\mathrm{Hz}}$ in the frequency range of interest after the feedback resistor is cooled down. It includes the shot noise of 44 fA/$\sqrt{\text{Hz}}$, the nulling loop noise of 65 fA/$\sqrt{\text{Hz}}$, the Johnson noise of 10 fA/$\sqrt{\text{Hz}}$, and the noise of the INA110 amplifier of 10 fA/$\sqrt{\text{Hz}}$. All these noise contributions add up to 80 fA/$\sqrt{\text{Hz}}$. There is still some 40 fA/$\sqrt{\text{Hz}}$ current noise unaccounted for in this analysis. The average total noise with the cold R_f is about 100 fA/$\sqrt{\text{Hz}}$ in the signal band. Thus the energy width due to electronic noise at quiescent state is $\Delta E_{qusnt} = k_I g i_n = 4.2 \pm 0.4$ eV.

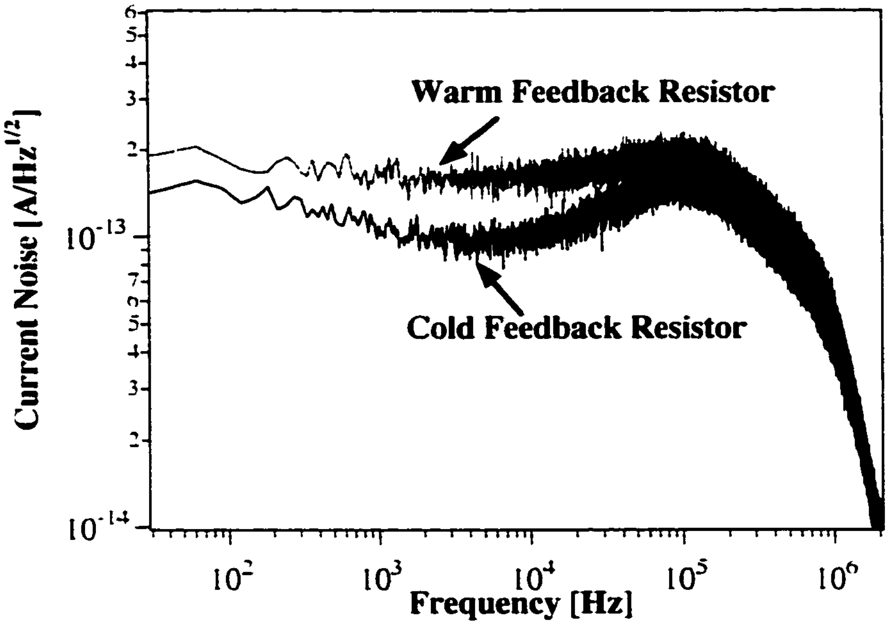

Fig. 4.14 The current noise spectra with feedback resistor at room temperature and cold temperature 1.5 K. (device B, 5/26/00, 6/4/00)

(2) Voltage noise of the amplifier

The equivalent current noise of the voltage noise is e_n / R_d, where e_n is the voltage noise at the input of the amplifier and R_d is the dynamic resistance of the junction at the bias point. At the quiescent state, for device B $R_{d,qusnt} > 50k\Omega$, and $e_n = 0.4$ nV/$\sqrt{\text{Hz}}$. So the equivalent current noise for device B is 10 fA/$\sqrt{\text{Hz}}$, which is very small compared to other noise sources. But when there are x-ray events, the dynamic resistance R_d becomes much smaller because the effective temperature in the quasiparticle system is much higher [Segall, 00a]. The tunneling current increases much more rapidly as a function of bias voltage when there are x-ray events than when there are not.

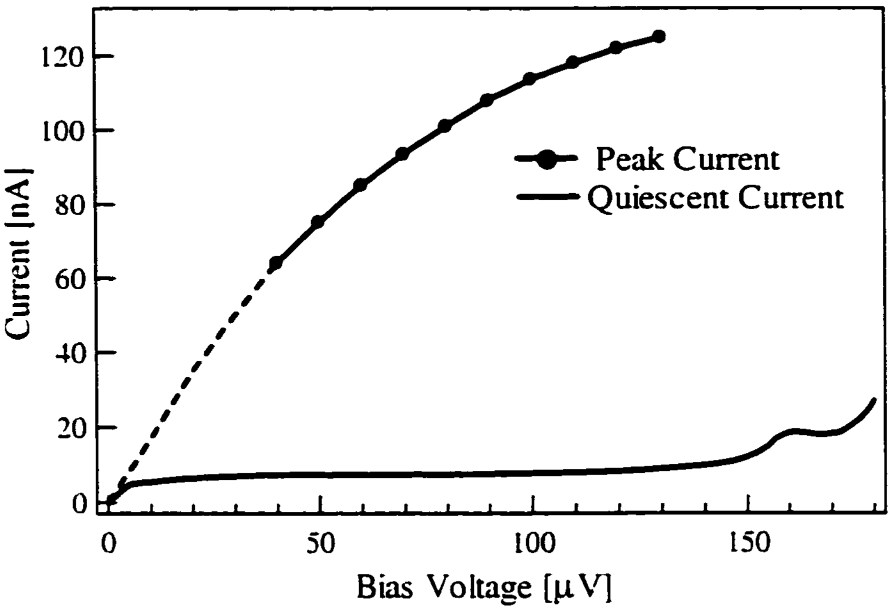

Fig. 4.15 The peak current as a function of bias voltage and the I-V curve at the quiescent state for device B. (device B, 5/11/00)

Fig. 4.15 shows the measured peak current of an x-ray event absorption as a function of the bias voltage and the I-V curve of the junction at the quiescent state. Since the peak current is only instantaneous it gives only small local disturbances to the I-V curve during the x-ray measurement. The dynamic resistance R_d changes with time during the current pulse. It reaches the minimum at the peak current. The slope of dV_{bias}/dI_{peak} gives the lower bound of R_d, which is found to be 3 kΩ at a bias voltage of 120 μV. This dynamic resistance is much smaller than 50 kΩ in the quiescent state.

To measure the effective R_d, a resistor, R_s, is connected in series with the junction as shown in Fig. 4.16. It works as an extra voltage noise source added to the amplifier voltage noise. The total effective voltage noise is then $e_{total}^2 = e_n^2 + e_{n\_series}^2 = e_n^2 + 4kTR_s$. The measured energy resolution ΔE changes as

$$(\Delta E)^2 = (\Delta E_0)^2 + (k_V e_{n\_series})^2 + (k_V e_n)^2 \tag{4.5}$$

where ΔE_0 is the energy width contributed from other noise sources, e_n is the amplifier voltage noise, e_{n_series} is the voltage noise of the series connected resistor R_s and k_V^2 is the relation between the energy width and the voltage noise.

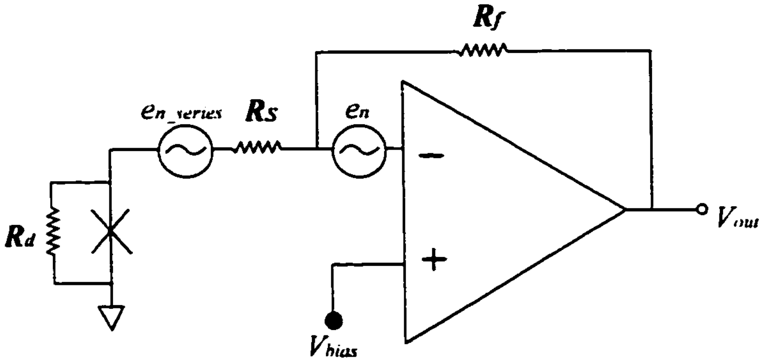

Fig. 4.16 The dynamic resistance R_d measurement circuit when there are signal pulses. R_d is deduced from the relationship between the energy resolution and the Johnson noise of the resistance R_s [Segall, 00].

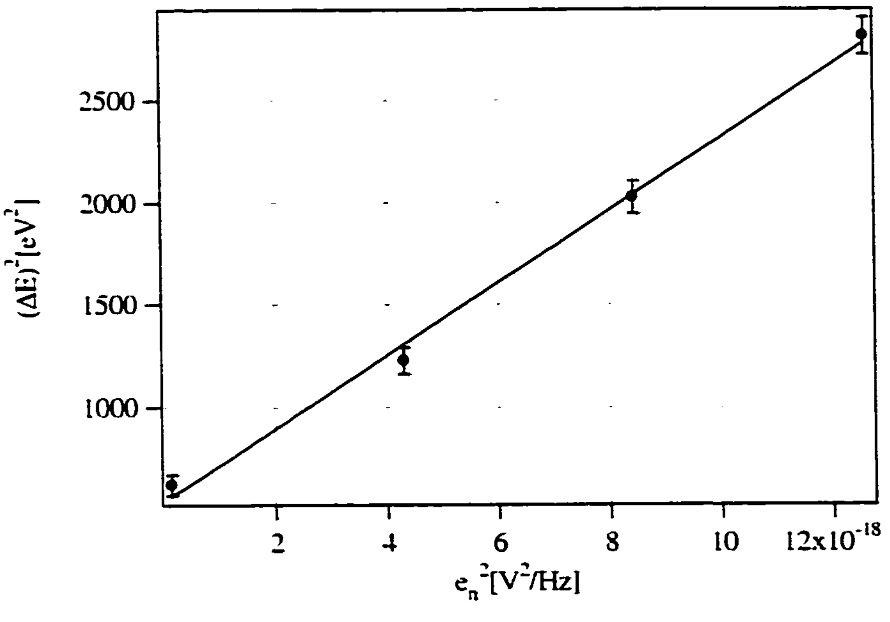

Fig. 4.17 Square of energy resolution ΔE^2 vs. the square of the voltage noise of the series resistor $e^2_{n\_series}$. The device is voltage biased at 120 μV and the temperature is 0.21 K. (device B, 11/18/00)

Fig. 4.17 shows the energy resolution square as a function of the square of the voltage noise of the series resistor, R_s, in the injection test. k_V is calculated from the slope of ΔE^2 vs. $e_{n\_series}^2$ to be $13\pm1\ \mathrm{eV}/\left(\mathrm{nV}/\sqrt{\mathrm{Hz}}\right)$. With the voltage noise e_n being $0.4\,\mathrm{nV}/\sqrt{\mathrm{Hz}}$, the energy width given by the voltage noise is $\Delta E_V = k_V e_n = 5.3\pm1.0$ eV, which is about a factor of 3 smaller than that of device A. The average dynamic resistance R_d is calculated to be $R_d = k_I/k_V = 3.2\pm0.3\ \mathrm{k\Omega}$, in agreement with the value derived from the peak current in Fig. 4.15.

(3) Bias Voltage Fluctuation (ΔV_{bias})

Sec. 4.2.1.1 discussed how incomplete cooling causes the collected charge to vary as a function of the bias voltage. This charge variation adds noise to the measurements. Device B is voltage biased by an active dc feedback loop. The electronic circuit was shown in Fig. 3.4. The *1/f* frequency noise below 1 kHz presented in the dc circuit contributes to the bias fluctuation noise in the low frequency range. Even though this noise is not in the signal band, it cannot be filtered out. It affects the charge response for each individual current pulse.

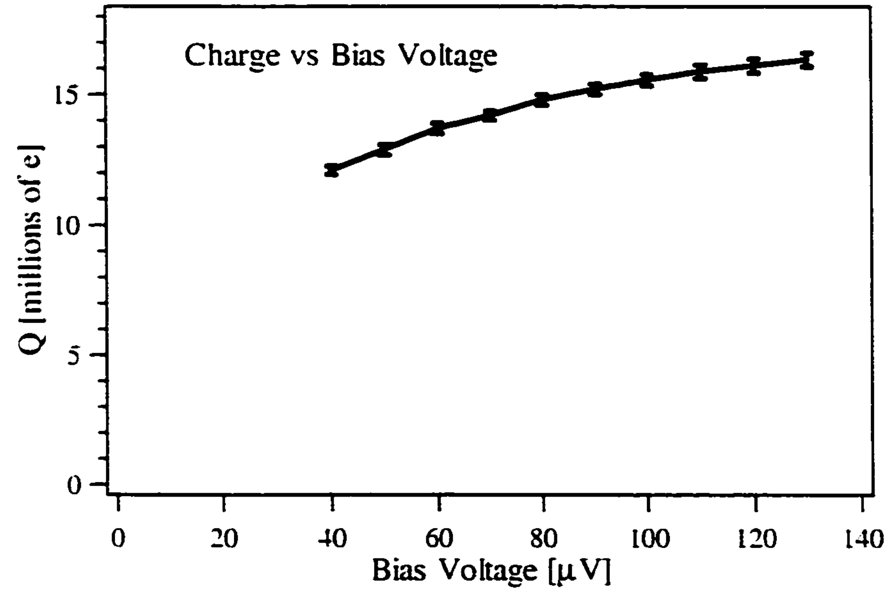

Fig. 4.18 The total charge as a function of the bias voltage for device B. (device B, 5/11/00)

Fig. 4.18 shows the total collected charge as a function of the bias voltage for device B. The energy width induced by the bias voltage fluctuation is

$$\Delta E_{bias} = 2.355\Delta V_{rms}\left(\frac{E}{Q}\,\frac{dQ}{dV}\right). \tag{4.6}$$

where ΔV_{rms} is the RMS bias fluctuation, and the factor 2.355 is to convert RMS to FWHM. For given photon energy E = 5895 eV, with Q and $\frac{dQ}{dV}$ read from Fig. 4.18, $\frac{E}{Q}\frac{dQ}{dV}$ is computed to be 10 eV/μV at V_{bias}=120 μV.

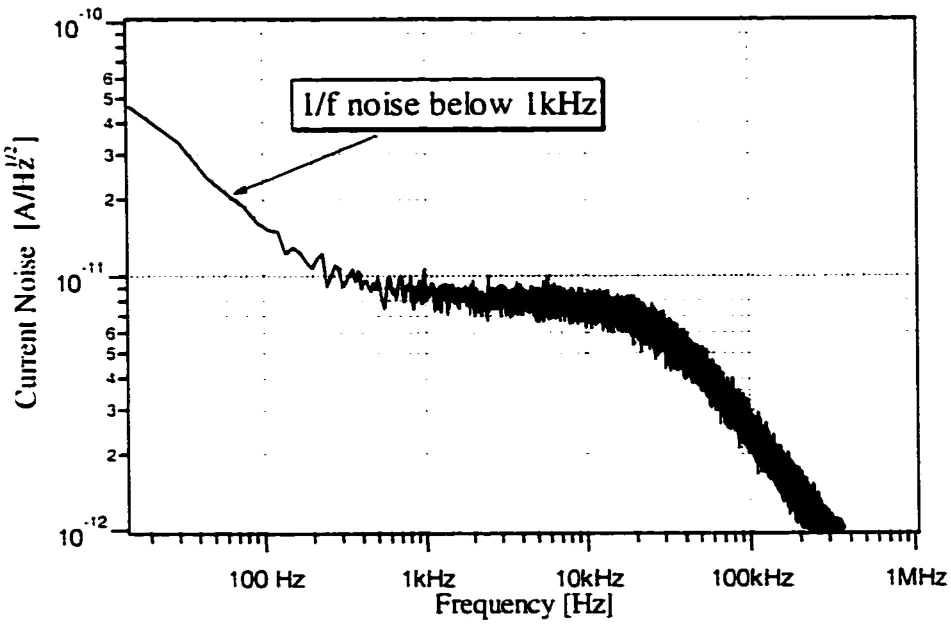

Fig. 4.19 The *1/f* noise of the amplifier. The measurement is done by replacing the junction by a 100Ω resistor.

If the junction is replaced by a warm 100 Ω resistor, the noise spectra of the current amplifier is shown in Fig. 4.19. The *1/f* noise below 1 kHz can be clearly seen and is believed to be caused by the A250 amplifier. Even though the active dc voltage bias provides a stiff load line, it couples the amplifier noise to the bias voltage. In Ref. [Segall, 00] the low frequency bias fluctuation was calculated to be ΔV_{rms}= 0.15 ± 0.02 μV. Thus it leads to an energy broadening of $\Delta E_{bias} = 3.5 \pm 0.5$ eV. By using proper device design to more completely cool the quasiparticles and bias the junction at higher voltage, we can reduce the bias voltage fluctuation noise to be comparable to the device intrinsic noise.

Energy width - ΔE	**device A** **ΔE [eV]**	**device B** **ΔE [eV]**
Predicted Device noise		
Creation	2.9	2.9
Absorber Loss	2.3	~ 0
Trapping Multiplication	3.6	3.6
Backtunneling	5.9	4.8
Cancellation	4.1	2.5
Self-recombination	~ 0	5.0
Sum	**8.9**	**8.9**
Amplifier -related noise		
Current noise	11.8	4.2
Voltage noise	16.8	5.3
Bias-Voltage fluctuations	10.6	3.5
ΔE_{Total} predicted	**24.9**	**12.0**
ΔE_{Total} measured	**25.4±2.1**	**13.1±1.6**

Table 4-3 List of all the noise contributions in devices A and B (FWHM).

In summary, we have quantified three electronic noise sources for device B: the electronic noise without x-ray events, the amplifier voltage noise, and the bias voltage fluctuation noise. Table 4-3 lists all noise sources including the device noise sources for device B and A. The main improvement in device B is the better cooling of quasiparticles in the junctions and the use of cold feedback resistor R_f. All three main electronic noise sources in device A are approximately reduced by a factor of 3. If the finite line width of the x-ray source $\Delta E_{source} = 2.8$ eV is considered, the total energy width of device B is predicted to be $\Delta E_{total}^2 = \Delta E_{device}^2 + \Delta E_{amplifier}^2 + \Delta E_{source}^2 = (12\mathrm{eV})^2$. The experimental results for both device A and B are in agreement with the theoretical prediction [Li, 01]. In device B, the electronic noise sources are no longer the dominant noise source.

Chapter 5 Non-equilibrium Quasiparticle Dynamics in the Ta Absorber

The previous chapter discussed how the optimization of the junction design and the electronic circuit could improve the energy resolution of an STJ detector (device B). The noise sources contributing to the energy resolution of device B were carefully studied and calculated. It was found that the energy resolution on the two sides of the absorbers is better than in the center. This chapter discusses the cause of the location dependence of the energy resolution.

The first part of this chapter discusses how the spatial non-uniformity causes different energy resolution at different locations. A practical solution to eliminate the spatial non-uniformity is presented. In the second part, the non-equilibrium quasiparticle dynamics in the Ta absorber is studied. The diffusion constant and the lifetime of the quasiparticles are derived using a numerical model [Segall, 00]. Both the diffusion constant and the quasiparticle lifetime are the most important parameters in determining the limiting size of the STJ detectors for practical astronomy applications.

5.1 Spatial Uniformity

5.1.1 Spatial Non-uniformity Caused by the Nb Contact

In discussing the major contributing noise sources to the energy broadening of the device B in Chapter 4, most noise sources did not relate to the geometry of the Ta absorber. Apparently though, the energy resolution depends on the location where the x-ray events occur. The location dependence causes big difference in energy resolution in different regions of the absorber. This phenomenon can be attributed to the spatial non-uniformity in the Ta absorber caused by the Nb ground contact in the center of the device.

Based on the analysis in Chapter 4, on the two sides of the Ta absorber the total contribution of all unknown noise sources cannot exceed 5 eV. Thus, the energy broadening in that region caused by spatial non-uniformity should be less than 5 eV. But in the center of the absorber, the energy broadening is much worse, which is about 160 eV for device A and 49 eV for device B as shown in Fig. 5.1. Comparing the energy resolution at different locations, the energy broadening caused by the spatial non-uniformity become dominant in the central region of the absorber.

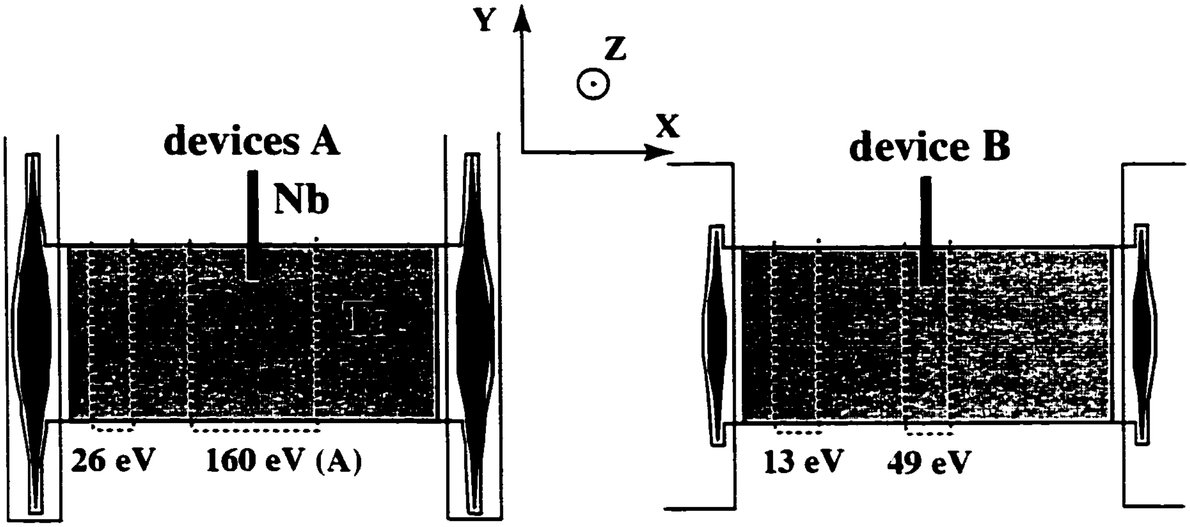

Fig. 5.1 Location dependence of energy resolution for device A (XN93) and B (OP-F99-11C). The broadening of the energy resolution in the center is caused by the Nb ground contact.

Fig. 5.2 shows the total collected charge Q_0 vs. location for device A and device B. The energy resolution becomes worse when the x-ray events are closer to the center. The best energy resolution is achieved on the two sides of the absorber.

In device A and B, a Nb strip is used as the ground contact for the two tunnel junctions. The 2000Å thick Nb contact is sputtered on the Ta film. It covers only the upper side of the absorber in the y direction as shown in Fig. 5.1. The covering dimension is 20 × 5 μm^2. Because the Nb energy gap $\Delta_{Nb} = 1.5$ meV is twice as large as the Ta energy gap, the Nb ground contact can prevent quasiparticles from diffusing out of the Ta absorber at the ground contact.

Nb is known to form a metallic oxide that has a lower energy gap. The Nb oxide forms loss centers for the quasiparticles [Halbritter, 87]. The x-rays absorbed near the Nb ground contact suffer more quasiparticle loss than the x-rays absorbed farther away from the Nb contact in the y direction. This spatial non-uniformity in the y direction degrades the detector performance. As shown in Fig. 5.2 the extra broadening in the center of device A is much larger than that of device B. This difference is believed to be due to fact that the Nb contact of device A was sputtered twice.

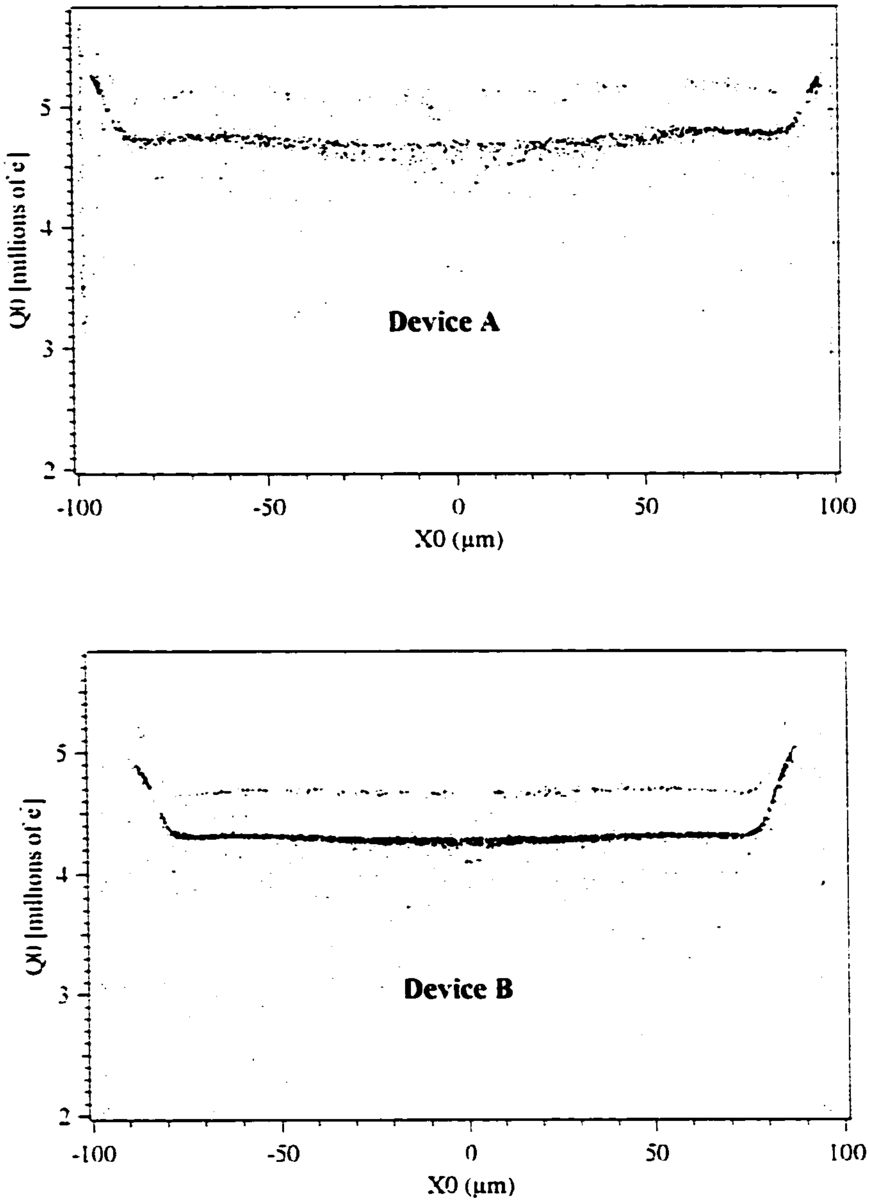

Fig. 5.2 Total charge Q_0 as a function of location for device A and device B. Both devices have a Nb contact in the center. (device A, 2/26/98, [Segall, 00b]; device B, 6/4/00)

The energy histograms of the photon events from the center and one side of device B are shown in Fig. 5.3.

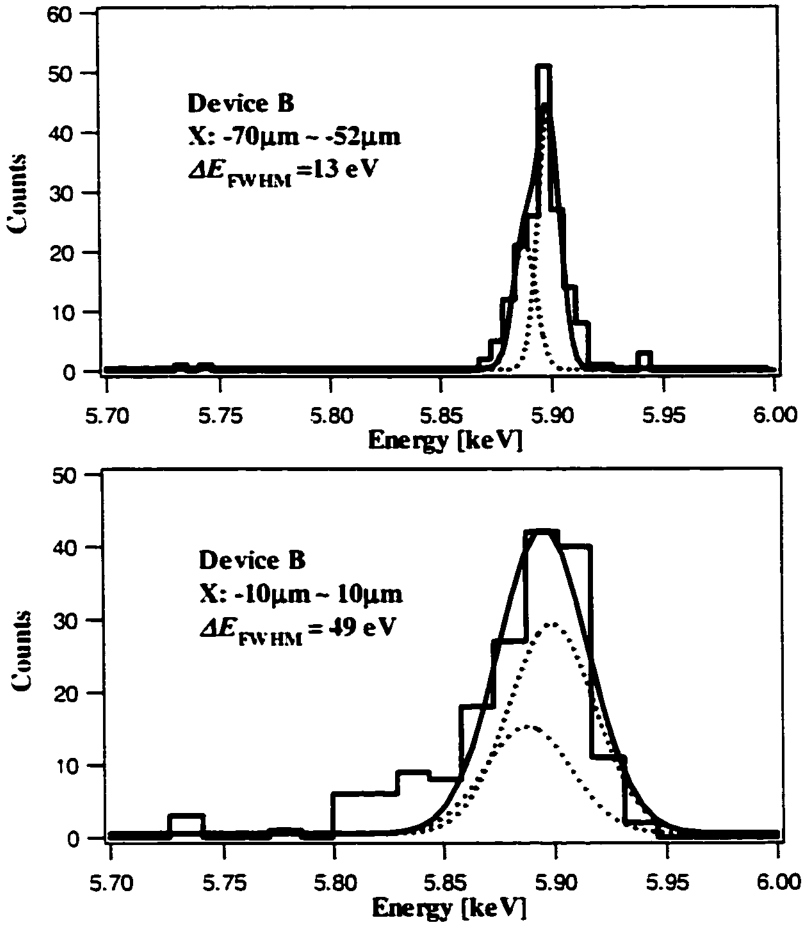

Fig. 5.3 Energy histograms of the photon events from the center (top) and one side of device B (bottom). The energy resolution is 13 eV on the side and 49 eV in the center. Dotted lines show the two lines $K_{\alpha 1}$ and $K_{\alpha 2}$.

5.1.2 Spatial Uniformity with Ta Ground Contact

The spatial non-uniformity causes the energy broadening around the Nb ground contact in the center of the Ta absorber. Using a Ta ground contact connected to the trap of one of the Al junctions can eliminate this problem.

Fig. 5.4 shows the device design to solve the spatial non-uniformity problem. In this design the Nb ground contact in the center of the absorber is replaced by a Ta contact to the trap of the right side junction. Since the energy gap of the Ta is about four times larger than the Al energy gap, once the quasiparticles are trapped in the Al region they cannot diffuse out into the Ta contact. At the working temperature 0.21 K, both the Al trap and the Ta absorber are superconducting. There is no voltage difference among the two Al traps, the Ta absorber and the Ta ground contact. Therefore the Ta contact serves as the ground contact. This configuration prevents any direct contact to the absorber from inducing spatial non-uniformity.

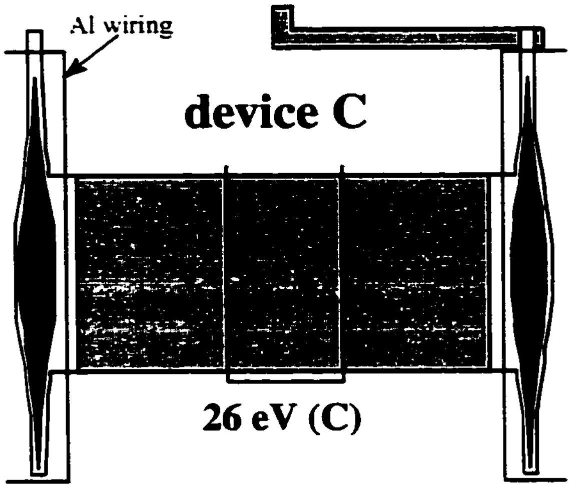

Fig. 5.4 Device C with a Ta ground contact connected to the trap of one of the junctions. This device has the best energy resolution over a large central region of about 50 μm.

The device shown in Fig. 5.4 is our device C. It has the same junction geometry and same absorber as device A. The only difference is that the Nb ground contact is replaced by the Ta ground contact.

The experimental result of the total collected charge as a function of the x-ray event location is shown in Fig. 5.5. The broadening in the center that has been seen for device A indeed disappears. Actually the best energy resolution for this device is in the center of the absorber. In addition, the best energy resolution is pretty uniform in a broad region in the center of the absorber. This strongly indicates that the extra broadening in the center of device A and B is caused by the Nb contact. Over a region of about 50 μm in the center, the energy resolution is uniformly 26 eV shown in Fig. 5.6. This is the best energy resolution that device A achieved in a very small region on one side of the absorber. If the junction geometry of device B is used, the energy resolution in the large central region is expected to be 13 eV.

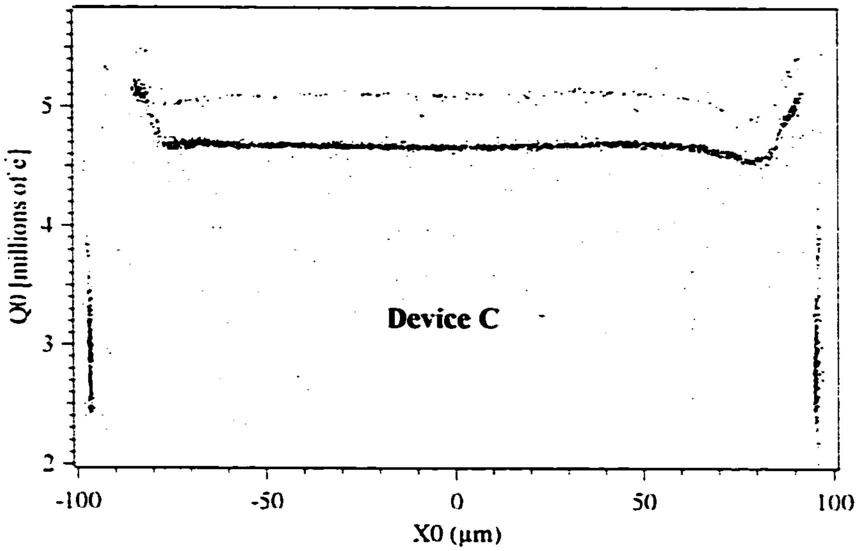

Fig. 5.5 The total collected charge vs. the x-ray event location for device C. (device C, 7/31/00; Filter: Chebysshev, 5th order, 4-90 kHz)

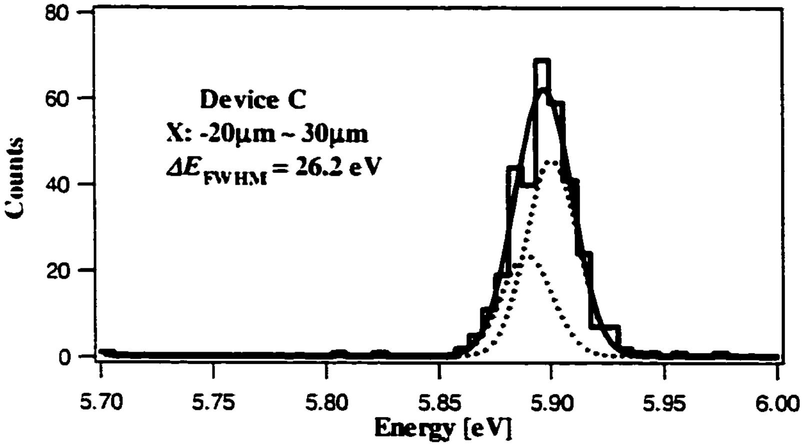

Fig. 5.6 Energy histogram of the photon events from the center of device C. The energy resolution is 26 eV in the center. Dotted lines show the two lines $K_{\alpha 1}$ and $K_{\alpha 2}$.

Fig. 5.5 shows an interesting feature that has not been seen in device A and B. Even though in the central area of the absorber the energy resolution is uniform, it becomes broader near the end of the absorber. There is a noticeable dip on the side of the Ta contact. The dip is believed to be caused by the quasiparticle diffusion into the ground contact. When an x-ray photon lands near the right side, the created quasiparticles can diffuse into the Al trap before they completely scatter down below the Ta gap energy. Even though the Ta ground contact is about 50 μm away from the absorber, some quasiparticles can still leak into the contact lead because the diffusion constant of Al is much larger than that of Ta [Stephan, 97]. Therefore there is some extra quasiparticle loss in the right side junction.

The Ta ground contact might also cause spatial non-uniformity at the edge of the absorber where it makes the contact. This is because the closer the x-ray event is to the Ta ground contact in the *y* direction, the more loss the quasiparticles suffer. In designing such devices, some care has to be taken with this spatial non-uniformity.

5.1.3 Spatial Resolution

The two-junction detectors can achieve 1-D imaging without using numerous readouts. The spatial resolution power of the device is expected to be of the same order of magnitude as the energy resolution – about 0.5%. The spatial resolution $\delta x_0/L$ can be calculated in terms of the measured energy resolution $\delta E/E$ by propagation of errors. It depends both on the absorption location x_0 and the loss parameter α. The expressions for the spectral resolution in a perfect trapping condition is given by [Kraus, 89]

$$\frac{\delta E}{E}=\frac{\delta Q}{Q}\sqrt{2+\sinh^2(\alpha(1/2+x_0/L))+\sinh^2(\alpha(1/2-x_0/L))}\,, \tag{5.1}$$

where L is the absorber length, $\alpha = L\big/\sqrt{D\tau_{loss}}$ is the loss parameter, x_0 is the location of the x-ray event, and of course δQ is the error of the collected charge. From Eq. (5.1) we can calculate the energy resolution δE from the charge uncertainty $\delta Q/Q$ in the presence of absorber loss. Assuming that the charge uncertainties of the two junctions δQ_1 and δQ_2 are equal to δQ, the spatial resolution $\delta x_0/L$ is then

$$\frac{\delta x_0}{L}=\frac{\delta Q}{Q}\sqrt{\left(\frac{\sinh(\alpha(1/2+x_0/L))}{\alpha}\right)^2+\left(\frac{\sinh(\alpha(1/2-x_0/L))}{\alpha}\right)^2}\,. \tag{5.2}$$

Due to the spatial non-uniformity caused by the Nb ground contact, $\delta Q/Q$ varies as a function of the x-ray event location. For device A and B the best spatial resolution is near the two sides of the absorber, while for device C the best spatial resolution is in the central region.

Table 5-1 lists the measured energy resolution and calculated spatial resolution as a function of location for the three devices (A, B, and C). Even though device B has the best energy resolution, due to the spatial non-uniformity caused by the Nb ground contact, its energy resolution is about 50 eV in the center. While for device C the energy resolution is more uniformly around 26 eV in a large central region. The same can be said for the spatial resolution. Device A has worse energy and spatial resolution compared to device B and C across the whole absorber. The best energy resolution of 26 eV for device A, which is in the 60 – 80 μm absorber region, is not shown in the table.

Location [μm]		-70 ~ -50	-50 ~ -30	-30 ~ -10	-10 ~ 10	10 ~ 30	30 ~ 50	50 ~ 70
Device A	δE [eV]	59	70	90	95	93	88	48
	δx [μm]	0.95	1.1	1.3	1.3	1.3	1.3	0.78
Device B	δE [eV]	13	29	45	49	37	29	22
	δx [μm]	0.24	0.51	0.75	0.79	0.61	0.51	0.42
Device C	δE [eV]	37	26	24	23	29	38	-
	δx [μm]	0.70	0.46	0.39	0.37	0.48	0.67	-

Table 5-1 The energy and spatial resolution as a function of locations for the three devices. The photon energy is 5895 eV, and the length of the absorber is 200 μm. The loss parameter α is 1.6 for device A [Segall, 00], 0.75 for device B and C (section 5.3).

One thing missing here is the direct measurement of the spatial resolution due to the difficulty in confining the x-ray photons to small areas. If masks are to be used to do such a measurement, first they must be thick enough to stop the x-rays. They must also be precisely aligned with the device to achieve good spatial resolution. The distance between the mask and the device has to be very small since the x-ray source is not a point source.

In summary, we studied the spatial uniformity and resolution of Ta based detectors. It was found that the Nb ground contact causes extra energy broadening and spatial non-uniformity in the central region of the absorber for devices A and B. By using a Ta ground contact instead of a Nb ground contact, better spatial uniformity can be achieved. Device B has the best energy resolution on one side of the absorber, but device C has good energy resolution in a broad central region of the absorber. Especially in the center, the energy resolution of device C is about two times better than device B. The best energy resolution in device B is achieved because the better quasiparticle cooling in the device design, while the improved performance of device C is mainly due to the replacement of the Nb contact by the Ta contact.

In the future one easy improvement is to combine small junctions with the Ta ground contact design. It is expected such a device will achieve 13 eV energy resolution in a large central region of the absorber. Another consideration is to move the Ta ground contact farther away from the Ta absorber to prevent quasiparticles from diffusing into it.

5.2 Device Modeling

Quantitatively analyzing the detectors involves studying both the quasiparticle diffusion process in the Ta absorber and the quasiparticle tunneling process in the Al junctions. Considering all the possible processes inside the device, the only way currently available is to numerically simulate them [Segall, 00]. Due to the different dynamics in the Ta absorber and the Al junction, two kinds of simulations are used to study our devices.

5.2.1 Quasiparticle Diffusion in the Ta Absorber

The created quasiparticles propagate through the Ta absorber by the process of diffusion. Theoretically, to fully simulate the whole process, both the energy distribution and the spatial density distribution of the quasiparticles must be considered. Since quasiparticle relaxations in the Ta absorber are much faster than the diffusion process, it is appropriate to ignore quasiparticle relaxations. Thus only the spatial distribution of the quasiparticle density $u(x, t)$ need to be simulated. In the 1-D imaging detector, the quasiparticle density function in the Ta absorber can be described by the one-dimensional diffusion equation,

$$\frac{\partial u(x,t)}{\partial t} - D\frac{\partial^2 u(x,t)}{\partial x^2} = -\frac{u(x,t)}{\tau_{loss}} \tag{5.3}$$

with the following boundary and initial condition,

$$u(x,t=0) = N_0\delta(x - x_0) \text{ and } \left.\frac{\partial u}{\partial x}\right|_{x=\pm L/2} = \frac{u|_{x=\pm L/2}}{L_{trap}}, \tag{5.4}$$

where D is the diffusion constant, τ_{loss} is the quasiparticle lifetime, N_0 is the number of initially created quasiparticles, and x_0 is the photon absorption location. $L_{trap} = \sqrt{\frac{D^2\tau_{trap}}{D_{Al}}}$ is the characteristic trapping length [Segall, 00b]. The charge $Q_{1(2)}$ that is trapped in the Al traps of the two junctions can be solved analytically [Jochum, 93]

$$Q_{1(2)}(x_0) = Q_0\frac{\sinh(\alpha(1/2 \pm x_0/L)) + \beta\cosh(\alpha(1/2 \pm x_0/L))}{(1+\beta^2)\sinh(\alpha) + 2\beta\cosh(\alpha)}, \tag{5.5}$$

where $Q_0 = eN_0$ is the total charge initially created by an x-ray photon. $\beta = \sqrt{\tau_{trap}/\tau_{loss}}$ is a measure of the relative time scales of trapping and loss, and $\alpha = L/\sqrt{D\tau_{loss}}$ is the loss parameter.

In order to study the dynamics of quasiparticles, the quasiparticle density as a function of time is required to simulate the tunneling current. The Crank-Nicholson formalism [Press, 92] is used to numerically solve the diffusion equation (5.3) because it is unconditionally stable for an arbitrary time step dt and is accurate to the second order in both space and time. Using the shorthand notation $u_j^n \equiv u(x_j, t^n)$, the Crank-Nicholson difference equation is

$$\frac{u_j^{n+1} - u_j^n}{\Delta t} = \frac{D}{2}\left[\frac{(u_{j+1}^{n+1} - 2u_j^{n+1} + u_{j-1}^{n+1}) + (u_{j+1}^n - 2u_j^n + u_{j-1}^n)}{(\Delta x)^2}\right]. \tag{5.6}$$

Eq. (5.6) can be written in the following matrix form,

$$\begin{pmatrix} 1+\delta & -\delta/2 & & & \\ -\delta/2 & 1+\delta & -\delta/2 & & \\ & -\delta/2 & 1+\delta & -\delta/2 & \\ & & & & \cdots\cdots \end{pmatrix} \begin{pmatrix} u_0^{n+1} \\ u_1^{n+1} \\ u_2^{n+1} \\ \cdots\cdots \end{pmatrix} = \begin{pmatrix} 1-\delta & \delta/2 & & & \\ \delta/2 & 1-\delta & \delta/2 & & \\ & \delta/2 & 1-\delta & \delta/2 & \\ & & & & \cdots\cdots \end{pmatrix} \begin{pmatrix} u_0^{n} \\ u_1^{n} \\ u_2^{n} \\ \cdots\cdots \end{pmatrix}. \tag{5.7}$$

where $\delta \equiv \frac{D\Delta t}{(\Delta x)^2}$. Quasiparticle loss can be included by adding $\frac{\Delta t}{2\tau_{loss}}$ to the diagonal elements of the left hand side matrix and subtracting $\frac{\Delta t}{2\tau_{loss}}$ from the diagonal elements of right hand side matrix. The loss terms can also be added to each individual diagonal element to simulate local losses such as the Nb loss.

The initial quasiparticle density $u(x, x_0, t=0)$ is assumed to be a Gaussian distribution in space with a width of 5 μm. In the simulation the initial total charge eN_0 and the diffusion constant D are adjustable numbers. The center of the initial quasiparticle density is at x_0 where the x-ray photon is absorbed.

The boundary condition $\left.\frac{\partial u}{\partial x}\right|_{x=\pm L/2} = \frac{u}{L_{trap}}$ can be written as

$$\frac{u(x_1)-u(x_0)}{\Delta x} = \frac{u(x_0)}{L_{trap}} = \frac{u(x_0)}{\sqrt{D^2\tau_{trap}/D_{Al}}}. \tag{5.8}$$

The number of quasiparticles flowing from the Ta absorber into the Al trap is going to be used in the simulations of the Al junction.

5.2.2 Quasiparticle Tunneling in the Al Junction

To simulate all the physical processes in the junctions as discussed in Chapter 2 is very complicated. To simplify the process, a spatially uniform distribution of the quasiparticle density in the Al trap is assumed. This is justifiable since quasiparticles diffuse very rapidly in the Al trap. Thus, only the quasiparticle energy distribution needs to be simulated.

Both electrode and counter-electrode are first divided into many energy bins to trace the quasiparticle energy distribution. For the quasiparticle in each energy bin there are five possible processes: (1) the injection process which records the number of quasiparticles flowing from the Ta absorber into the Al trap at the Ta gap energy $E = \Delta_{Ta}$,

(2) the scattering process which includes the quasiparticles scattered from higher energy levels minus the quasiparticles scattering down to lower energy levels, (3) the tunneling processes which include all four possible tunneling processes, (4) the self-recombination process which causes quasiparticle loss in the Al junction, and (5) the outdiffusion process in the counter-electrode, which simulates the quasiparticle loss from the junction region by outdiffusion. Adding all the processes together,

$$\frac{dN[E_i]}{dt} = \left.\frac{\partial N[E_i]}{\partial t}\right|_{int} + \left.\frac{\partial N[E_i]}{\partial t}\right|_{scat} + \left.\frac{\partial N[E_i]}{\partial t}\right|_{tun} + \left.\frac{\partial N[E_i]}{\partial t}\right|_{recom} + \left.\frac{\partial N[E_i]}{\partial t}\right|_{out} . \tag{5.9}$$

The first term is the quasiparticle flow from the absorber to the trap, which is calculated from the simulation of quasiparticle diffusion in the Ta absorber as mentioned earlier,

$$\left.\frac{\partial N_{trap}[E_{\Delta Ta}]}{\partial t}\right|_{int} = \frac{I_{int}}{e} . \tag{5.10}$$

where I_{int} is the quasiparticle current flowing from the Ta absorber into the Al trap.

The second term is due to the inelastic scattering and can be written out as

$$\left.\frac{\partial N[E_i]}{\partial t}\right|_{scat} = \sum_{j=i+1}^{M} \frac{N[E_j]}{\tau_s[E_j,E_i]} - \sum_{k=0}^{i-1} \frac{N[E_i]}{\tau_s[E_i,E_k]} . \tag{5.11}$$

In Eq. (5.11) the first term on the right hand side is the number of quasiparticles scattered from higher energy levels into E_i and the second term is the number of quasiparticles scattered out from E_i to lower energy levels.

The third term of Eq. (5.9) is the change of quasiparticle number in the trap due to quasiparticle tunneling

$$\left.\frac{\partial N_{trap}[E_i]}{\partial t}\right|_{tun} = -\frac{N_{trap}[E_i]}{\tau_{tun,trap}^{E_i+eV}} - \frac{N_{trap}[E_i]}{\tau_{tun,trap}^{E_i-eV}} + \frac{N_{ce}[E_i+eV]}{\tau_{tun,ce}^{E_i}} + \frac{N_{ce}[E_i-eV]}{\tau_{tun,ce}^{E_i}} . \tag{5.12}$$

In the trap, the forward tunneling process (process A) and the reverse backtunneling process (process C) from E_i decrease the number of the quasiparticles. And the reverse tunneling (process B) and the backtunneling process (process D) increase the number of quasiparticles. The quasiparticle tunneling from the counter-electrode can be computed similarly.

The fourth term in Eq. (5.9) is the quasiparticle recombination loss.

$$\left.\frac{\partial N[E_i]}{\partial t}\right|_{rec} = -\frac{R}{V}\left[\left(\sum_{j=1}^{M} N\left[E_j\right]\right) + 2n_{th}V\right]N[E_i], \tag{5.13}$$

where the first term is due to self-recombination, and the second term is caused by thermal recombination.

The last term in Eq. (5.9) is the quasiparticle loss due to the out-diffusion process in the counter-electrode. We simply assume a loss rate of $1/\tau_{out}$.

$$\left.\frac{\partial N_{ce}[E_i]}{\partial t}\right|_{out} = -\frac{N_{ce}[E_i]}{\tau_{out}}. \tag{5.14}$$

The final tunneling current including all four processes and summing up all the energy levels yields

$$\frac{I_{tun}}{e} = \sum_i \left[\frac{N_{trap}[E_i]}{\tau_{tun,trap}^{E_i+eV}} - \frac{N_{trap}[E_i]}{\tau_{tun,trap}^{E_i-eV}} + \frac{N_{ce}[E_i+eV]}{\tau_{tun,ce}^{E_i}} - \frac{N_{ce}[E_i-eV]}{\tau_{tun,ce}^{E_i}}\right] \tag{5.15}$$

By fitting the experimental pulses to this model, parameters such as D, Q_0, τ_{loss}, τ_{trap}, and τ_{out} can be determined, see Section 5.3.2. The information on these physical parameters provides ways to investigate the non-equilibrium quasiparticle dynamics in the superconducting tunnel junction detectors.

5.3 Experimental Results

Three devices (E, F, G) with the different absorber lengths shown in Fig. 5.7 were used to study the quasiparticle dynamics. The absorber sizes of the three devices are 200 × 100 μm^2, 500 × 100 μm^2, and 1000 × 100 μm^2 respectively. Some physical parameters of the three devices are listed in Table 5-2. They each have the same diamond shaped junction size of 64 × 64 μm^2. Each junction is voltage biased at 130 μV and operated at 0.21 K.

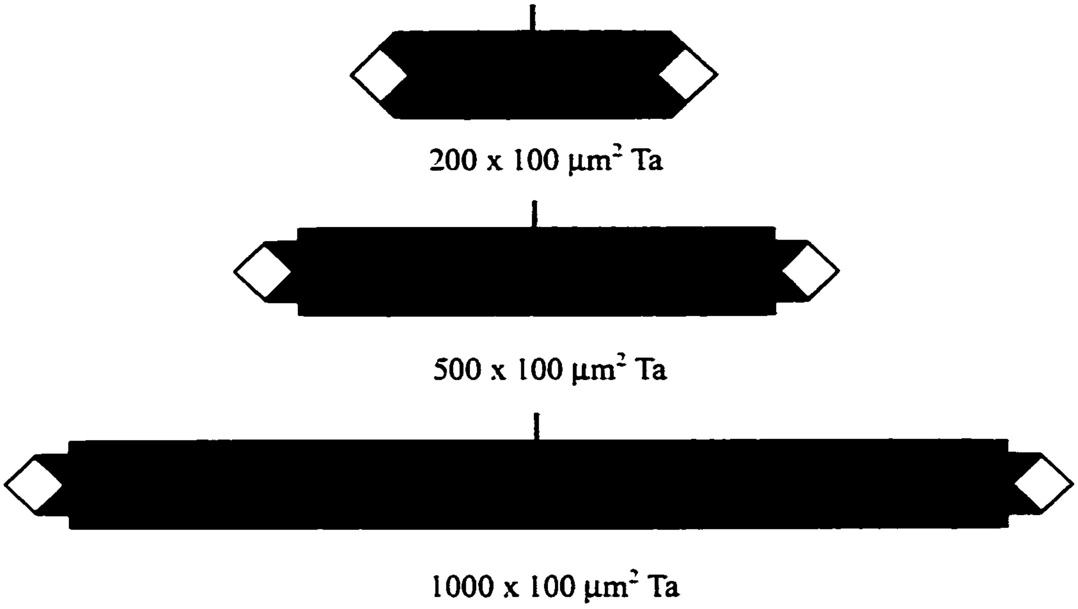

Fig. 5.7 Three devices (E, F, G) with different absorber length 200, 500, 1000 μm respectively. All of them have the same shape and sized junctions, except that device E has a large trap.

	Device E	Device F	Device G
Absorber Length [μm]	200	500	1000
Jc [A/cm^2]	30	30	30
Trap Volume [μm^3]	1944	972	972
$\tau_{tun,\,tr}$ [μs]	6.8	3.4	3.4
$\tau_{tun,\,ce}$ [μs]	24	24	24

Table 5-2 Physical parameters of the three devices with different absorber length.

5.3.1 Charge Fitting

The Q_1 vs. Q_2 plots of the three devices are shown in Fig. 5.. Each dot represents a single x-ray event. They form the K_α and K_β lines on the plot. The up-bending at the two ends of the K_α line of the 200 μm long device is due to the 10 μm overlap between the Ta absorber and the Al trap. Because of the superconductor proximity effect, the 2000Å thick Al on the 6000 Å thick Ta film becomes proximitized in the overlap region. The coherence length of Al ($\xi_{\mathrm{Al}} \sim 5600\,\text{Å}$) is much longer than that of pure Ta ($\xi_{\mathrm{Ta}} \sim 450\,\text{Å}$). Using the de Gennes model [de Gennes, 64], the energy gap of the proximitized Al can be estimated to be around 400 μeV, which is significantly higher than the gap energy of pure Al but is still smaller than the gap energy of Ta.

If the x-ray photon is absorbed in the overlap region, because the Al has a lower energy gap than the Ta, more quasiparticles can be created in the overlap region than if the photon were absorbed in the pure Ta absorber. As the portion of the 'hot' spot, i.e., more quasiparticles, formed by the x-ray absorption in the overlap region increases, the number of the created quasiparticles increases. We see continuous increase of the charges at the two ends of the absorber. The total charge at the two ends of the absorber is more than 20% higher than in the center for the 200 μm long device.

Assuming the energy is uniformly distributed in space, the net increase of quasiparticles can be estimated from

$$\frac{\Delta N}{N_0} = \frac{N_0 \times \dfrac{\Delta_{Ta} - \Delta_{Al}}{\Delta_{Al}} \times \dfrac{d_{Al}}{d_{Ta} + d_{Al}}}{N_0} = 19\% \qquad (5.16)$$

where N_0 is the total number of quasiparticles generated, d_{Al} and d_{Ta} are the thickness of Al and Ta films, respectively. The estimated charge increase is in agreement with the observation.

In Fig. 5., the Q_1 vs. Q_2 data of the device with a 200 μm long absorber follows almost a straight line. This indicates that there is very little quasiparticle loss in the Ta absorber. But the other two devices show apparent quasiparticle loss in the center region. If there exists a uniform quasiparticle loss in the absorber, the quasiparticles generated in the center will suffer more loss than the quasiparticles generated near the traps. This is because it takes longer for quasiparticles to diffuse out to the Al trap from the center than from the edge. Since 200 μm is relatively short, there is almost no quasiparticle loss in this device.

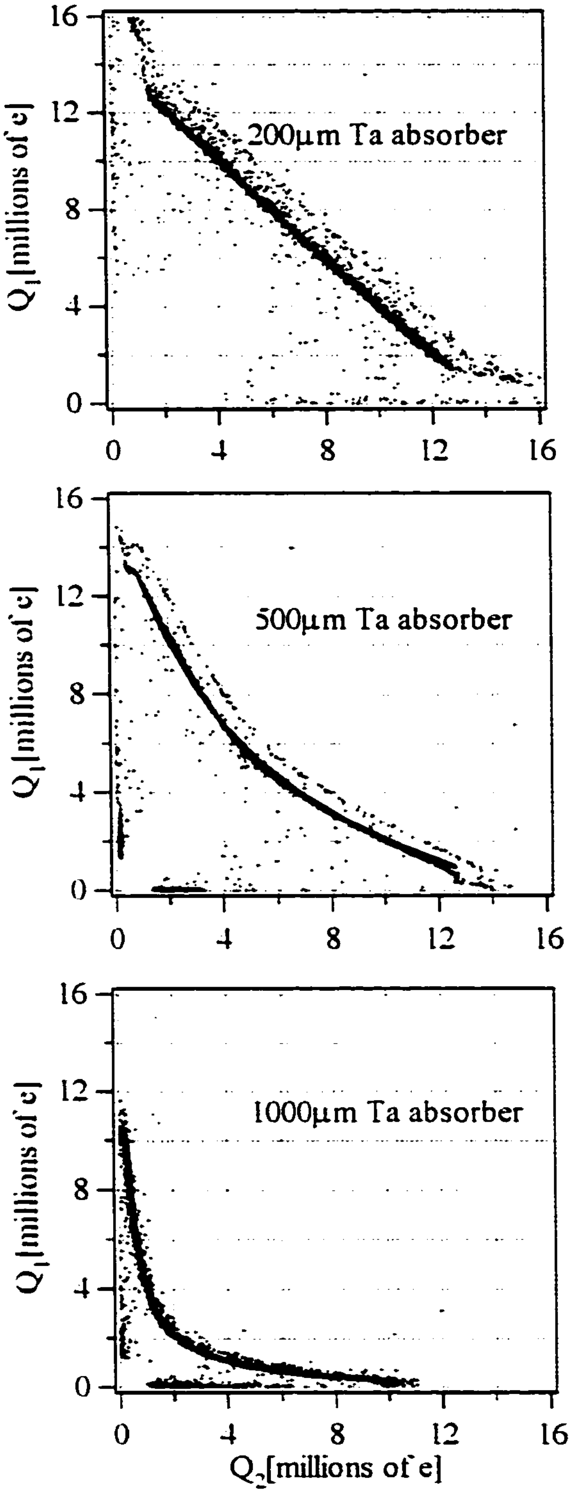

Fig. 5.8 Q_1 vs. Q_2 for three devices (E, F, G) with different lengths. The dots are experimental x-ray events and the solid lines are the fitting curves. (device E, 1/22/01; device F, 3/6/01; device G, 3/19/01)

In the theoretical model of Eq. (5.13), the self-recombination effect in the Al junction was included. The recombination rate ***R*** of the Al used in the simulation is derived from the charge fluctuation measurement of a confined potential box [Wilson, 01]. Self-recombination affects the shape of the Q_1 vs. Q_2 plot. If the x-ray events are near the edge of the absorber, most of the quasiparticles generated will diffuse into the nearest junction. The more the excess quasiparticle density created near the edge of the absorber, the larger the self-recombination loss of the quasiparticles in the Al trap. The self-recombination process causes about 1.7% of quasiparticle loss when they are generated in the center and about 3.4% near the edge for the 200 μm long device. Therefore the self-recombination has the opposite effect on the shape of the Q_1 vs. Q_2 compared to what uniform quasiparticle loss does. But compared to the uniform loss, the self-recombination loss is small. It is hardly observed in Fig. 5..

Fig. 5. shows that the longer the absorber, the more loss the quasiparticles suffer. About 30% of the quasiparticles generated in the center of the 500 μm long device are lost, while in the 1000 μm long device about 75% are lost. The spatial non-uniformity along the x-direction has been observed for devices with a Nb ground contact in the center of the Ta absorber. But how much does a Nb ground contact cause the quasiparticle loss in the center? To answer this question, we can add in the 1-D model of the Nb point loss.

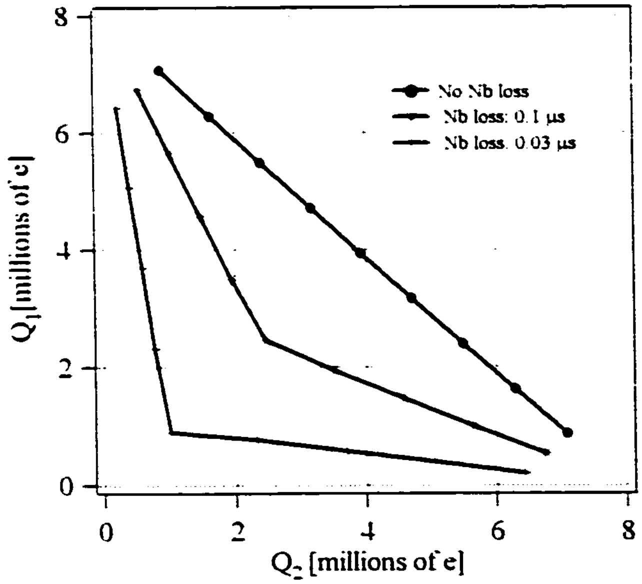

Fig. 5.9 (a).Q_1 vs. Q_2 with only Nb loss in a Ta absorber.

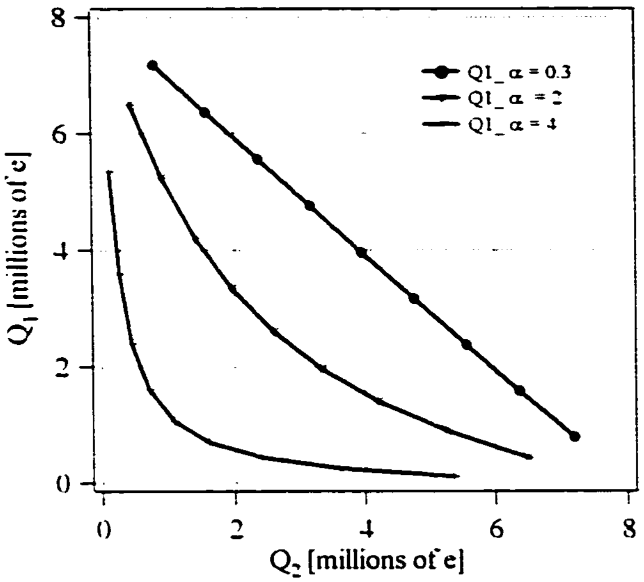

Fig. 5.9 (b) Q_1 vs. Q_2 with only uniform loss in a Ta absorber.

Fig. 5.9 (a) and (b) show the different behaviors of the Q_1 vs. Q_2 caused by the Nb point loss in the center and by the uniform loss in the Ta absorber. If there is only the Nb contact loss, the Q_1 vs. Q_2 plot shows a cusp-like structure in the center, and a straight line from the center to the ends (see Fig. 5.9 (a)). If only the uniform loss exists, the Q_1 vs. Q_2 is a smooth curve (Fig. 5.9 (b)). These two loss mechanisms show distinct features in the Q_1 vs. Q_2 plots.

The experimental Q_1 vs. Q_2 plots of the three different devices are more similar to the ones with only uniform quasiparticle loss in the absorber. This suggests that the quasiparticle loss is mainly due to uniform loss, but the Nb loss causes energy broadening.

Absorber Length [μm]	200	500	1000
Loss Parameters $\alpha = L/\sqrt{D\tau_{loss}}$	0.75	1.9	4.0
Quasiparticle lifetime in the Nb contact region [μs]	20	20	20

Table 5-3 The loss parameter α and the quasiparticle lifetime in the Nb ground contact region.

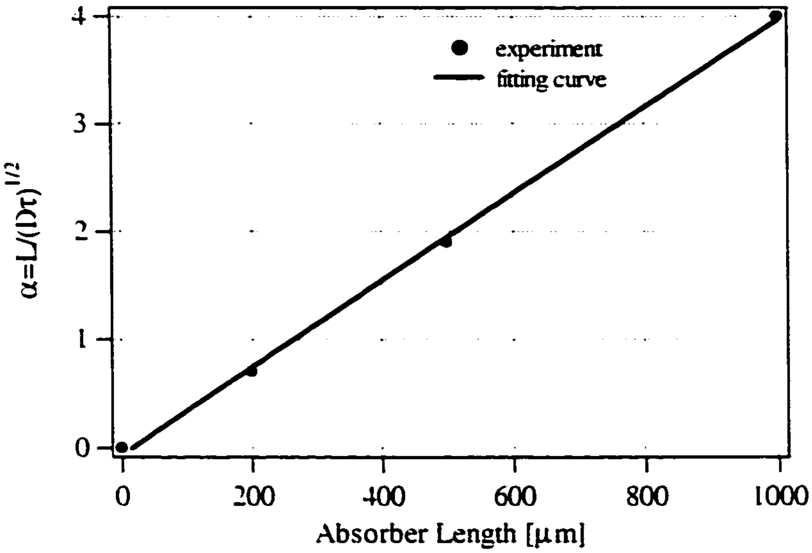

Fig. 5.10 The loss parameter α as a function of the absorber length L.

The quasiparticles uniform loss can be described by the loss parameter α, which is proportional to the length of the absorber

$$\alpha = L/\sqrt{D\tau_{loss}}\,. \tag{5.17}$$

Table 5-3 lists the values of α obtained through fitting Q_1 vs. Q_2 for the three devices. If the Ta absorber films in the three devices have the same quality, then the lifetime and the diffusion constant of the quasiparticles in these three devices will be the same. Thus the loss parameter α should be a linear function of the absorber length. Fig. 5.10 shows the linear relationship between α and the absorber length.

We now try to include the Nb contact loss in the simulation. But first, two assumptions have to be made. The first assumption is that the quasiparticle lifetime in the Ta film is the same for all three devices. The second assumption is that the quasiparticles lifetime in the Nb contact region is also the same for all three devices. We use an iterative procedure to find the Nb contact loss. We begin with the 200 μm long device and assume all the loss is caused by the Nb contact. Then we substitute this loss into the 500 and 1000 μm long devices. The residual loss can be contributed to the Ta uniform loss. We then substitute the Ta uniform loss back into the 200 μm long device and recalculate the Nb contact loss. The Nb contact loss is then put back into the 500 and 1000 μm long devices for next step calculation. After many iterations we get both the Ta uniform loss parameters and the Nb contact loss parameter from these three devices.

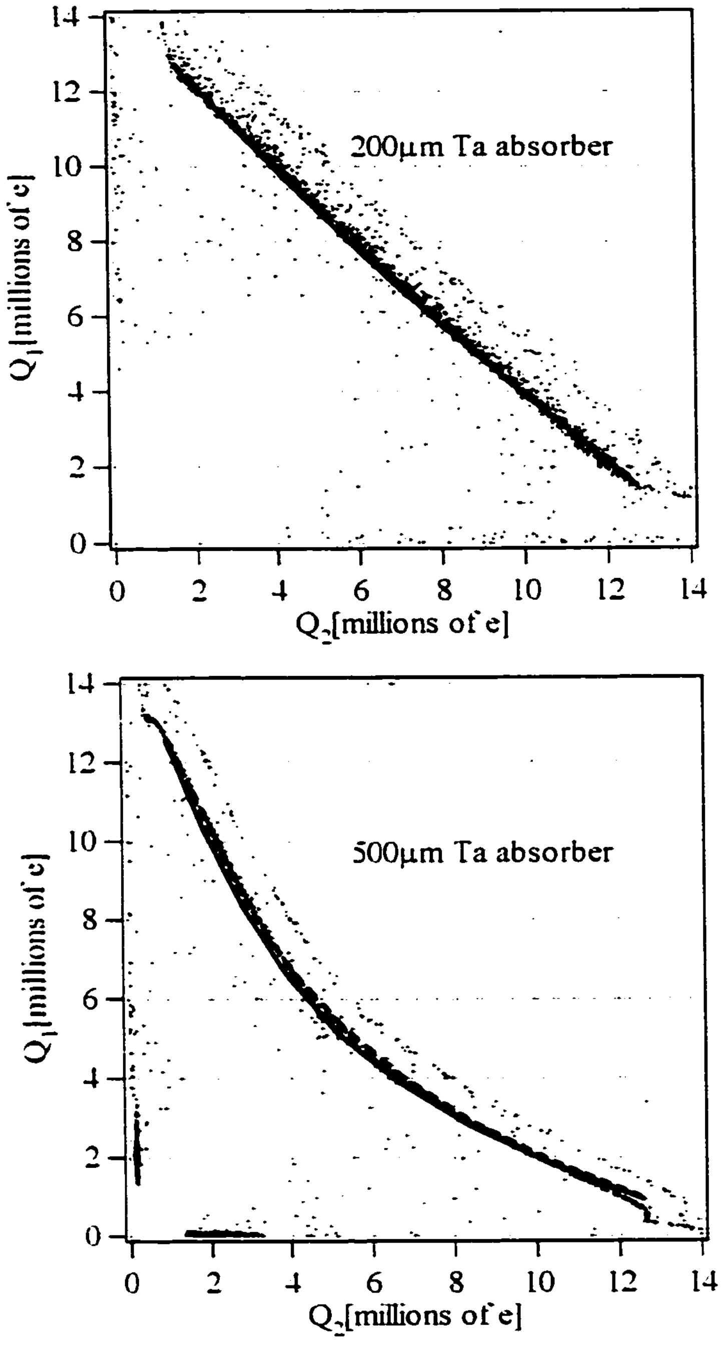

Fig. 5.11 Q_1 vs. Q_2 of two devices (E and F) with different lengths. The dots are experimental data points. The solid lines are the model with Nb contact loss. the dashed lines are the model without Nb contact loss. (device E. 1/22/01; device F. 3/6/01)

Fig. 5. shows the fitting to the experimental Q_1 vs. Q_2 data (the dots). The solid lines are the model including the Nb contact loss, while the dashed line is just the uniform quasiparticle loss model. Based on the fitting, the most quasiparticle loss comes from the uniform loss in the Ta absorber, while the loss due to the Nb contact is relatively small. Though it is small, the Nb loss contributes to the energy broadening in the center of the absorber.

The loss parameter α gives information about the product of the quasiparticles lifetime τ_{loss} and the diffusion constant D. It can be used to derive the quasiparticle lifetime once the diffusion constant D is known from the experimental data.

The amplitude and duration of the current pulses change with the absorber length. The longer the absorber, the longer the time that the quasiparticles take to reach the Al trap. Since the total charge generated by the x-ray photon is fixed, the long diffusion time causes the reduction in the amplitude of the current pulse. Fig. 5.12 shows the current pulses created by x-ray events at different locations on the three devices. The left panels show the current pulses created near one edge of the absorber for the three devices. The current asymmetry in the two junctions is clearly seen here since the x-ray event is closer to one junction. The right panels show the current pulse created by x-ray events that occurred in the center of the absorber. The current pulses on the two junctions of the device are identical as they should be.

In the 200 μm long device, the quasiparticle diffusion time in the Ta absorber is much shorter than both the tunneling time in the Al junction and the outdiffusion time in the counter-electrode. The pulse duration is determined mainly by the tunneling time and the outdiffusion time. But when the absorber becomes longer, the diffusion time increases as the square of the absorber length. If the diffusion time becomes longer than the tunneling time and the outdiffusion time, the pulse duration will be determined by the diffusion time. Long pulse duration affects the count rate, because the average time interval between two pulses should be ten times the pulse duration to avoid overlap. From Fig. 5.12 we estimate the count rate to be about 200 Hz for the 1000 μm long device and 1 kHz for the 200 μm long device.

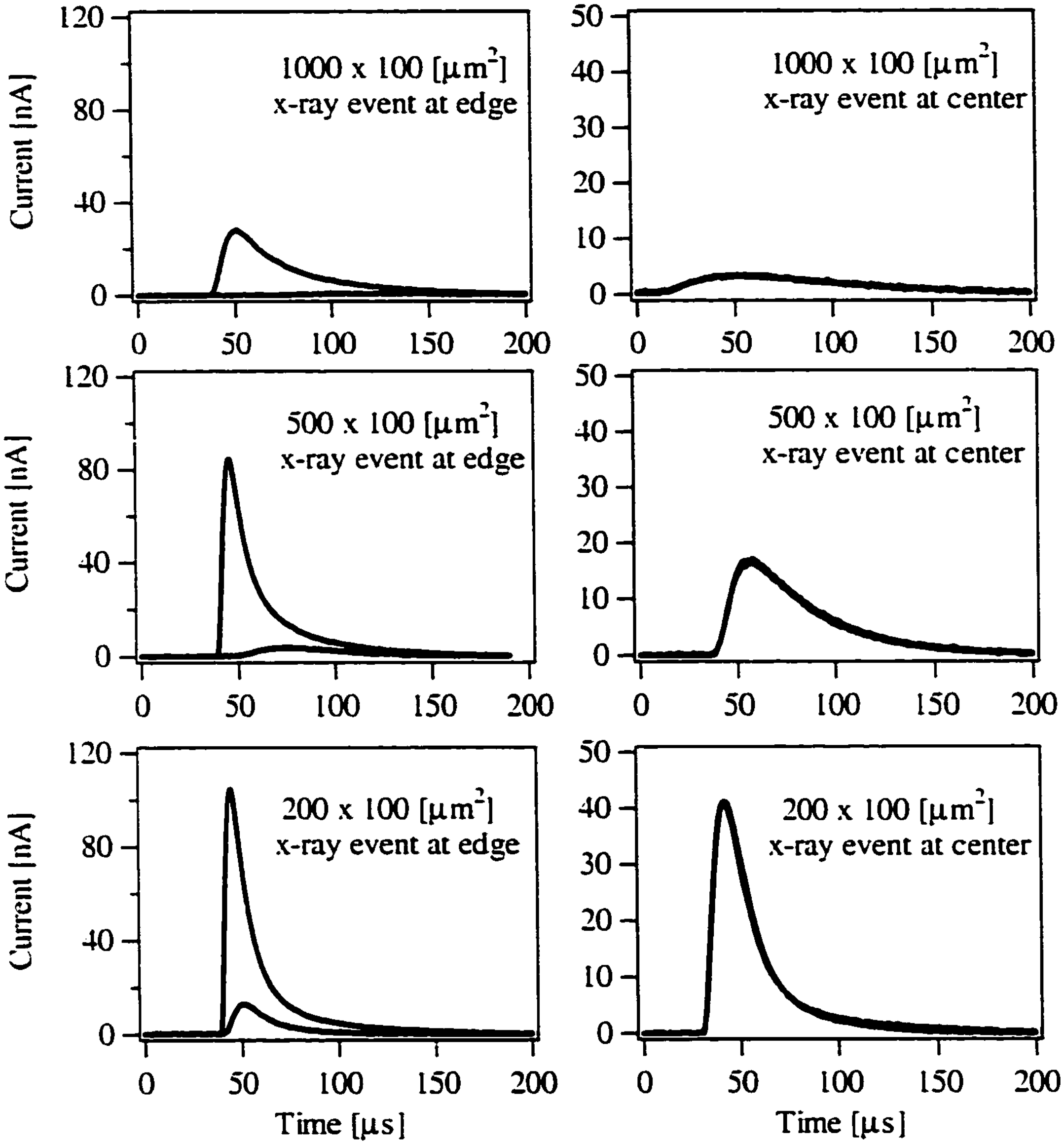

Fig. 5.12 The current pulses generated by x-ray events at different locations on the three devices (device E, F and G). Left panels: x-ray events occur near one edge of the absorbers. Right panels: x-ray events occur in the center of the absorbers. (device E, 1/22/01; device F, 3/6/01; device G, 3/19/01)

In Fig. 5.12 the current pulses in the 500 μm long device last about twice as long as those in the 200 μm long device. If there is no quasiparticle loss in the Ta absorber, the amplitude of the signal should be halved by assuming the same amount of quasiparticles is created by the x-ray photon in both devices. Since the measured quantity is the current, an integration on the current pulse has to be performed to obtain the charge. We can assume the same amount of electronic noise for all the measurements. The charge noise will increase as the integration time since the charge noise is proportional to the square root of the integration time T_{pulse}.

The loss of quasiparticles increases exponentially as a function of the time that the quasiparticles stay inside the absorber. This will cause large fluctuations in the collected quasiparticle numbers. Assuming that each quasiparticle has the probability β of being lost in the Ta absorber, the statistical noise caused by the quasiparticle loss in the absorber is [Segall, 98]

$$\Delta E_{abs} = 2.355\sqrt{\frac{\beta}{1-\beta}\varepsilon E} \,. \tag{5.18}$$

The device with a 200 μm long absorber has a small statistical noise since the absorber loss is small. But for the device with a 1000 μm long absorber, the loss probability β of 75% gives a statistical noise 10 eV for a 5895 eV x-ray photon. This noise is already much larger than the statistical quasiparticle creation noise. Another large effect of the quasiparticle loss is that it reduces the signal amplitude. The broadening due to the electronic noise is inversely proportional to the signal amplitude. The electronic noise of our setup is around 10 eV for the 200 μm long device with a bandwidth of 100kHz. But due to the 75% quasiparticle loss in the 1000 μm long absorber, the energy resolution caused by the electronic noise can easily go up to $\Delta Q / Q = 10\ \mathrm{eV} / 0.25 = 40\ \mathrm{eV}$. To make the device practically usable, the electronic noise has to be brought down to be smaller than the statistical creation noise.

5.3.2 Diffusion Constant and Lifetime

The quasiparticle diffusion constant in the Ta absorber can be derived from the measured current pulses from the two junctions. When an x-ray photon is absorbed near one side of the Ta absorber, it takes different time for the quasiparticles to diffuse into the

Al traps that connect to the two ends of the absorber. By studying the time delay between the two current pulses the diffusion constant can be calculated [Segall, 00b].

In practice, the above approach relies on the information of the x-ray event location which is typically calculated based on very simple assumptions [Kraus, 89]. Instead, we utilize the following procedure.

1. Fit the Q1 vs. Q2 plot to find the loss parameter α.
2. Fit the current pulses created by two x-ray events to obtain three parameters: the total charge Q_{total}, the diffusion constant, and the outdiffusion time. Two events are needed because the current pulses are location sensitive. They are chosen so that they all approximately lie along the center line of the delay time vs. I_{peak} plot (Fig. 5.14), but one has a long delay time and the other has a short delay time. The total charge parameter controls the amplitude of the pulse, the diffusion constant controls the duration of the pulse, and the outdiffusion time describes the behavior of the tail of the pulse. Fig. 5.13 shows the fitting for one x-ray event pulses and the agreement is quite good. In this figure, we also show how the delay time is read between two current pulses for the same x-ray event. The delay time is the time interval between the two pulses in the two junctions at a given current threshold. The parameters obtained in this step serve as initial values for the next step fitting.
3. Use the three parameters determined in step two as initial values to fit the delay time vs. I_{peak} for the three devices. The current threshold for determining the delay time is 2 nA for the 200 μm and the 500 μm long devices and 1 nA for the 1000 μm long device. Fig. 5.14 shows the experimental delay time vs. I_{peak} as well as the numerical fitting for the three devices. As can be seen, the overall fitting of the data is quite good. When the peak current in one junction is small, the uncertainty in determining the delay time increases. Thus the fitting becomes slightly worse when I_{peak} is small. This also happens when I_{peak} is large, because a large I_{peak} in one junction means a small I_{peak} in the other junction.
4. Check the values of the three parameters by comparing the numerically simulated I_{peak1} vs. I_{peak2} with the experimental data. Fig. 5.15 shows the comparison. The agreement between the simulation and the data is very good.

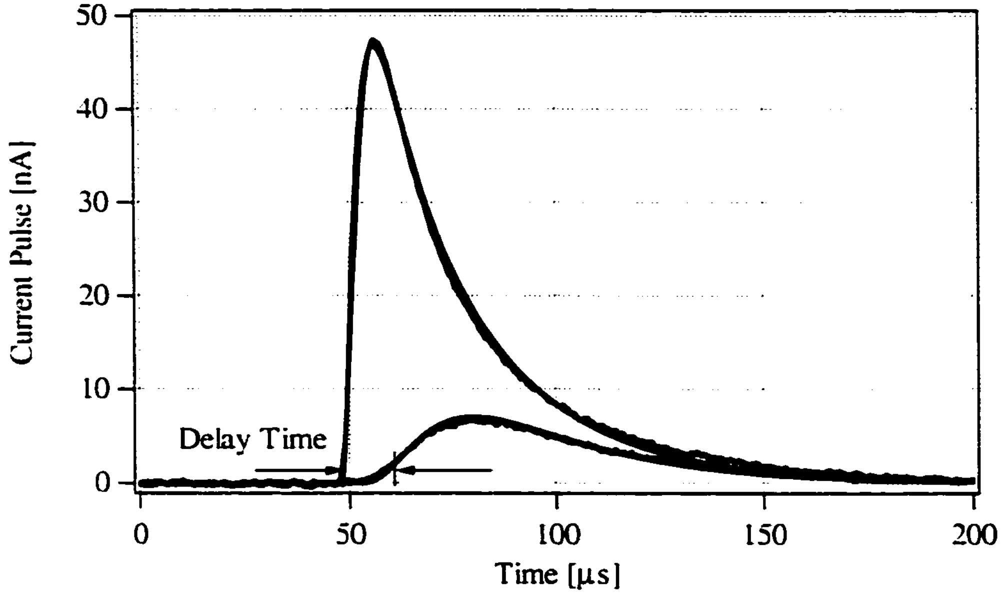

Fig. 5.13 The current pulses of one x-ray event absorbed in device F (500 μm long device). Both the experimental data and the fitting from the numerical model are shown. The delay time is the time interval between the two current pulses at the same current threshold. (device F, 3/6/01)

After the loss parameter α and the diffusion constant D are fitted from the data, the quasiparticle lifetime in the Ta film can be calculated from (5.17). Both the quasiparticle lifetime and diffusion constant are listed in Table 5-4. The average value of the diffusion constant in the superconducting Ta film is 8.2 ± 0.2 cm^2/s, while the average quasiparticle lifetime is 83 ± 5 μs.

Absorber Length L [μm]	200	500	1000
Quasiparticle lifetime τ_{loss} [μs]	87	83	78
Diffusion constant D [cm^2/s]	8.2	8.3	8.0

Table 5-4 The diffusion constant and the lifetime of quasiparticles in the Ta absorber film for three devices (E, F, G).

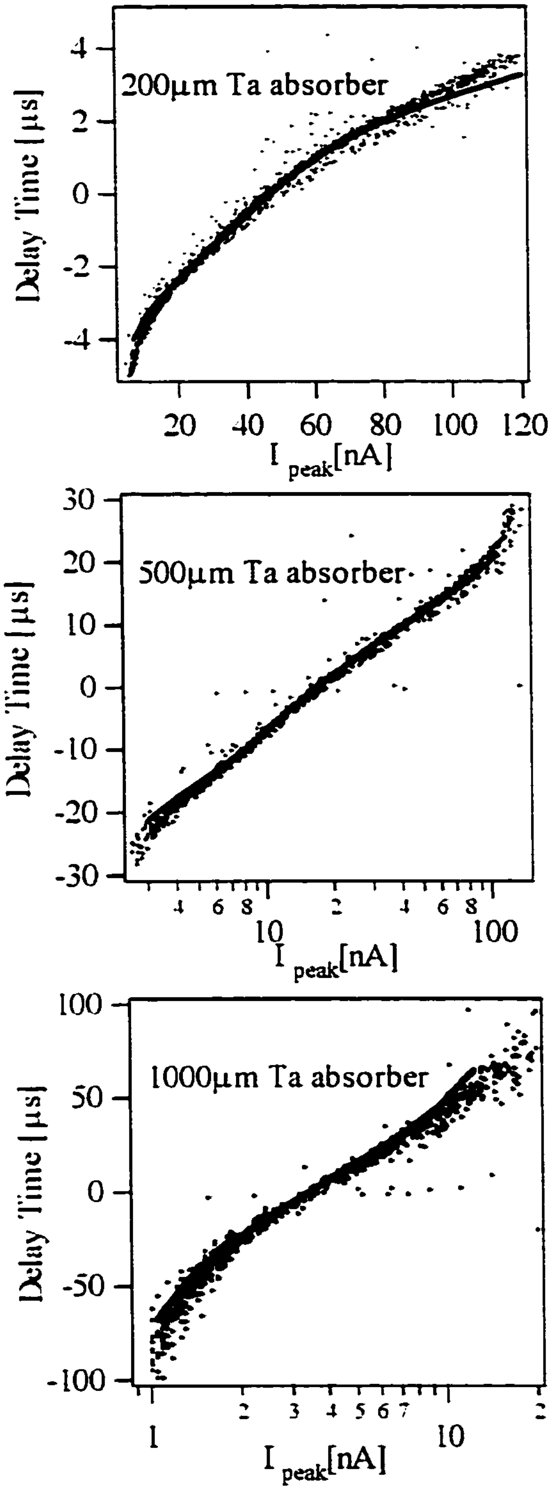

Fig. 5.14 Delay time vs. I_{peak} for all three devices. Dots are the experimental data, solid lines are the fitting curve. (device E, 1/22/01; device F, 3/6/01; device G, 3/19/01)

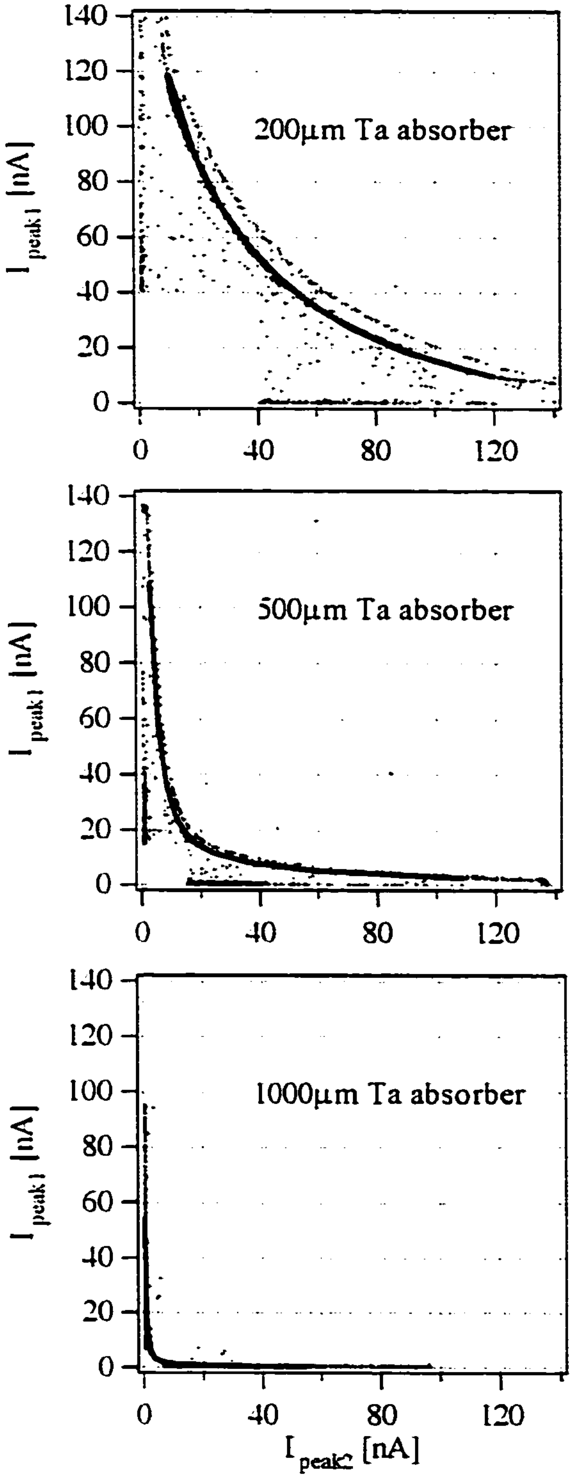

Fig. 5.15 I_{peak1} vs. I_{peak2} for all three devices. The dots are the experimental data and the solid line is the fitting of the model. (device E, 1/22/01; device F, 3/6/01; device G, 3/19/01)

5.3.3 Discussion

Due to the difficulty of focusing x-ray beams in astronomical applications, large x-ray absorbers are required. The detectors would have to span at least on the order of a millimeter. To successfully scale the absorber length from 200 μm to 1mm and still preserve the good energy resolution, a higher diffusion constant and longer quasiparticle lifetime are required. A longer quasiparticle lifetime reduces the quasiparticle loss, while a higher diffusion constant improves the time response of the detectors.

The normal state diffusion constant of the Ta film can be calculated from the following Einstein equation

$$D_N = \frac{1}{\rho_N e^2 n(E_F)}, \tag{5.19}$$

where $n(E_F) = (7.1 \pm 0.3) \times 10^{22}\,\mathrm{eV^{-1}cm^{-3}}$ is the density of states at the Fermi surface and ρ_N is the resistivity of the Ta film in the normal state. With a measured residual resistance ratio (***RRR***) of 17 and resistivity, $\rho_N = 0.70 \pm 0.05$ μΩ–cm, the normal state diffusion constant is $D_N = 130 \pm 20\ \mathrm{cm^2/s}$.

If the Ta film is superconducting, the quasiparticle dispersion relation has a minimum at the Fermi energy where the density of states diverges. In the thermal equilibrium state, the diffusion constant of a superconductor is given by [Narayamurti, 78]

$$D_{sc} = D_N \sqrt{\frac{2k_B T}{\pi\Delta}}. \tag{5.20}$$

At temperature $T = 0.21\mathrm{K}$, the thermal equilibrium diffusion constant, D_{sc}, is 17 $\mathrm{cm^2/s}$. When an x-ray photon is absorbed in the Ta film, the created quasiparticles are under non-equilibrium conditions. The energy distribution of the quasiparticles as a function of time can be calculated using the scattering time [Kaplan, 76]. From the energy distribution the average diffusion constant can be computed. Because the non-equilibrium state has more energy than the equilibrium state, the diffusion constant at the non-equilibrium state is larger than that at the equilibrium state. Using the simulations on the quasiparticle relaxation processes [Friedrich, 97], the effective diffusion constant at the non-equilibrium state is $\boldsymbol{D_{eff}}$ = 27 cm^2/s. Thus, the measured diffusion constant $\boldsymbol{D}$ = 8.2 cm^2/s is significantly smaller than what theory and simulations predict.

So far there is no satisfying explanation of the small diffusion constant in the Ta film. One hypothesis is that there is a random scattering process at the grain boundary of the polycrystalline Ta film. Another hypothesis is that small gap variations exist inside the Ta absorber film at the grain boundaries.

The Ta film of our device has a densely packed grain structure. It is sputtered on the SiO_2 surface under the deposition condition of T ≈ 700 °C and 6 mtorr Ar [Gaidis, 94]. The dense structure prevents oxygen from diffusing into the film rapidly so that it helps form stable high quality x-ray absorbing films. However the dense structure also causes substantial stress between the boundaries because there are not enough voids to relieve the stress within the Ta grains [Gaidis, 94]. When quasiparticles hit these boundaries, they will either go through the boundaries or scatter back. The scattering at the boundaries may slow the quasiparticles down.

Another explanation is that the slow diffusion might be caused by intrinsic gap variations. The intrinsic gap anisotropies are related to the Fermi surface, the electron wave functions, the phonon spectrum, and the electron phonon matrix element. The variation of the intrinsic gap would constrain the quasiparticles to a lower energy gap region and thus confine the quasiparticles longer in the absorber. Critical magnetic field measurements indicate a 12% anisotropy [Bostock, 77].

The diffusion constant of the Ta film could be improved by using different crystal structure in the future. One choice is to use epitaxial Ta film. The epitaxial Ta film has a single crystal structure instead of a polycrystalline structure, so the boundary scatterings can be eliminated. One European group tried to use epitaxial Ta films as x-ray absorbers and observed higher residual resistance ratio (***RRR***) and a diffusion constant twice as large as our measurements [den Hartog, 01]. Their diffusion constant, however, is still smaller than the theoretical value.

The measured quasiparticle lifetime in the Ta film is about 80 μs. It is much shorter than the theoretical 1.7 ms. It has been shown in Ref. [Friedrich, 97] that the quasiparticle loss in device A is not sensitive to temperature below 0.3 K. This suggests that the uniform quasiparticle loss in the Ta film is due to some non-thermal processes.

One source for the short quasiparticles lifetime might be due to the anisotropic energy gap in the Ta polycrystal film. The quasiparticles might be trapped in the lower energy region and eventually get lost by recombining into Cooper pairs.

The second loss source may be caused by the defects in the Ta film. The defects might trap magnetic flux. Once the flux is trapped, the defects become quasiparticle loss centers. The use of epitaxial Ta films will possibly reduce these defects.

Another possibility is that the phonons escape into the substrate faster than expected. The way to test this is to change the thickness of the Ta film and measure the quasiparticle lifetime as a function of the thickness.

The limit on the size of the absorber for astronomical applications is determined by the combination of the diffusion constant and the quasiparticle lifetime, i.e., by the loss parameter α For the measured quasiparticle lifetime of 83 μs and the diffusion constant of 8.2 cm^2/s, the maximum absorber length is 500 μm. However after carefully studying the sources of quasiparticle loss and slow diffusion, there is a good likelihood fulfilling the astronomical requirement of the absorber length in the future.

Chapter 6 Four-Junction Devices

Instead of using two junction devices to implement single photon 1-D imaging STJ detectors. we explore the possibility of using four junction devices to do 2-D imaging for applications in x-ray astrophysics. By analytical and numerical simulations of the quasiparticle diffusion process. we study two types of designs for doing 2-D imaging: (1) a square Ta absorbers with four Al junctions attached to each side. and (2) a square absorber with four Al junctions attached in each corner. By measuring the charge collected by the four junctions. we can determine both the energy and spatial resolution of the x-ray events. By comparing the two designs. the device design with junctions on the four sides of the absorber gives better spatial performance [Li. 00].

6.1 The Quasiparticle Diffusion Process

The number of quasiparticles created is proportional to the energy of the photon. The quasiparticles diffuse in the absorber and are collected in the traps. They tunnel through each junction. When an x-ray photon is absorbed at time $t = 0$ at position $x = x_0$. $y = y_0$. the dynamics of the quasiparticle distribution $n(x, y, t)$ inside the absorber can be described by a standard diffusion equation including a term for quasiparticle loss on a time scale of τ_{loss} to account for the finite quasiparticle lifetime. Since the process of quasiparticle generation is fast compared to the diffusion process inside the absorber. the initial distribution can be assumed to be point-like. Quasiparticles at the absorber-trap interfaces will be trapped into the trap by inelastic scattering. The resulting differential equation is

$$\frac{\partial n(x,y,z)}{\partial t} = D\nabla^2 n(x,y,t) - \frac{n(x,y,z)}{\tau_{loss}}, \tag{6.1}$$

with the initial condition

$$n(x,y,0) = N_0\delta(x - x_0, y - y_0), \tag{6.2}$$

where D is the diffusion constant and N_0 is the total number of charges generated by the x-ray photon.

We will apply the above model on two different designs of the 2-D imaging four junction detectors. The two designs are shown in Fig. 6.1. The left hand side device has four STJ junctions with one junction on each side of the absorber, while the right hand side device has four junctions with one junction in each corner.

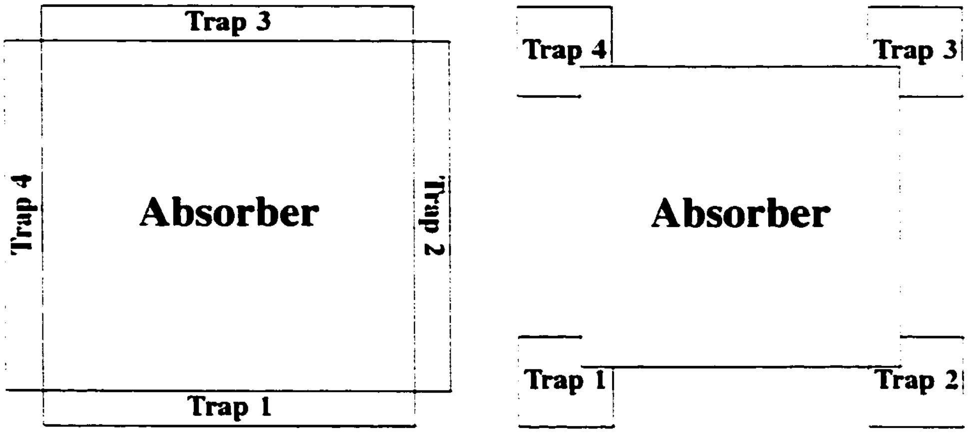

Fig. 6.1 The left design is a square absorber with junctions on each side. The right design is a square absorber with junctions in each corner.

6.2 Design with Junctions on Each of the Four Sides

In the devices that we have studied so far, the trapping is close to be perfect. It is realistic to choose perfect boundary condition as [Kraus, 89]

$$n\big|_{x=0,\ x=L}=0,\quad n\big|_{y=0,\ y=L}=0, \tag{6.3}$$

where L is the length of the absorber. The charge Q_1 collected in trap 1 can be calculated analytically from

$$Q_1(x,y)=\frac{4}{\pi}Q_0\sum_{m=1}^{\infty}\frac{\sin((2m-1)\frac{\pi x}{L})}{2m-1}\times\frac{\sinh\left(\sqrt{(2m-1)^2+\frac{L^2}{\pi^2 D\tau_{loss}}}\left(1-\frac{y}{L}\right)\pi\right)}{\sinh\left(\sqrt{(2m-1)^2+\frac{L^2}{\pi^2 D\tau_{loss}}}\,\pi\right)} \tag{6.4}$$

where $Q_0 = eN_0$ is the total charge produced by the incident x-ray photon. Charges Q_i, (i=2,3,4) collected in other traps are calculated similarly.

Fig. 6. shows the contour plot of the fraction of the total charge vs. position of the x-ray events. If the x-ray event is close to one junction, most of the charge will be collected by that junction. The farther the photon absorption event is from a junction, the fewer quasiparticles can be collected by that junction. If there are only two junctions on the

opposite sides of the absorber, the contour plot will be straight line. The bending of the equal collection lines shows the effect of the addition of the two extra traps. They act as trapping sinks that strongly reduce the collection power of the selected junction. This behavior will be the same for all the junctions of the device. The charge collected at each of the four junctions give the necessary information to determine both the photon energy and the position of the x-ray absorption event, which can be used to implement 2-D imaging. In order to calculate the spatial resolution, we introduce combination variables

$$f = Q_1/(Q_1+Q_3) \text{ and } g = Q_2/(Q_2+Q_4). \qquad (6.5)$$

Let's denote the RMS charge noise for junction i (i = 1,2,3,4) by ΔQ_i. From the $\Delta Q_i/Q_0$ ratios, the spatial resolution can be calculated.

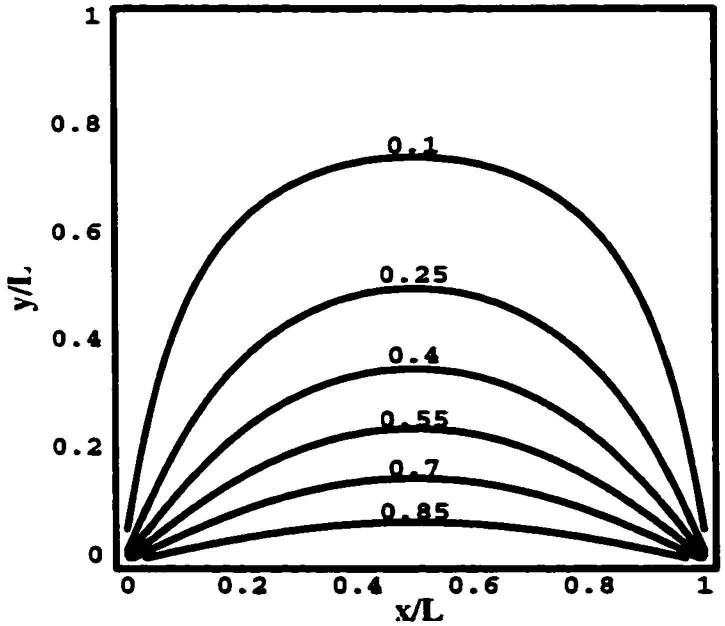

Fig. 6.2 Contour plot of the fraction of total quasiparticle charge collected in trap 1 Q_1/Q_0 as a function of the position of the x-ray events. We assume there is no loss in the absorber and perfect trapping.

We define

$$a_{11}(x,y) = \frac{\partial f(x,y)}{\partial x}, \quad a_{12}(x,y) = \frac{\partial f(x,y)}{\partial y},$$
$$a_{21}(x,y) = \frac{\partial g(x,y)}{\partial x}, \quad a_{22}(x,y) = \frac{\partial g(x,y)}{\partial y}. \qquad (6.6)$$

Assume that the noise of the charge readout from the four junctions is not correlated and equal to ΔQ. Then

$$\sqrt{\overline{(\Delta x_i)^2}} = \frac{\Delta Q}{|a_{11}a_{22} - a_{21}a_{12}|} \times \left(\frac{a_{2i}^2}{(Q_1 + Q_3)^4}(Q_1^2 + Q_3^2) + \frac{a_{1i}^2}{(Q_2 + Q_4)^4}(Q_2^2 + Q_4^2) \right)^{1/2} \quad (6.7)$$

where $i = 1,2$, $\Delta x_1 = \Delta x$, and $\Delta x_2 = \Delta y$.

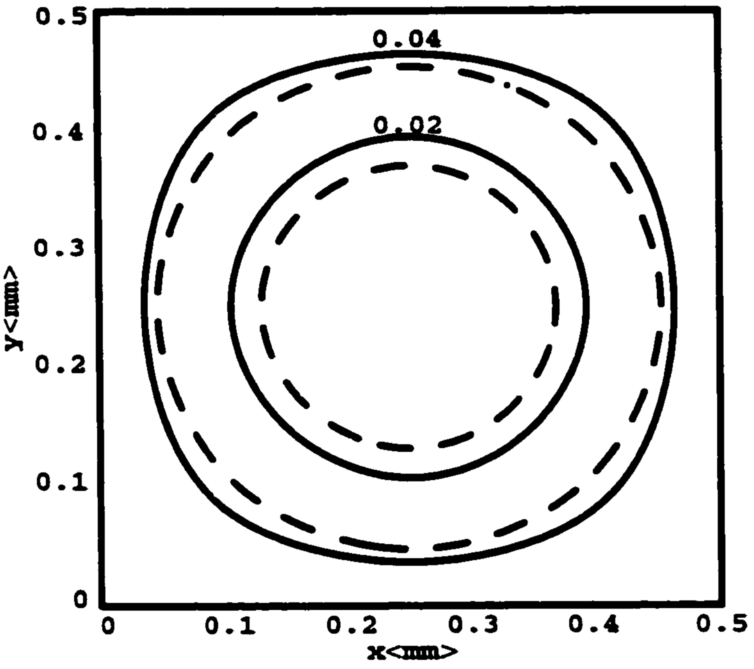

Fig. 6.3 Contour plot of the spatial resolution $\Delta r/L$ of a 0.5mm × 0.5mm absorber with junctions on four sides. The solid contour line is the spatial resolution with no charge loss. The dashed contour line is the spatial resolution with charge loss. For each junction we assume that the readout has charge noise of $\Delta Q_i/Q_0$=0.01.

Fig. 6.3 shows the normalized spatial resolution $\Delta r / L = \sqrt{(\Delta x)^2 + (\Delta y)^2} / L$ depending on the position of the photon absorption, with loss and without loss in an absorber of 0.5mm × 0.5mm size. We assume $\Delta Q_i/Q_0$=0.01. In the case of quasiparticle loss, we use the diffusion constant and quasiparticle lifetime derived in Chapter 5, D = 8 cm^2/s, τ_{loss} = 83 μs. From the plot the spatial resolution in the center is better than that in the region near the edges. This can be explained by the symmetry consideration. If the x-ray event is close to one junction, the charge collected by the other three junctions will be small. The overall signal-to-noise ratio is thus smaller, and this degrades the spatial resolution. In both cases (with loss and without loss), the spatial resolution is better than 2% in the center region. Comparison reveals that the spatial resolution is slightly worse if there is quasiparticle loss, as expected.

6.3 Design with Junctions in Each of the Four Corners

The boundary condition for Eq. (6.1) changes to $n = 0$ at the four corners and the quasiparticles are reflected at the other parts of the boundary. In the simulation, the corner traps are assumed to extend over 10% of each side. Due to the complexity of the boundary condition problem, the random walk method [Tobochnik, 89] has to be used to solve for the charge collected at each of the four corners. Fig. 6.4 shows the simulated results of the fractional charge collected in trap 1 assuming there is no quasiparticle loss.

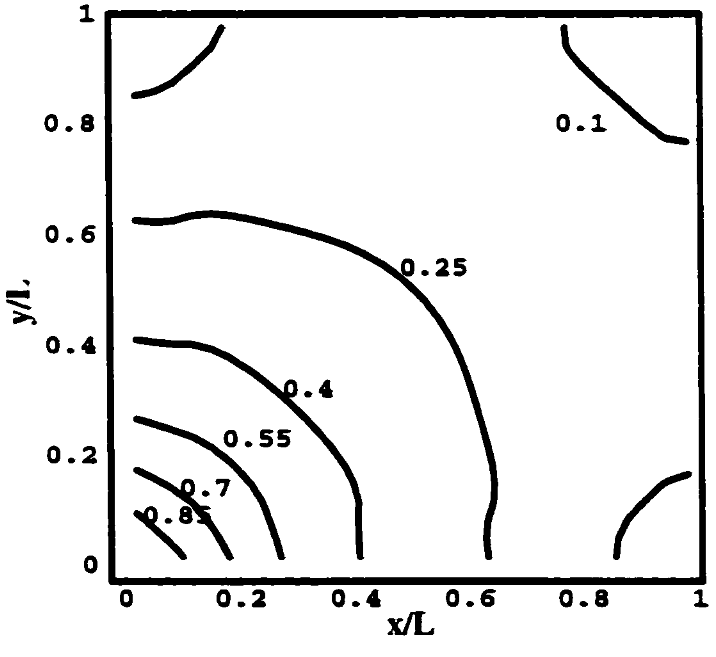

Fig. 6.4 Contour plot of the fraction of the total quasiparticle charge collected in trap1 Q_1/Q_0 as a function of the position of x-ray absorption events. We assume there is no loss in the absorber and perfect trapping.

Similar to Eq. (6.3), the same variables *f* and *g* are defined to determine the location of the x-ray absorption event. Fig. 6.5 shows the spatial resolution normalized to the absorber size.

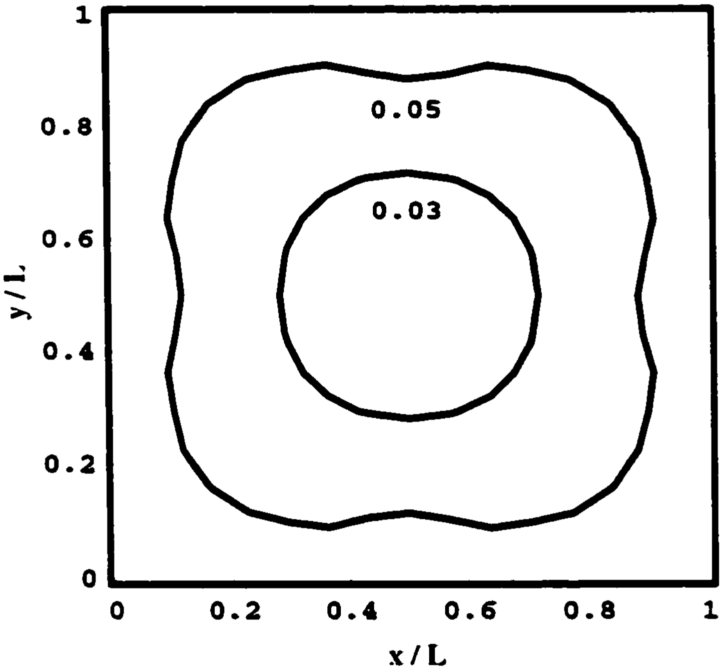

Fig. 6.5 Contour plot of the spatial resolution Δr normalized to the absorber size with junctions in four corners. For each junction we assume that the readout channel has charge noise of $\Delta Q_i/Q_0 = 0.01$.

Comparing the two designs, the device with the junctions on the four sides shows better spatial resolution than the device with the junctions in four corners. In fact, in spite of the better spatial separation of charge in the four-corner junction device, we lose information about the charge position near the center of the edges due to random reflection of the quasiparticles at the boundary with no traps. This device with junctions at four corners is more sensitive to the loss of quasiparticles because its junctions take a longer time to collect the quasiparticles generated by the x-ray photons.

6.4 Summary

We numerically studied two designs of four junction devices [Li, 00]. Our results show that they can provide good 2-D imaging. The loss of quasiparticles in the absorber affects the spatial resolution of the devices. With the lifetime we measured in the two-junction device (device B), the 1mm×1mm absorber can provide very good spatial resolution. The advantage of such 4-junction devices compared to arrays of single pixel detectors [Rando, 98, Chervenak, 99] is that one can implement 2-D imaging with only 4 readout channels to effectively achieve 10^3 or more pixels.

Chapter 7 Long Decay of the Pulses

We have observed that the x-ray current pulses for both device B and C have long decay time as shown in Fig. 7.1. The decay time for device B and C is about 110 μs, while it is about 20 μs for device A (same for E, F and G). The steep rise and the initially sharp fall of the pulses for devices A and C are very similar because both devices have the same junction structure. However the pulse of device C differs from that of device A in its long decay. Device B also has long decay time as device C does, but the magnitude of the decay is smaller than that of device C.

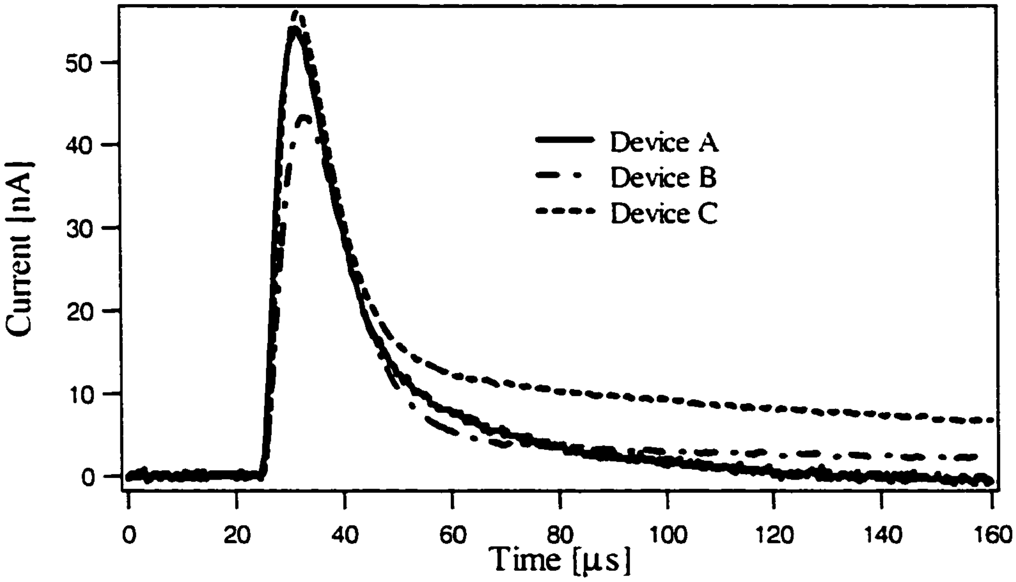

Fig. 7.1 The pulses generated by the x-ray photon absorption events in the center of device A, B and C. The pulses for device B (dot-dashed line) and C (dashed line) have long decays (tails), but the pulse from device A (solid line) doesn't. (device A, 2/26/98, [Segall, 00b]; device B, 5/22/00; device C, 7/26/00)

In Fig. 7.1, we can divide the decay into two stages. The first stage is the fast decay right after the peak current. This stage is almost the same for all devices and it lasts for about 10 μs. After the fast decay, the tunneling current is significantly reduced in the second stage. Due to the different pulse shapes for different devices, we conjecture that there might be two different processes involved in the removal of the quasiparticles in the junctions.

7.1 Characters of the Long Decays

The long decays have some special characters that can help understand their origin. First, the magnitude of the long pulse tails scales with the total charge of the pulse. If we scale the two pulses by the charge collected in each junction for the same x-ray event, the magnitude of the scaled pulses coincide with each other in the long decay part. Fig. 7.2 shows the pulses collected in the two junctions of device C for the same x-ray event. The dot-dashed line denotes the pulse measured in junction 1, while the dashed line is the pulse in junction 2. The solid line is pulse 1 after being scaled by the charge ratio Q_2/Q_1. The solid line and the dot-dashed line match quite well in the tail region. This feature tells us that the long decay is caused by the photon event that generates the pulses. Thus we can exclude the random substrate events from playing any role in this phenomenon.

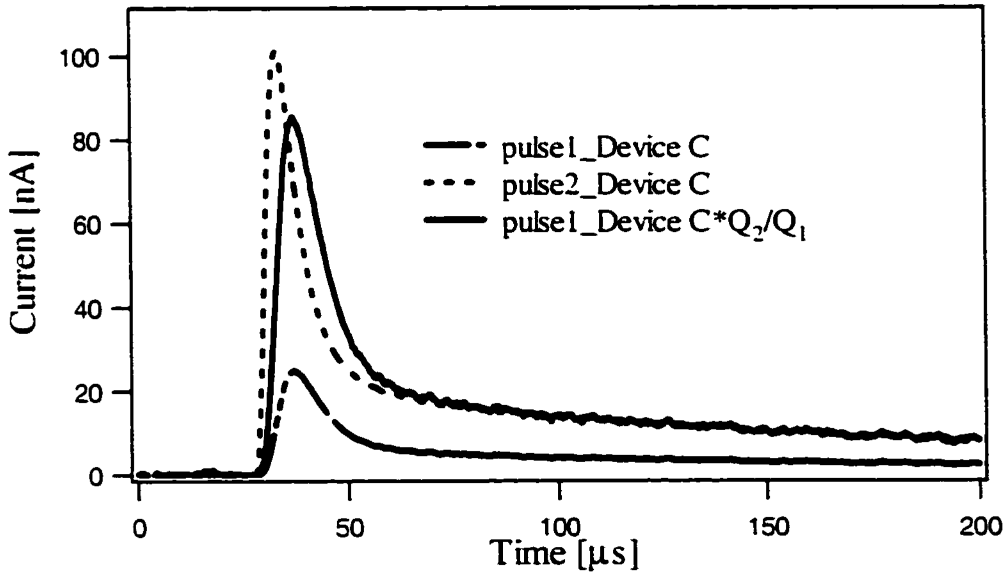

Fig. 7.2 The current pulses from the two junctions of device C. The photon event is absorbed near junction 2. After the pulse 1 is scaled by the charge ratio Q_2/Q_1, the tails of the scaled pulse and pulse 2 match quite well.

Second, the magnitude of the long decay scales with the junction area. The magnitude of the long tail for device B is smaller than that for device C if the x-ray absorption event occurs in the same *x* location. Let's focus on x-ray events occurring in the center of the absorber so that the pulses measured in both junctions are the same. The area of device B is only one third of the area of device C. This leads to the magnitude of the tail for device B to be one third of that for device C as shown in Fig. 7.. This observation is confirmed by the perfect tail matching between the scaled pulse for device B and the pulse for device C. The scaling by junction area indicates that the quasiparticle densities are the same in the junction region for different devices. Then the long tail must be caused by something other than the junction.

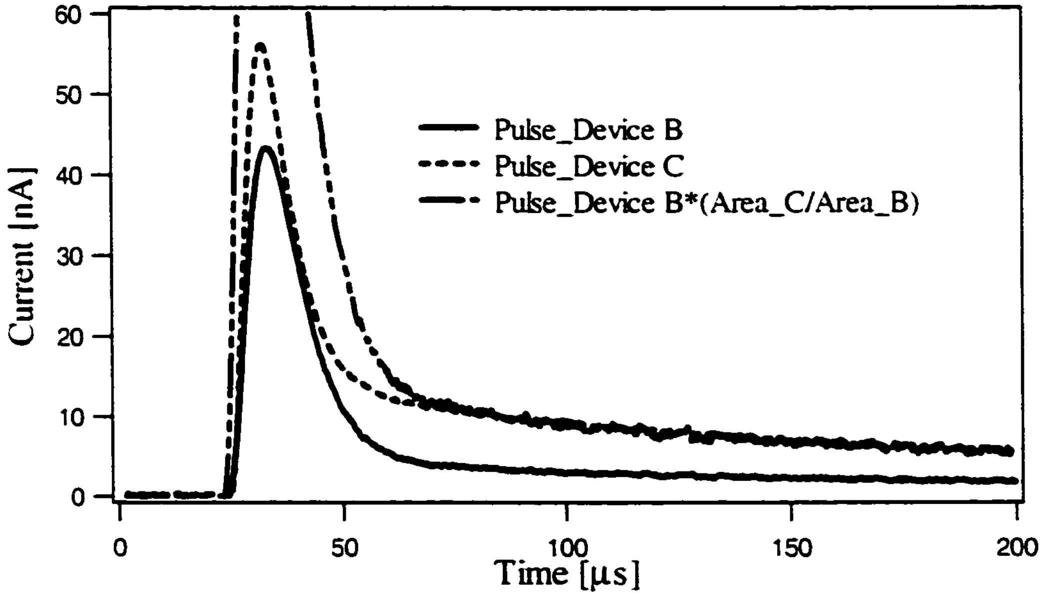

Fig. 7.3 Pulses generated by the x-ray photon absorption events in the center of both devices B and C. The pulse for device C (dashed line) has a larger tail than that for device B (solid line). However the tail of the area scaled pulse for device B (dot-dashed line) matches the tail for device C.

7.2 Constrained Slow Out-Diffusion

We now turn our attention to the wiring pad. Fig. 7.4 shows the two pulses when an x-ray event is not absorbed in the Ta absorber but in the wiring pad. Because the Ta absorber prevents quasiparticles created in the wiring pad from going from one junction into the other junction, only one junction can detect non-zero signal. The significance of such events in the wiring pad is its long decay time. Unlike the pulses generated from events occurred in the Ta absorber, pulses generated in the wiring pad show only the slow decay process. However the slow decay feature is very similar to the long tails observed in the pulses generated from x-ray events in the Ta absorber. We intend to find an answer to the long tails of the pulses by explaining the slow decay of the wiring pad pulses.

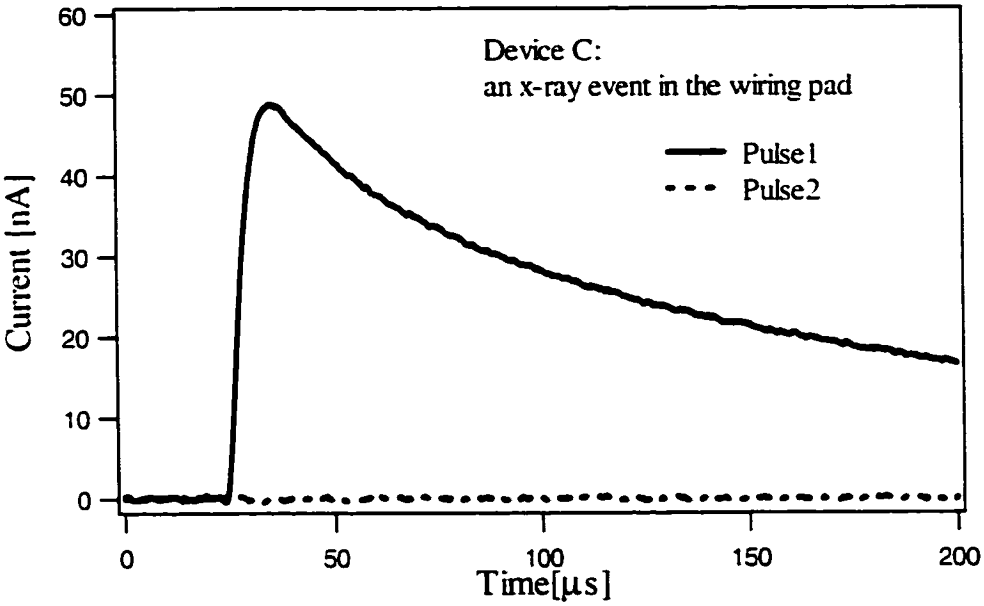

Fig. 7.4 The pulses of an x-ray event absorbed in the wiring pad of junction 1 for device C. The pulse decays very slowly as observed in the x-ray events occurred in the Ta absorber. Pulse 1 (2) is from junction 1 (2).

Even though device A and C have the same junction structure, they have different wiring designs. While device B and C have the same wiring design. The design of the wiring pad of device A and C is shown in Fig. 7.5. Device C consists of a wide wiring pad of 200 x 250 μm^2 and a 50 μm lead connected to it. Device A has a wiring pad of 35 x 250 μm^2 and a 50 μm lead connected to it. The difference in the wiring design between these two devices is the wiring width to the lead width ratio. The wide wiring pad design for device C is intended to improve the quasiparticle out-diffusion. However, the narrower lead dramatically slows down the quasiparticle out-diffusion process. In device A, the lead width is comparable to the wiring pad width so that there is no constraint in the quasiparticle out-diffusion process.

7.3 Qualitative Study of the Slow Decay

The slow decay or (long tail) we observed in device B and C can be qualitatively explained by the device design difference. In these two devices, after quasiparticles tunnel from the trap to the counterelectrode, they fast diffuse into the wiring pad. After about 10 μs, they quickly fill up the wiring pad. Then the quasiparticle diffusion is slowed down by the narrower lead. This constrained out-diffusion process causes the slow decay of pulses for device B and C.

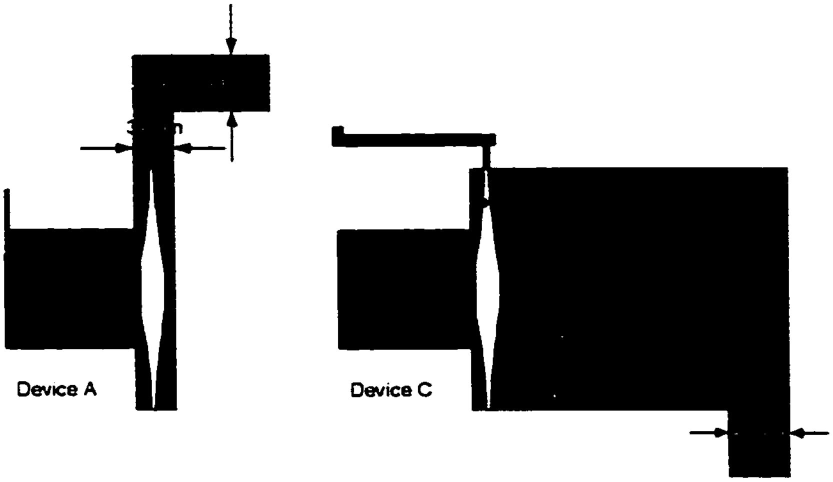

Fig. 7.5 The wiring structure of device A and C.

The two characters we discussed earlier can be explained now. Since the delay time between the two pulses is less than 10 μs, the quasiparticles fill the wide wiring pad almost 'simultaneously'. Then they begin to slowly diffuse out from the narrow lead. In parallel to the thermal quasiparticle current calculation, the tunnelling current is proportional to the quasiparticle density Q_i/V_{wiring}, here Q_i is the charge of excess quasiparticles in the Al wiring pad. Therefore the magnitude of the long decays is proportional to the total charge measured from the junction. If we consider x-ray events occur at the same x location for device B and C, the quasiparticle density Q_i/V_{wiring} will be the same. Since the tunnelling barriers for both devices have the same transparency. the tunnelling current scales with the junction area.

7.4 Quantitative Study of the Slow Decay

Numerical simulations can now be used to quantitatively verify our explanations. We make a simple assumption that the quasiparticle density in the wiring pad is constant and quasiparticles propagate in the lead by diffusion. The objective of the simulation is to see how the width of the lead affects the quasiparticle out-diffusion in the wiring pad. We treat the wiring pad as the quasiparticle reservoir. Two configurations shown in Fig. 7.6 are simulated. The configuration (a) consists of a large reservoir connected by a narrow lead. The configuration (b) is a simple 1-D diffusion with reflecting boundary at $x=0$. W and L are the width and length of the reservoir for configuration (a), respectively.

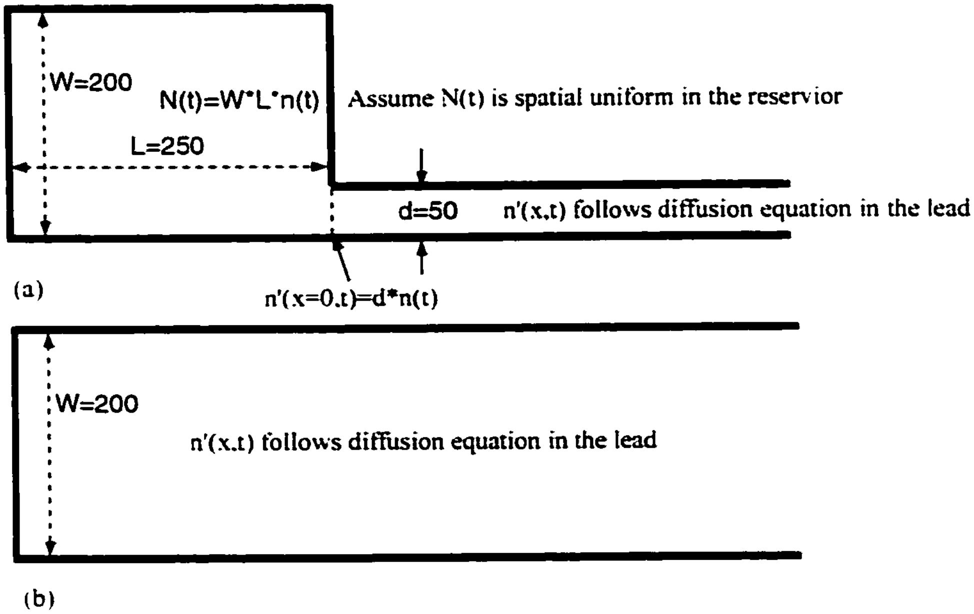

Fig. 7.6 The wiring pad configuration used for simulation. Configuration (a) is a large reservoir connected by a narrow lead. Configuration (b) is a 1-D diffusion with reflecting boundary at $x=0$.

We use the 1-D diffusion equation in our simulation. The boundary condition for diffusion in the lead can be described by

$$\frac{dN(t)}{dt} = D_{Al} \frac{dn'(x,t)}{dx}\bigg|_{x=0}, \tag{6.8}$$

where $N(t)$ is the number of particles in the reservoir, $n(t)$ is the number of particles per unit area, $n'(x,t)$ is the number of particles per unit length in the lead and it follows the diffusion equation, $n'(x=0,t) = n(t)\times d_{ld}$, where d_{ld} is the width of the lead.

The width and length of the reservoir are W = 200 μm, L = 250 μm respectively. The width of the leads is $d_{ld} = 50\,\mu m$ for (a) and $d_{ld} = 200$ μm for (b). The lead length is 1000 μm. The diffusion constant of Al D_{Al} is 60 cm^2/s [Friedrich, 97]. In the simulation we assume that there is no quasiparticle recombination loss and the initial condition $n'(x,t=0)$ is a half Gaussian function with $x = 0$ and $\sigma = 12.5\,\mu m$. At the other end of the lead, the trapping time is 10 μs. The simulation results are not very sensitive to the trapping time when the length of the lead is very long.

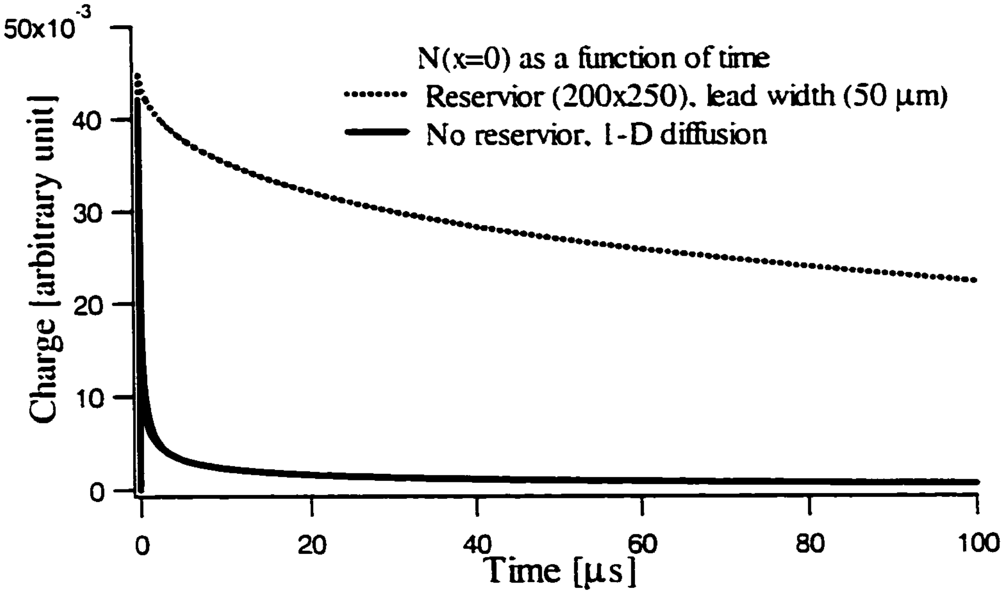

Fig. 7.7 The simulation of quasiparticle out-diffusion in different configurations. The dotted line shows the change of quasiparticle density in the reservoir connected by a narrow lead. The solid line shows the change of quasiparticle density without reservoir.

The simulated results of $N(t)$ and $n'(x,t)$ are shown in Fig. 7.7. The y-axis is in arbitrary unit. From Fig. 7.7, we see a narrow lead in the configuration (a) dramatically slows the quasiparticle outdiffusion, while if the wiring pad width and the lead width are comparable, the diffusion is much faster.

Then we estimate the magnitude of the tails. We assume that a 6 keV x-ray photon absorbed in the Al wiring pad creates about 15×10^6 quasiparticles. The total volume of the wiring pad and Al junction is 1.90×10^4 μm^3. If the created quasiparticles are uniformly distributed in the wiring pad, the density of the quasiparticle is $15\times10^6 / 1.90\times10^4 \mu m^3 = 779 / \mu m^3$. The thermal quasiparticle density at T = 0.215 K is $n_{th} = 2N_\sigma\sqrt{2\pi\Delta k_B T}e^{-\Delta/k_B T} = 212/\mu m^3$, where N_σ is the single spin density of states at the Fermi level and is $1.2\times10^{22} / eVcm^3$. The ratio of the excess quasiparticle density and thermal current density is then $779/212 = 3.67$.

At T = 0.215 K, the measured thermal subgap current I_{subgap} is 20 nA for device C and 7 nA for device B. The peak current of the photon events in the wiring pad is around 50~60 nA for device C and 15~20 nA for device B. So the peak current is about a factor 2.5~3 larger than the thermal current. If the junction can be seen as excess quasiparticle density detector, the magnitude of the long decays of the events in the wiring pad is expected to be roughly 3.67 times of the thermal current. This estimation agrees with the experimentally measured results.

If an x-ray photon is absorbed in the Ta absorber, the quasiparticle number measured by the junctions is 15 million. If we consider a factor of 2 of backtunneling, the total excess quasiparticles in the two junctions are about 8 million. For the photon event in the center, each junction collects 4 million quasiparticles. These 4 million quasiparticles eventually tunnel through the junction and flow into the wiring pad. Then the quasiparticle density in the wiring pad becomes $4\times10^6 / 1.90\times10^4 \mu m^3$ = $211/ \mu m^3$. (We didn't count the thermal loss in the Al trap). From the experimental data the tail starts at about 17~20 nA for device C and three times smaller for device B, which is close to the thermal subgap current of the junctions. So the estimated magnitude of the tails is consistent with what we observed.

We have clearly explained the origin of the long decays or the tails of the pulses. They are caused by the narrow lead that constrains the quasiparticle out-diffusion from the wide wiring pad region. This has been a very interesting phenomenon observed in our experiment. However their very existence limits the effective count rate of our detectors. One way to solve the problem is to keep the width of the wiring pad and the lead width the same. If we want to improve the quasiparticle out-diffusion and reduce the backtunneling, we can even make the lead width larger than the wiring pad width.

Chapter 8 Other Device Issues and Perspectives

Besides the device issues that we have extensively discussed in Chapter 4 and Chapter 5, there are other issues that also deserve some brief discussion. Substrate x-ray absorption events introduce quasiparticles into the Ta absorber film. These unaccounted for quasiparticles cause some energy noise broadening and degrade the detector performance. The energy resolution of the lateral backtunneling device is briefly analyzed here to reveal that its performance is limited by the fluctuation of thermal quasiparticles and quasiparticle self-heating effects in the junction.

8.1 The Effects of Substrate Events

A substrate event happens when an x-ray photon gets absorbed in the Si substrate and is detected by the Al junctions. In fact, because of the small area and the thinness of the Ta absorber film, most x-ray photons land on the silicon chip and are absorbed in the substrate. The phonons created by the x-ray absorption in the substrate can break Cooper pairs and generate quasiparticles in the Ta absorber and Al junctions. Since most of the x-ray photon energy is dissipated in the Si substrate, the total charge generated by the substrate event is less than that by direct absorption in the Ta absorber or in the Al junctions. In Fig. 4.11 we can find many substrate events sparsely distributed below the K_α line. For events that are right underneath the absorber most of the photon energy will be collected by the absorber and detected by the junctions. As the events occur further away from the absorber, the amplitude of the signals changes as a function of the inverse of the distance.

Because the substrate events are randomly distributed in time, any time overlap between the direct x-ray photon absorption by the absorber and the substrate event can add charge fluctuation to the measurement. This effect becomes more significant as the count rate of the detector increases. The higher the radiation rate of the source or the count rate of the detector, the more chances the substrate events will overlap with the actual signal, and the larger the charge effects. Therefore the substrate events impose constraints on the maximum possible count rate of the detector.

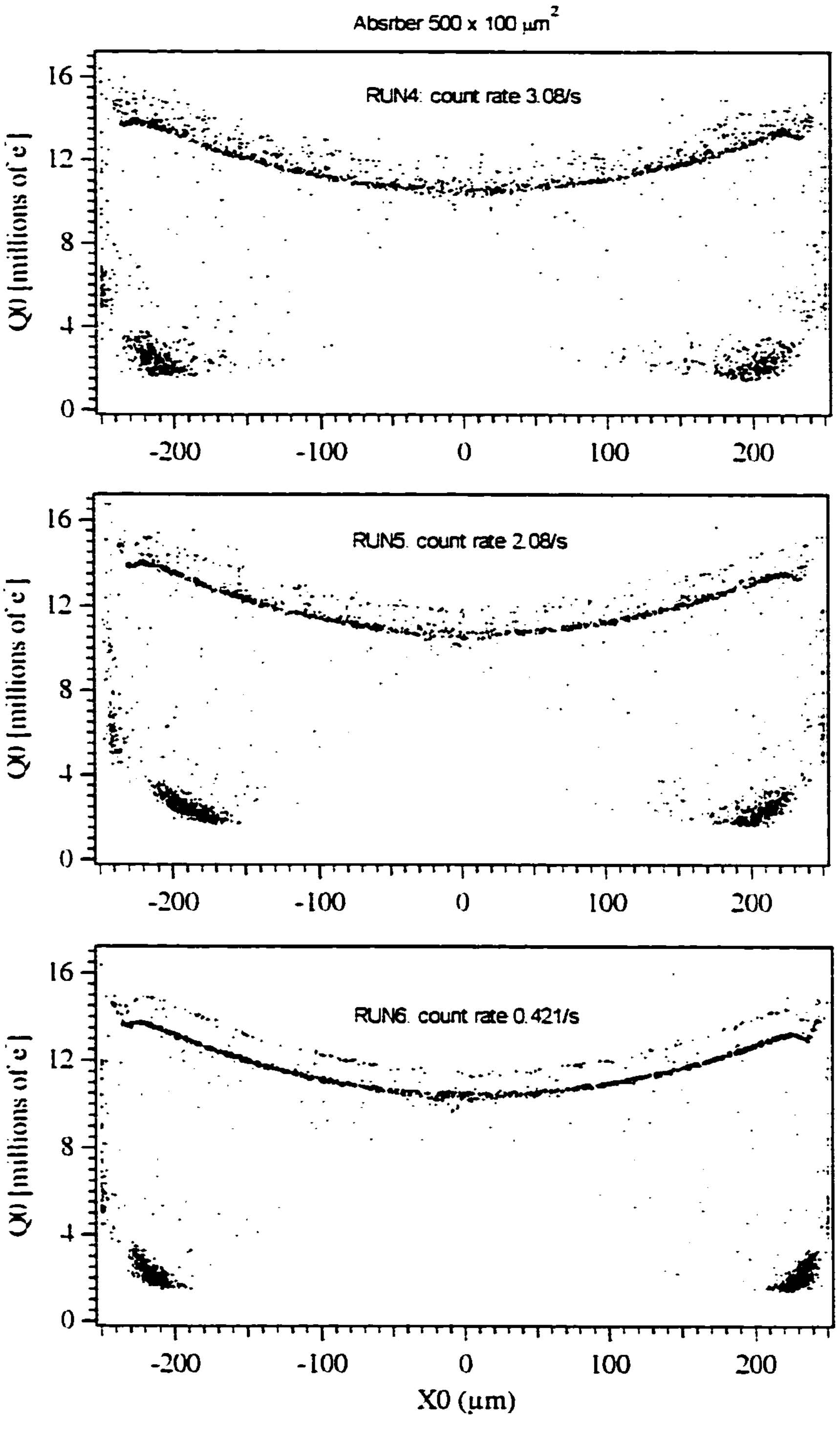

Fig. 8.1 Total charge as a function of location for the 500 μm long device with different count rates. The pulse length is 200 μs including a 50 μs pretriggered baseline. The numbers of x-ray events are the same for the three plots. And the trigger levels are the same too. (device F. 3/6/01)

The energy resolution of the 500 μm device has been measured for different count rates to study the effects of the substrate events. Fig. 8.1 shows the total collected charge as a function of the location under different count rates without filtering, i.e., the full 200 μs long pulses are integrated to obtain the charges. When the count rate is relatively high (the top panel), the K_β line is almost indistinguishable from the K_α line without filtering the signals. As the count rate decreases by one order of magnitude, we can clearly distinguish the K_α line from the K_β line.

The energy resolution of the device can be analyzed to quantitatively study the substrate effect. In doing the energy resolution analysis, we cut the pretriggered baselines (40 μs) and the tails of pulses (60 μs) so that only the central 100 μs pulses are kept to have large signal to noise ratio. Fig. 8.2 shows the square of the energy resolution as a function of the count rate. The energy resolution is calculated from the x-ray events in the -150 to -100 μm region. We assume that the square of the energy resolution is proportional to the count rate (see Appendix D), and ***ΔE^2/Count rate*** ~ $(36.5\ \mathrm{eV})^2$/s (per count rate) is calculated from the slope of the linear fit.

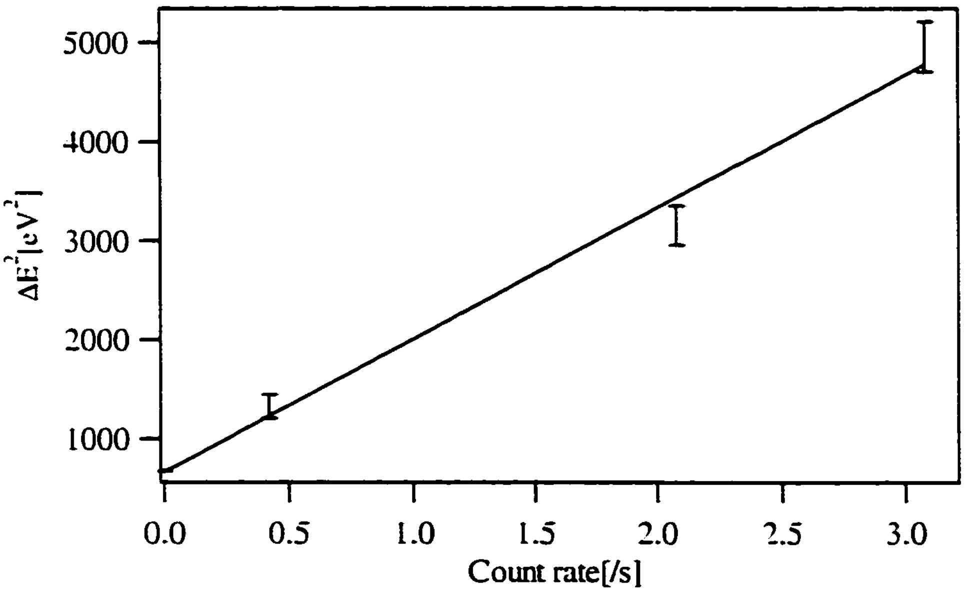

Fig. 8.2 ***ΔE^2*** as a function of the count rate for the 500 μm device without filtering. (device F, 3/6/01)

The substrate event effects can also be shown in the charge histograms. In Fig. 8.3 we compare the charge histograms of device B with that of the 500 μm long device. All x-ray events are included in the histogram without filtering. Most substrate events of device B create less than 1 million quasiparticles in the Ta absorber so they are not noticeable at all. But the number of quasiparticles created by the substrate events of the 500 μm device can reach 4 million to create a fat tail on the low energy side of the histogram.

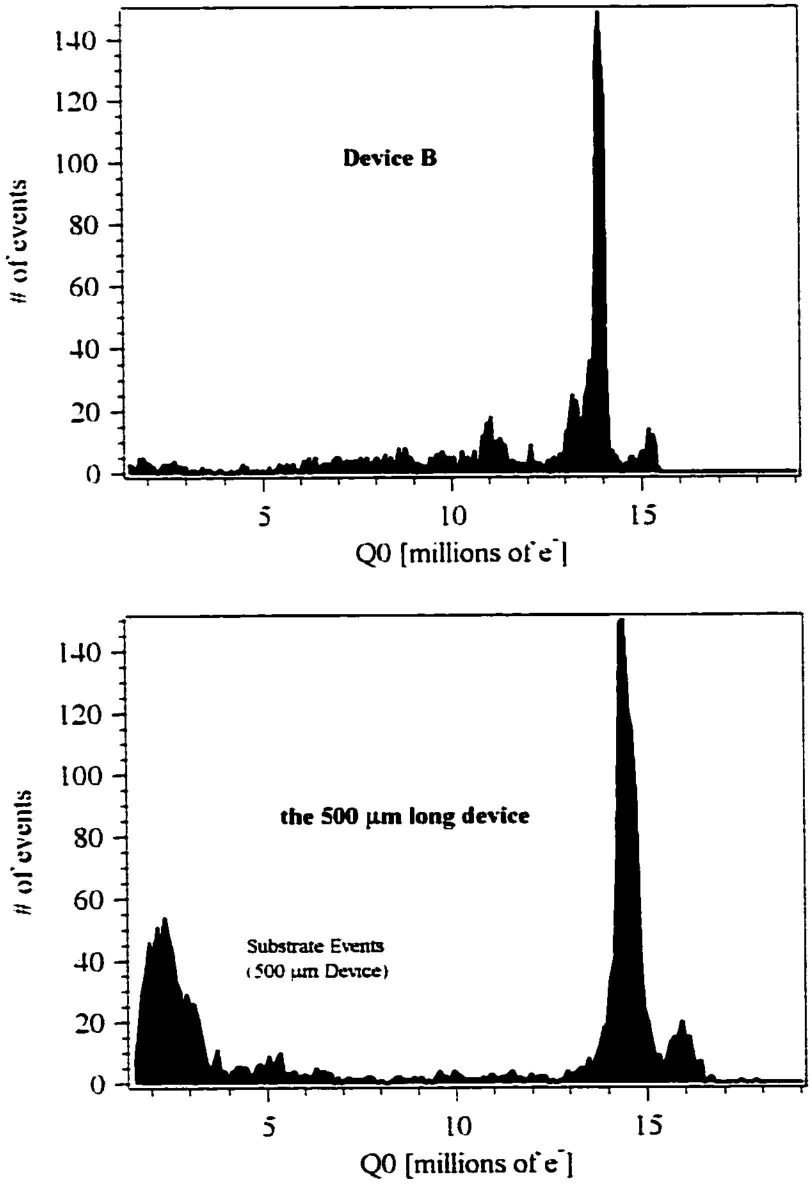

Fig. 8.3 The charge histogram of device B and the 500 μm device (device F) along the whole absorber without filtering. (device B, 6/4/00; device F, 3/6/01)

The major difference between device B and the device F is the thickness of the buffer layer between the absorber and the Si substrate. The SiO_2 layer for device B is 6000Å compared to 3000Å for the 500 μm long device. This suggests that the suppression of the substrate events in device B might be due to the thicker SiO_2 layer. Since the substrate events are substantially suppressed in device B, the energy resolution of device B does not change much as a function of the count rates as the 500 μm long device does.

How low should the count rate of the x-ray source be so that the substrate event effects can be regarded negligible? It depends on three parameters: (a) the energy broadening due to the substrate events, (b) the pulse length, (c) the coupling strength of substrate events to the Al junction.

The energy broadening due to the substrate events should be much smaller than the broadening caused by other noise sources so that its effect can be negligible. For example, a 13 eV energy resolution with an error bar of 1 eV, the energy broadening due to the substrate events should be less than $\sqrt{13^2-12^2}=5$ eV. If a 6 keV x-ray photon creates 5 million quasiparticles, the 5 eV energy broadening means that the charge fluctuation caused by the substrate events should be about 4×10^3 quasiparticles.

The pulse length determines the overlapping probability of the substrate events. For the 500 μm long device the pulse length is 100 μs. To avoid overlapping the count rate of substrate events should be less than $1/(10\times100\ \mu s)=1000s^{-1}$. The Ta absorber has a absorption area of $500\times100\ \mu m^2$. The absorption efficiency for it is 28%, while that for the Si substrate is almost 100%. With a measured 3 photon events occurring in the Ta absorber every second, the rate of x-ray events in the substrate within a 1 mm range from one of the Al junctions will be about $1000s^{-1}$. If the substrate events farther than the 1 mm range can still couple to the Al junction and generate charge fluctuation of about 4×10^3 quasiparticles, they will add more energy broadening to the measurement.

The coupling strength of the substrate events to the Al junction determines how far away the substrate events can affect the device performance. The onset charge of the substrate events is about 4 million quasiparticles for device F as shown in Fig. 8.3. However, for device B and C the onset charge is below 1 million quasiparticles and for device A it is about 1.2 million quasiparticles. The smaller coupling strength of the Si substrate and Al junction in device A may be due to its narrow wiring pads and leads compared to that of device E, which are 78 μm wide. Therefore, device F with the 500 μm long absorber shows a stronger coupling between the substrate events and the Al junction than device A, B and C. In Ref. [Friedrich, 97], the collected charge of the substrate events as a function of distance from the junction was studied for device A. With the onset charge of 1.2 million quasiparticles for device A, the substrate events as far as 700 μm away from the Al junctions can still create a charge fluctuation of more than 10^4 quasiparticles. Because the onset charge for device F is 4 million quasiparticles, its coupling range can reach as far as 2 mm. This roughly explains why we observed the significant substrate events in device F. The coupling between the Si substrate events and the Al junction was also studied in Ref. [Cabrera, 96]. They fabricated two sets of QETs (quasiparticle-trap-assisted electrothermal-feedback transition-edge-sensors) 5 mm apart on a 1cm × 1cm × 1mm Si crystal. The QETs can easily detect the 6 keV x-ray photon 5 mm away. If an x-ray event is close to one QET and ~5 mm away from the other QET, the ratio of the energy collected by these two junctions is 4:1 with Au heat sink around the Si wafer and 5:2 without heat sink. The collected energy is reduced by the heat sink on the Si wafer, which is caused by the reduction of the phonon lifetime in the Si crystal. More information on the phonon lifetime in the Si crystal is needed in order to more quantitatively study the substrate events.

Based on the above discussions, there might be several ways to minimize the effects of the substrate events. (1) We can decrease the x-ray count rate of the detector to reduce the chance of time overlapping between the real signals and the substrate events signals. (2) We can use a mask to shield the substrate and only open a window on the device. The mask is supposed to be thick enough to prevent x-ray photons from being absorbed in the substrate. (3) We can use a thicker buffer layer to separate the substrate and the absorber so that the phonons generated in the substrate have less chance to couple to the device. Other groups have tried to use different type of buffer layers instead of thicker SiO_2 to reduce the substrate events [Angloher, 00]. Some even build devices on membranes to completely remove the substrate under the absorber [Irwin, 99]. In real astronomical applications, a high count rate is a necessity so that we must better separate the substrate from the absorber or use masks.

8.2 Backtunneling Device

Backtunneling devices with a stack structure have been used by many groups [Frank. 96: Verhoeve. 98]. The typical structure of such a device is either Nb-Al-AlOx-Al-Nb or Ta-Al-AlOx-Al-Ta. Fig. 8.4 shows the energy diagram as well as the cross-sectional view for three types of devices: (1) stack backtunneling, (2) lateral backtunneling, and (3) non-backtunneling devices. In the backtunneling devices, once the quasiparticles are trapped in the Al junction region they can tunnel and backtunnel many times until they recombine into Cooper pairs or escape from the Al traps with energy higher than the absorber gap energy. The multiple tunneling of the quasiparticles increases the measured charge.

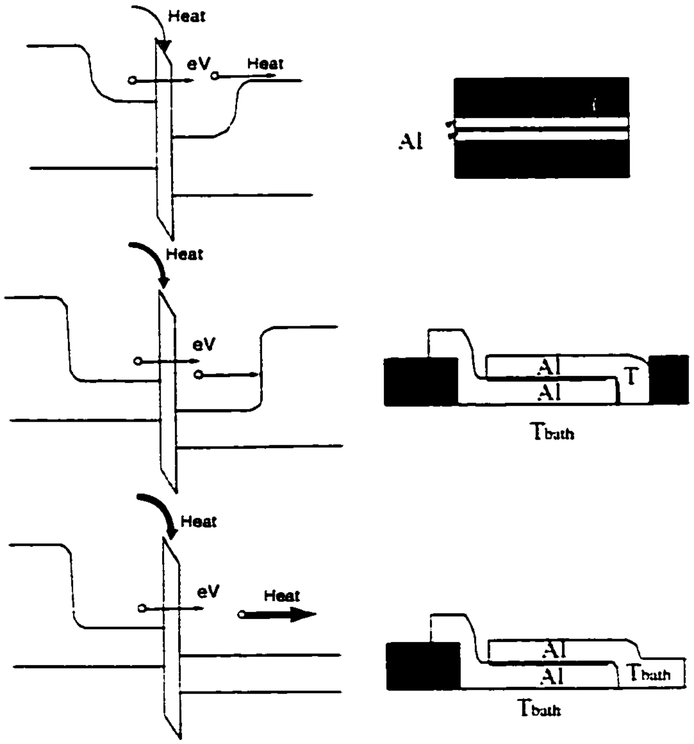

Fig. 8.4 The energy diagrams and cross sections of the stack backtunneling device, lateral backtunneling device and non-backtunneling device.

In the stack structure, the thin layer of the Al trap accelerates the tunneling and increases the current signal since the tunneling rate is inversely proportional to the volume of the trap. Even though the backtunneling process brings with it the backtunneling noise, the stack backtunneling device is still a very good detector when the noise is dominated by electronic noise. The Al film in the stack backtunneling device is proximitized because the Al film in the junction is very thin compared to the Nb or Ta absorber. The trap barrier in the stack backtunneling devices is thus shallower than the lateral backtunneling devices. Though a considerable portion of the quasiparticles in the stack structure will recombine into Cooper pairs, some quasiparticles can still tunnel out of the junction area. While in the lateral structure, the barriers formed by the Ta absorber on the two sides are high enough to confine the quasiparticles in the Al junction area to make it almost impossible for quasiparticles to escape the junction region.

The best energy resolution of Nb based STJ detectors was actually achieved by using stack backtunneling devices [Frank, 96]. But can the backtunneling device with a lateral structure provide similar benefits as the stack backtunneling device? In Ref. [Segall, 00b], it is expected that the lateral backtunneling device can achieve 10 eV energy resolution. The two main assumptions behind this prediction were: (1) the backtunneling device could give a charge gain of n by quasiparticles that multiple-tunnel n times, (2) the charge noise due to the long integration time of the electric current noise increases by $\sqrt{n}$. One more implicit assumption is that the electronic noise is much larger than the intrinsic backtunneling noise. With these three assumptions, the signal to noise ratio is supposed to be increased by $\sqrt{n}$ due to the backtunneling.

Some preliminary investigation on the lateral backtunneling device was performed [Segall, 00b]. It was found that the I-V curve didn't follow the BCS prediction. The device behaved like a resistor as can be seen in Fig. 8.5 where the current almost increases linearly with the voltage. The data can be well fitted by a self-heating model Eq. (7.5). The dynamic resistance was about 100 Ω which is much smaller than the dynamic resistance for the device without backtunneling. Both the subgap current and the dynamic resistance give a lot of electronic noise. It has been demonstrated that the linear I-V curve is not an accidental phenomenon caused by trapped flux or stray photons. Rather, it is intrinsic to the lateral backtunneling device structure [Wilson, 01].

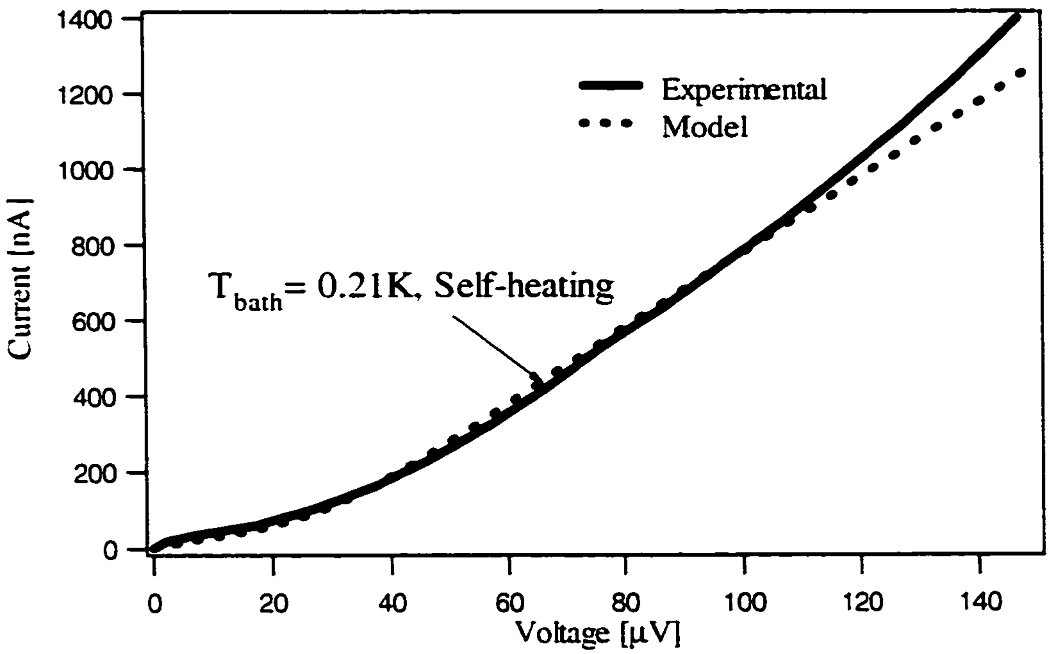

Fig. 8.5 The I-V curve of the x-ray backtunneling device. The model (dashed line) compares well with the experimental data (solid line). The resistance like I-V curve is caused by heating the constrained quasiparticles in the junction region by the Ta plug. Both the subgap current and the voltage noise due to the small dynamic resistance become dominant noise sources of the device. (Experimental data, [Segall, 00b])

We now believe the resistor-like behavior of the I-V curve is caused by the heating of the confined quasiparticles in the Al junction region. When the tunnel junction is voltage biased, the electrical power flowing into the Al junction is IV. For each tunneling event, the quasiparticle gains an energy of eV. Since the quasiparticles are constrained in the junction region by the Ta plug, they cannot leave the junction region by the normal outdiffusion process until they recombine into Cooper pairs and the emitted phonons escape into the substrate without breaking Cooper pairs. So the gained energy by quasiparticles through tunneling can only be dissipated in the Al junction region.

There are two sources that create quasiparticles in the superconductor quasiparticle system. The first one is the thermal quasiparticle creation by phonons at the bath temperature T_{bath}. This process keeps the quasiparticle system in equilibrium with the bath. The second source is the quasiparticle creation by the absorbed electrical power IV.

The only way for the quasiparticles to disappear is to recombine into Cooper pairs. Therefore the change of the number of quasiparticles $N(t, T, V)$ in the Al junction is

$$\frac{dN(t,T,V)}{dt} = -\frac{RN(t,T,V)^2}{Vol} + P_{therm}(T_{bath}) + f_{create}(I(T,V),V). \tag{7.1}$$

where R is the recombination rate. Vol is the volume of both electrodes in between the Ta absorber and the Ta plug. $P_{therm}(T_{bath})$ is the thermal quasiparticle creation rate and related to the bath temperature T_{bath} by

$$P_{therm}(T_{bath}) = \frac{RN(T_{bath})^2}{Vol}. \tag{7.2}$$

This form is exactly the same as the quasiparticle recombination rate except that the temperature is now the bath temperature T_{bath}. $f_{create}(I(T,V),V)$ is the quasiparticle creation rate caused by the absorbed electrical power.

For devices without backtunneling or with a low backtunneling barrier (see Fig. 8.4), the generated heat can be carried away by the relatively fast quasiparticle outdiffusion process. Thus, the junction will cool down quickly and the heating effect can be neglected. The condition for ignoring the heating effect is that $f_{create}(I(T,V) \approx 0,V)$ is small compared to other terms in (7.1). If the heating effect can be ignored, the quasiparticles in the junction region are considered to be in thermal equilibrium with the bath and the subgap thermal quasiparticle current follows the BCS theory of Eq. (2.14).

For the backtunneling device, $f_{create}(I(T,V),V)$ cannot be ignored anymore. Furthermore, it increases with bias voltage. The higher the bias voltage, the higher the electrical power is injected into the Al junction region. The increase of $f_{create}(I(T,V),V)$ leads to a higher temperature in the quasiparticle system and more quasiparticles $N(T)$. Let's assume that the electronic power injected into the quasiparticle system is proportional to

$$\frac{c_{qp}}{c_{qp}+c_{ph}} = \frac{e^{-\Delta/kT}}{e^{-\Delta/kT}+C_0T^3}, \tag{7.3}$$

where c_{qp} and c_{ph} are the heat capacity of the quasiparticle system and phonon system (which also includes the substrate), respectively, C_0 is a fitting parameter. Then we have

$$f_{create}(I(T,V),V) = \frac{I(T,V)V}{e\Delta}\frac{e^{-\Delta/kT}}{e^{-\Delta/kT}+C_0T^3}. \tag{7.4}$$

By substituting Eq. (7.2) and (7.4) into Eq. (7.1) and assuming a steady state, i.e., $dN(t,T,V)/dt = 0$, we have

$$-\frac{RN(T,V)^2}{Vol}+\frac{RN(T_{bath})^2}{Vol}+\frac{I(T,V)V}{e\Delta}\frac{e^{-\Delta/kT}}{e^{-\Delta/kT}+C_0T^3}=0. \qquad (7.5)$$

If we assume the quasiparticles still follow the Fermi distribution, $N(T,V)$ and $I(T,V)$ can be calculated as a function of the temperature T from BCS theory. From Eq. (7.5) we can then calculate the tunneling current as a function of the bias voltage V. Fig. 8.5 shows the simulation obtained from this procedure and comparison with the experimental data. The model and experiment are in quite good agreement. The model describes well the resistive behavior of the device.

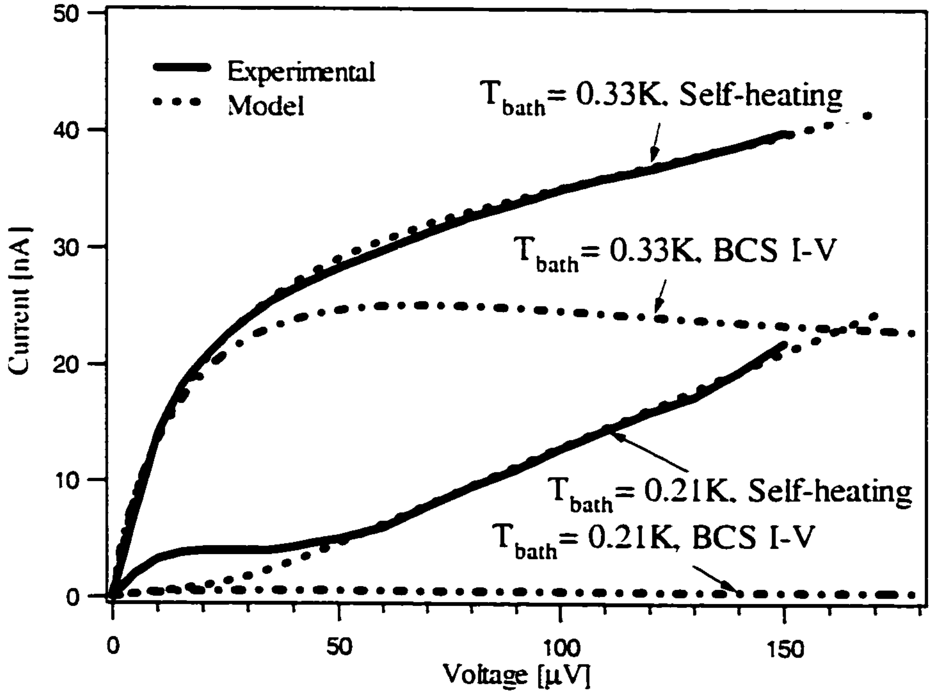

Fig. 8.6 The macroscopic model of the self-heating I-V curves of the UV-optical backtunneling device at two different temperatures compared with BCS theory. The experimental data (solid lines) [Wilson, 02] compare well with the model (dashed line).

We can further check this model against a UV-optical backtunneling device [Wilson. 02]. We first fit the self-heating model to the experimental I-V curve at T_{bath}= 0.21 K and V_{bias} > 50 μV to determine the constant C_0. Then we calculate the self-heating I-V curve at T_{bath}= 0.33 K. Fig. 8.6 shows the simulation results for the UV optical devices at different temperature and compared with experimental data. Again, the model is shown with dashed lines, while the experimental data are shown with solid lines. It is quite clear that the BCS theory cannot be used to describe the behavior of the device at bias voltage higher than 50 μV. The self-heating model not only describes well the high bias voltage portion of the curve, it also fits the data down to very low voltages for the T_{bath} = 0.33 K case. In the T_{bath} = 0.21 K case, there is some discrepancy between the model and the data in the low voltage region, that may be caused by residual Josephson current.

Due to the heating effect, even as the bath temperature goes to zero, the tunneling current $I(T= 0, V)$ does not go to zero as predicted by the BCS theory. The finite subgap current causes a large shot noise. The small dynamic resistance increases the noise contribution from the voltage noise of the amplifier to a very high level. These noise sources can become dominant and put new limits on the detector performance.

It is also shown that other than the thermal heating there is a fluctuation of thermal quasiparticles proportional to n instead of $\sqrt{n}$ [Wilson, 01]. If this is true, the signal to noise ratio will not have any improvement from the backtunneling device even without the heating effect.

Considering the self-heating effect and the fluctuation of the thermal quasiparticles, the lateral backtunneling devices are no longer ideal candidates for further improvements.

The reason that other groups use stack structure backtunneling devices is because the Al trap reduces the tunneling time and increases the signal. The proximitized Al trap also reduces the quasiparticle loss in the Nb or Ta absorber. The heating effect is less dramatic for the stack structure device because the proximitized Al layer has a much higher energy gap than the pure Al gap energy. The quasiparticles with higher energy can escape from the junction and carry away some heat. By finding the proper thickness of the Al layer, the stack structured backtunneling detector performance can be optimized.

8.3 Controlled Out-Diffusion

In Chapter 7 we gave an explanation of the long decays of the pulses. They are caused by the narrow lead that constrains the quasiparticle out-diffusion from the wide wiring pad region. To eliminate the long decays we can keep the width of the lead the same as the width of the wiring pad. If we want to improve the quasiparticle out-diffusion and reduce the backtunneling, we can even make the lead width larger than the wiring pad width.

On the other hand we can also control the out-diffusion or backtunneling by the wiring design. In section 8.2, we talked about the backtunneling device. The performance of those backtunneling devices is constrained by the self-heating effect and the thermal quasiparticle fluctuation noise [Wilson, 01]. In those devices, the quasiparticles are constrained in the junction region until they are recombined. The technique found in Chapter 7 can be used in the UV-Optical STJ detectors to control the quasiparticle backtunneling. By optimizing the charge gain and thermal fluctuation noise, hopefully the energy resolution of the optical backtunneling devices can be improved.

8.4 STJ Detectors Perspective

Since STJ detectors research started more than ten years ago, there has been enormous improvement on these detectors in terms of energy resolution as well as imaging capabilities. But there is still much room for improvement. So what will the next generation Ta based STJ detectors look like?

The present dominant noise source originates from incomplete quasiparticle cooling. The solution to this is to bias the junction at high voltage and increase the tunneling time. To increase the tunneling time, we must use the junction geometry design that was discussed in Chapter 4. However there is an upper limit to the bias voltage for the Al STJ detectors. The subgap current has a sharp increase at the bias voltage of Δ/e due to the two particle tunneling process [Schrieffer, 63]. At finite temperature, the subgap current for Al junctions begins to increase rapidly when the bias voltage increases to 150 μV. The bias voltage of device A, B, and C is limited by first Fiske mode. In Chapter 4 the design of a diamond shaped junction geometry can completely eliminate Fiske modes in the subgap energy region. So the bias voltage can be improved from 130 μV to 150 μV. But the margin of improvement remains relatively small.

In Chapter 4, we also showed that device B has better quasiparticle cooling. But because of its small trap volume self-recombination becomes a large source of noise. To test this idea, we designed device E with twice the trap volume of device A but the same junction area. Preliminary tests show the energy resolution can be improved from 26 eV to 18 eV with feedback resistor $\boldsymbol{R_f}$ operating at room temperature. We expect device E with $\boldsymbol{R_f}$ cooled down to 1.5 K to achieve comparable energy resolution to device B. Because the junction area is large, the shot noise of device E will be twice as large as device B. To further improve device E, we can try cooling device E down to even lower temperature such as 0.1K to further reduce shot noise. Here are several possible improvements for future STJ detector developments.

1. Using a large trap volume and cooling the device down to 0.1K

A device with 5 times the trap volume can reduce the noise due to the incomplete quasiparticle cooling. Since the long tunnel time could also cause more thermal quasiparticle loss in the Al trap, the device has to be cooled down to a lower temperature such as 0.1 K to minimize the thermal loss and shot noise contributions. We expect the subgap current to be reduced by a factor of about 10. The predicted performance of such devices operating at 0.1K is compared with device B in Table 8-1. In this table, the voltage noise and the bias-voltage fluctuations for the suggested device are estimated from the simulations in Chapter 5. The estimated current noise is projected from the measurement results of the existing devices. The quasiparticle thermal loss with a long tunnel time of 12.5 μs at 0.1 K is calculated using the recombination rate measured from the experiments. Since the device structure is still the same as device B, we assume the same noise contribution caused by absorber loss and trapping multiplication.

2. Using a normal metal on top of the Al wiring pad

In Table 8-1, we can see that the backtunneling noise is one of the largest noise sources for device B. One way to attack this problem is to put a normal metal on the top of the wiring pad near the junction as a quasiparticle trap to accelerate the outdiffusion and reduce the backtunneling. This idea needs further experimental exploration.

Energy width - ΔE	**device B** **ΔE [eV]** **τ_{tun}=5.0μs(0.21K)**	**device(large trap)** **ΔE [eV]** **τ_{tun}=12.5μs (0.1K)**
Predicted Device noise		
Creation	2.9	2.9
Absorber Loss	~ 0	~ 0
Trapping Multiplication	3.6	3.6
Backtunneling	4.8	(normal metal) ~0
Cancellation	2.5	1.2
Self-recombination (and thermal loss in Al)	5.3	~0
Sum	**8.9**	**4.77**
Amplifier -related noise		
Current noise	4.2	2.4
Voltage noise	5.3	3.6
Bias-Voltage fluctuations	3.5	1.83
ΔE_{Total} predicted	**12.0**	**6.7**

Table 8-1 The prospective energy resolution of the Ta based STJ detectors due to changing the trap volume of junctions and lowering the device temperature.

3. Using epitaxial Ta films to increase the diffusion constant

The maximum dimension of the Ta absorber is constrained by the small quasiparticle diffusion constant and the short quasiparticle lifetime. Using epitaxial Ta films can make the quasiparticle diffusion process faster. Using a thicker Ta absorber can increase the quasiparticle lifetime. Both ways may enlarge the maximum dimension of the device to meet the requirement for astronomy applications.

4. Using shielding mask to prevent substrate events and increase the count rate

The intrinsic energy resolution of the Ta based STJ detectors is around 5 eV for 6 keV x-ray photons. The advantage of STJ detectors compared to bolometers is their capability of handling a fast count rate. Since the count rate of our detector is limited by the substrate events, shielding mask can be used to eliminate the substrate events and thus increase the count rate.

Appendix A: Device Parameters

	Device A (XN93)	Device B (F99-11C)	Device C (F99-13C)
Dimensions:			
Ta absorber area [μm^2]	200×100	200×100	200×100
Al trap [μm^3]	700	517	839
Al junction [μm^2]	1860	620	1860
CE+ wiring [μm^3]	2800	9133	9133
Fabrications:			
Ta absorber [Å]	6000	5700	5700
Nb contact [Å]	2000	2400	N/A
Al trap [Å]	1500	2100	2100
Al counterelectrode [Å]	700	800	800
SiO via [Å]	1500	2700	2700
Al wiring [Å]	3000	3650	3650
SiO_2 [Å]	3000	6000	6000
Electrical:			
R_{NN} [Ω]	0.5	1.4	0.4
I_c [μA]	500	205	675
I_{bias} [nA]	25	9	25
R_{dyn} [kΩ]	10	>50	10
Pulse Fits:			
τ_{trap} [ns]	10	--	--
D [cm^2/s]	8.5	--	--
τ_{loss} [μs]	30	--	--
Q_0 [millions of e]	8.0	--	--
τ_{tun} [μs]	2.5	5.0	2.5
τ_{out} [μs]	7.1	--	--

	Device E (H00-6C)	Device F (H00-3C)	Device G (H00-2C)
Dimensions:			
Ta absorber area [μm^2]	200×100	500×100	1000×100
Al trap [μm^3]	1944	972	972
Al junction [μm^2]	2025	2025	2025
CE+ wiring [μm^3]	6804	6804	6804
Fabrications:			
Ta absorber [Å]	6000	6000	6000
Nb contact [Å]	2000	2000	2000
Al trap [Å]	1400	1400	1400
Al counterelectrode [Å]	1200	1200	1200
SiO via [Å]	2400	2400	2400
Al wiring [Å]	3000	3000	3000
SiO_2 [Å]	3000	3000	3000
Electrical:			
R_{NN} [Ω]	0.43	0.43	0.43
I_c [μA]	620	630	650
I_{bias} [nA] at 100 μV	18	18	20
R_{dyn} [kΩ] at 100 μV	>50	>28	>24
Pulse Fits:			
τ_{trap} [ns]	10	10	10
D [cm^2/s]	8.0	8.3	8.0
τ_{loss} [μs]	87	83	78
Q_0 [millions of e]	8.1	7.6	7.4
τ_{tun} [μs]	6.8	3.4	3.4
τ_{out} [μs]	11	16	17

Appendix B: Summary of Important Runs

Date	**Device**	**Summary**
04/03/00	Device B	First test of device B in the shielded box. The magnetic field applied by the superconducting coil was very stable. Observed x-ray pulses with long decay time.
04/20/00	Device B	First time successfully used laser detrapping setup to remove trap flux from the junction in the x-ray measurement. It dramatically improved the experiment efficiency.
04/28/00	Device B	Cooled the device for two hours after the detrapping and the device showed a very good performance with ΔE=18 eV.
05/11/00	Device B	Measured x-ray pulses with different voltage bias from 40 μV to 130 μV and collected some important information to study the quasiparticle cooling in the junctions.
05/26/00	Device B	First time successfully used cold R_f for both junctions. The energy resolution was ΔE=22 eV.
06/02/00	Device B	Continued the test of device B with cold R_f. The energy resolution was ΔE=14~15 eV.
06/04/00	Device B	Continued the test of device B with cold R_f. The energy resolution was ΔE=13eV.
06/06/00	Device B	Did injection test to measure the energy broadening caused by the quiescent electronic noise.
07/26/00	Device C	First test of device C with a Ta contact with R_f at room temperature. There is no extra energy broadening in the center of device C. It proved that Nb caused the excess energy broadening in the center of the device B. The magnitude of long pulse decay of device C is larger than that of device B.
07/31/00	Device C	First test of device C with cold R_f. The energy resolution was ΔE = 26 eV, which is consistent with our expectation. The energy resolution along the whole absorber is comparable to that of device B. Device C significantly improved the spatial uniformity of the energy resolution throughout the absorber.
10/16/00	Annular Junction	First test of the annular junction. X-ray photon measurement was done with normal procedure by applying magnetic field
10/26/00	Annular Junction	Successfully trapped one flux quanta. The trapped fluxon greatly suppressed Josephson *dc* current. Successfully measured x-ray photons without external magnetic field.
11/18/00	Device B	Measured the energy broadening due to the voltage noise during the x-ray pulses.
12/22/00	Device C	Repeated test, the energy resolution was ΔE = 26.7 eV.
01/01/01	Device E	First test of the diamond shape junctions. This kind of junctions do not have Fiske mode below Al energy gap. It has a large trap volume and therefore better quasiparticle cooling. It showed ΔE

		= 19 eV with warm R_f. Observed substrate event effects too.
02/27/01	Device F	Measured the 500 μm long absorber device. The goal of the measurement was to study quasiparticle diffusion constant and quasiparticle lifetime.
03/06/01	Device F	Studied the substrate event effects by measuring the energy resolution as a function of count rate.
03/19/01	Device G	Measured the 1000 μm long absorber device to continue the study of quasiparticle non-equilibrium dynamics in the Ta absorber. Device E, F and G didn't have long decay as Device B and C did, but they showed substrate event effects.

Appendix C: Related Experimental Data Analysis

In this appendix some experimental data related to the wiring events of device B and C are shown.

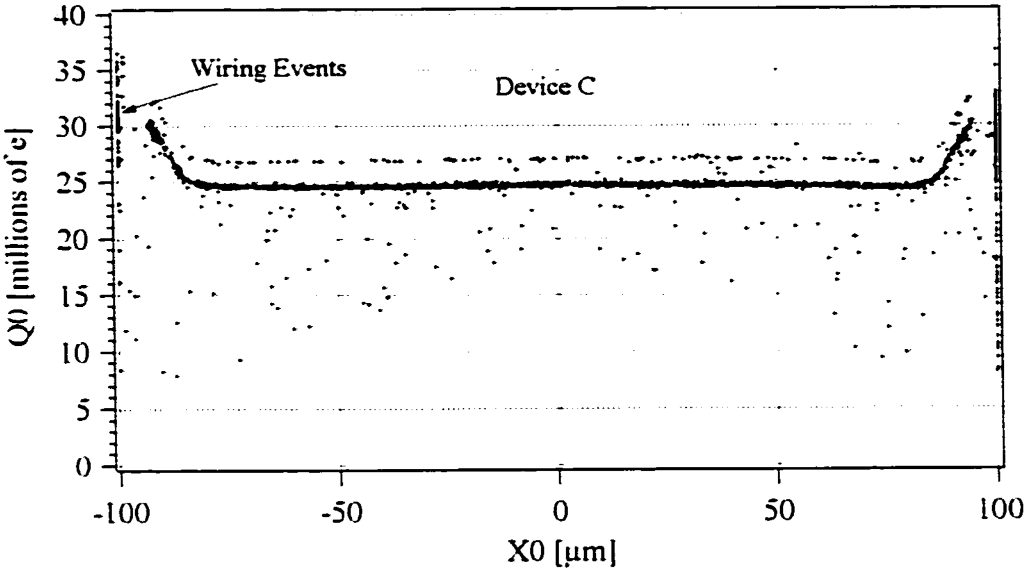

Fig. C.1 The total collected charge vs. the x-ray event location for device C without filter.

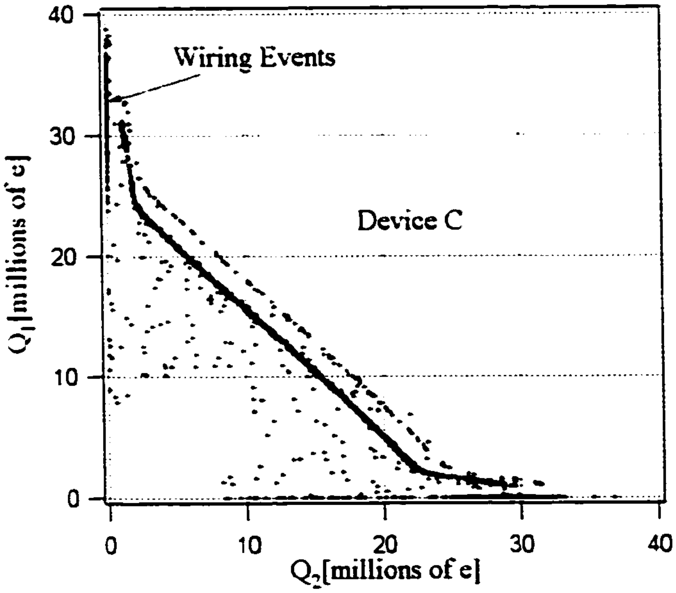

Fig. C.2 Q_1 vs. Q_2 of device C without filtering.

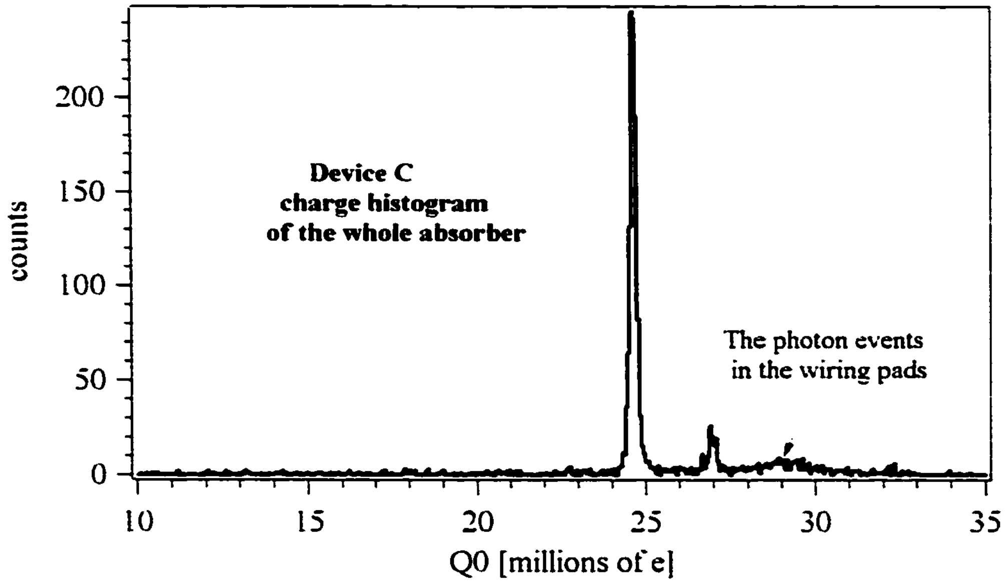

Fig. C.3 Charge histogram of device C through the whole absorber. The charge of the wiring events is about 29 millions of e.

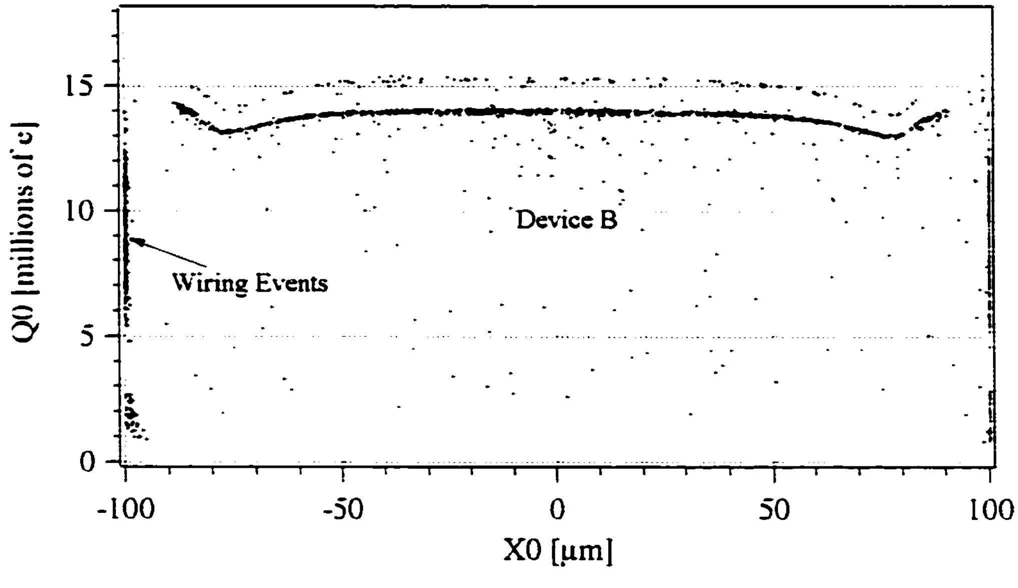

Fig. C.4 The total collected charge vs. the x-ray event location for device B without filter.

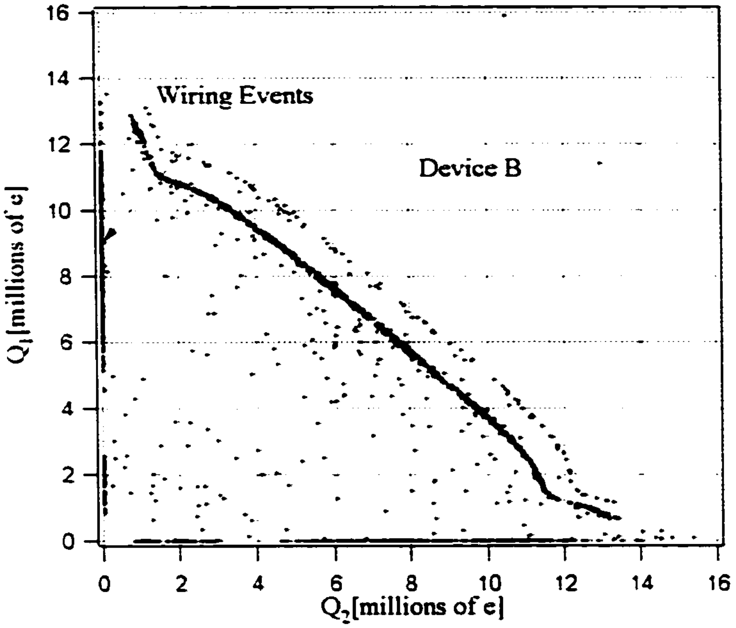

Fig. C.5. Q_1 vs. Q_2 of device C without filtering.

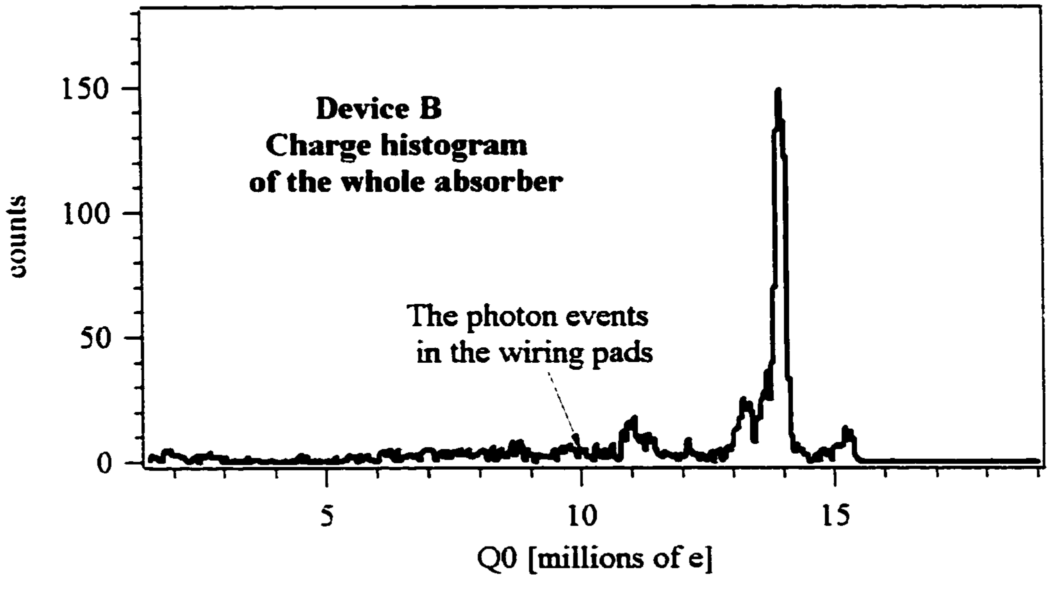

Fig. C.6. Charge histogram of device C through the whole absorber. The charge of the wiring events is about 29 millions of e.

The total charge difference between device B and C without filtering is due to the long decay of the pulses discussed in Chapter 7. The charge of the photon events in the wiring pad of device C is about three times of that of device B. The total charge decrease at two ends in device B is due to quasiparticle self-recombination.

Appendix D: Substrate Event Effect and Count Rate

In this appendix we use a very simple model to study the energy broadening caused by substrate events as a function of count rate. We make two assumptions: (a) the time interval between the pulses absorbed in the Ta absorber is the same. (b) the substrate events are very short (they either overlap with real pulses or not) and the collected charge is the same and very small. If the probability of substrate events overlapped with the real pulse is p. The number of substrate events per unit time overlapped with the real pulse follows the binomial distribution. If the count rate of the substrate events is n_{sub}, which is proportional to the count rate of the real absorber events n, the fluctuation of the overlapped substrate events is $\sigma_{n_{sub}}^2 = n_{sub} p(1-p) \propto np(1-p)$. The energy broadening caused by the substrate events is proportional to fluctuation of the overlapped substrate events, therefore it is proportional to the square root of the count rate ($\Delta E \propto \sigma_{n_{sub}} \propto \sqrt{n}$) under our simple assumptions.

However the real situation is much more complicated than this model. First the real absorber events are randomly distributed in time. The magnitude of the substrate events decreases with the distance from the junction, but the number of the substrate events increase with the distance. Our empirical analysis in Section 8.1 only shows the general effect of the substrate events to the energy resolution.

Bibliography

1. [Ambegaokar, 63] V. Ambegaokar, A. Baratoff, *Phys. Rev. Lett.* **10**, 486, 1963.

2. [Angloher, 00] G. Angloher, B. Beckhoff, M. Buhler, F.V. Feilitzsch, T. Hertrich, P. Hettl, J. Hohne, M. Huber, J. Jochum, R.L. Mossbauer, J. Schnagl, F. Scholze and G. Ulm, *Nucl. Instru. Meth.*, **A444**, 214, 2000.

3. [Angloher, 01] G. Angloher, P. Hettl, M. Huber, J. Jochum, F. v. Feilitzsch and R. L. Mossbauer, *J. Appl. Phys.* **89,** 1425, 2001.

4. [Bardeen, 57] L. Bardeen, L.N. Cooper, J. Schrieffer, *Phys. Rev.* **108**, 1175, 1957.

5. [Barone, 82] A. Barone and G. Paterno, "Physics and Applications of the Josephson Effects", Wiley, New York, 70-95, 1982.

6. [Bostock, 76] J. L. Bostock, M.L. Vicar, "Anisotropy effects in superconductors," Plenum Press, New York, 1977.

7. [Booth, 87] N.E. Booth, *Appl. Phys. Lett.* **50**, 293, 1987.

8. [Cabrera, 96] B. Cabrera, *Nucl. Instrum. Meth.* **A370**, 150, 1996

9. [Charles, 95] P.A. Charles and F. C. Steward., Exploring the X-ray Universe, Cambridge University Press, 1995.

10. [Chervenak, J.] J.A. Chervenak, et al., *Appl. Phys. Lett.* **74**, 4043, 1999.

11. [Cristiano, 95] R. Cristiano, E. Esposito, L. Frunzio, S. Pagano, L. Parlato, G. Peluso, G. Pepe, U. Scotti di Uccio, H. Nakagawa, M. Aoyagi, H. Akoh, S. Takada, *Appl. Phys. Lett.* **67**, 3340, 1995.

12. [Cristiano, 99] R. Cristiano, E. Esposito, L. Frunzio, M. P. Lisitskii, C. Nappi, G. Ammendola, A. Barone, L. Parlato, D. V. Balashov, V. N. Gubankov, *Appl. Phys. Lett.* **74**, 3389,1999.

13. [de Gennes, 64] P.G. De Gennes, *Rev. Mod. Phys.* **36**, 225, 1964.

14. [den Hartog, 00] R. den Hartog, P. Verhoeve, N. Rando, A. Peacock, M. Krumrey and D.J. Goldie, Proceedings of the 8th international workshop on low temperature detectors, *Nucl. Instr. Meth.* **A444**, 278, 2000.

15. [den Hartog, 02] R. den Hartog, A. Kozorezov, D. Martin, G. Brammertz, P. Verhoeve, A. Peacock, F. Scholze, D.J. Goldie, *Ninth international workshop on low temperature detectors*, F. S. Porter, et al. Ed., Wisconsin. 11, 2002.

16. [den Hartog, 02] R. den Hartog, A. Kozorezov, J.K. Wigmore, P. verhovev, D. Martin, A. Peacock, *Ninth international workshop on low temperature detectors*, F. S. Porter, et al. Ed., Wisconsin, 35, 2002.

17. [Eck, 65] R.E. Eck, D.J. Scalapino and B.N. Taylor. Proc. 9th Intl. Conf. On Low Temp. Phys., ed J.G. Daut, New York: Plenum, 415, 1965.

18. [Eisenmenger, 81] W. Eisenmenger, "Nonequilibrium Phonons," Chapter 3 in K.E. Gray, ed., "Nonequilibrium Superconductivity, Phonons, and Kaptiza Boundaries, New York: Plenum Press, 1981.

19. [Face, 87] D.W. Face, D.E. Prober, *J. Appl. Phys.* **62**, 3257, 1987.

20. [Fano, 47] U. Fano, *Phys. Rev.* **72**, 26, 1947.

21. [Fiske, 64] M.D. Fiske, *Rev. Mod. Phys.* **36**, 221, 1964.

22. [Frank, 96] M. Frank, C.A. Mears, S.E. Labov, F. Azgui, M.A. Lindeman, L.J. Hiller, H. Netel, A. Barfknecht, *Nucl. Instrum. Meth.* **A370**, 41, 1996.

23. [Friedrich, 97a] S. Friedrich, K. Segall, M.C. Gaidis, C.M. Wilson, D.E. Prober, P.J. Kindlmann, A.E. Szymkowiak, S.H. Moseley, *IEEE Trans. Appl. Supercond.* **7**, 3383, 1997.

24. [Friedrich, 97b] S. Friendrich, Ph.D. Thesis, Yale University, 1997.

25. [Friedrich, 97c] S. Friedrich, K. Segall, M.C. Gaidis, C.M. Wilson, D. E. Prober, A.E. Szymkowiak and S.H. Moseley, *Appl. Phys. Lett.* **71**, 3901, 1997.

26. [Friedrich, 02] S. Friedrich, T. Niedermayr, T. Funk, O. Drury, M.L. van den Berg, M.F. Cunningham, J.N. Ullom, A. Loshak, S.P. Cramer, M. Frank, S.E. Labov, *Ninth international workshop on low temperature detectors*, F. S. Porter, et al. Ed., Wisconsin, 359, 2002.

27. [Frunzio, 01] L. Frunzio, L. Li, D.E. Prober, I.V. Vernik, M.P. Lisiskii, C. Nappi and R. Christiano, *Appl. Phys. Lett.* **79**, 2103, 2001.

28. [Gaidis, 93] M.C. Gaidis, S. Friedrich, D.E. Prober, S.H. Moseley and A.E. Szymkowiak, *IEEE Trans. Appl. Supercond.* **3**, 2088, 1993.

29. [Gaidis, 94] M.C. Gaidis, Ph.D. thesis, Yale University, 1994.

30. [Gaidis, 96] M.C. Gaidis, S. Friedrich, K. Segall, D.E. Prober, S.H. Moseley and A.E.Szymkowiak, *IEEE Trans. Appl. Supercond.* **6**,1, 1996.

31. [Gijsbertsen, 95] J.G. Gijsbertsen, E. P. Houwman, B. G. Klopman, J. Flokstra, H. Rogalla, D. Quenter, S. Lemke, *Physica* **C249**, 12, 1995.

32. [Goldie,1994] D.J. Goldie, P.L. Brink, N.E. Booth and G.L. Salmon, *Appl. Phys. Lett.* **64**, 954, 1994.

33. [Gray, 71] K.E. Gray, *Journ. Phys. F: Metal Phys.* **1**, 290, 1971.

34. [Gubrud, 01] M.A. Gubrud, M. Ejrnaes, A. J. Berkley, R.C. Ramos, Jr., I. Jin, J.R. Anderson, A. J. Dragt, C.J. Lobb and F. C.Wellstood, *IEEE Trans. Appl. Supercond.* **11**, 1002, 2002.

35. [Halbritter, 87] J. Halbritter, *J. Appl. Phys.* **A 43**, 1, 1987.

36. [Hilton, 99] G.C. Hilton, D.A. Wollman, K.D. Irwin, L.L. Dulcie, N. Bergren, and J.M. Martinis, *IEEE Trans. Appl. Supercond.* **9**, 3177, 1999.

37. [Irwin, 98] K. Irwin, G. Hilton, D. Wollman, J. Martinis, *J. Appl. Phys.* **83**, 3978, 1998.

38. [Irwin, 99] K.D. Irwin, G.C. Hilton, J.M. Martinis, S. Deiker, N. Bergren, S.W. Nam, D.A. Rudman, D.A. Wollman, *Nucl. Instru. Meth.*, **A444**, 184, 1999.

39. [Jochum, 93] J. Jochum, H. Kraus, M. Gutsche, B. Kemmather, F.v.Freilitzsch, R. L. Mossbauer, *Ann. Physik* **2**, 611, 1993.

40. [Josephson, 62] B.D. Josephson, *Phys. Rev. Lett.* **1**, 251, 1962.

41. [Kaplan, 76] S.B. Kaplan, et al., *Phys. Rev.* **B14**, 4854, 1976.

42. [Kikuchi, 00] K. Kikuchi, H. Myoren, T. Iizuka, S. Takada, *Appl. Phys. Lett.* **77**, 3660, 2000.

43. [Kraus, 89] H. Kraus, F. v. Freilitzsch, J. Jochum, R. L. Mossbauer, T. Peterreins, F. Probst, *Phys. Lett.* **B 321**, 195, 1989.

44. [Kurakado, 82] M. Kurakado, *Nucl. Instru. Meth.* **A196**, 275, 1982.

45. [Labov, 98] S. Labov, M. Frank, J.B. le Grand, M. Linderman, H. Netel, L. Hiller, D. Chow, S. Friedrich, C. Mears, G. Caldrara, A. Barfknecht, Proc. LTD7, 82, 1998.

46. [Le Grand, 97] J.B. le Grand, J. Martin, R.P. Huebener, A.W. Hamste, G.C.S. Brons and J. Flokstra, *J. Appl. Phys.* **81**, 7413, 1997.

47. [Li, 00] L. Li, L. Frunzio, K. Segall, C.M. Wilson, D.E. Prober, A.E. Szymkowiak and S. H. Moseley, *Nucl. Instr. Meth.* **A444**, 228, 2000.

48. [Li, 01a] L. Li, L. Frunzio, C.M. Wilson, K. Segall, D.E. Prober, A.E. Szymkowiak and S. H. Moseley, *IEEE Trans. Appl. Supercond.* **11,** 685, 2001.

49. [Li, 01b] L. Li, L. Frunzio, C.M. Wilson, D.E. Prober, A.E. Szymkowiak and S.H. Moseley, *J. Appl. Phys.*, **90**, 3645, 2001.

50. [Li, 02a] L. Li, L. Frunzio, C.M. Wilson, K. Segall, D.E. Prober, A.E. Szymkowiak and S.H. Moseley, *Proc. 9th Int. Workshop of Low Temperature Detectors*, AIP Conference Proceedings **605**, 145, 2002.

51. [Li, 02b] L. Li, L. Frunzio, C.M. Wilson, D.E. Prober, accepted by *J. Appl. Phys.*.

52. [McCammon, 91] D. McCammon, W. Cui, M. Juda, P. Plucinski, J. Zhang, R.L. Kelley, S.S. Holt, G.M. Madejski, S.H. Moseley, A.E. Szymkowiak, *Nuclear Physics A. Proc.* PANIC XII, **A527**, 821, 1991.

53. [Mears, 93] C.A. Mears, S.E. Labov, A.T. Barfknecht, *Appl. Phys. Lett.* **63**, 2961, 1993.

54. [Mears, 96] C.A. Mears, S.E. Labov, M. Frank, M.A. Lindeman, L.J. Hiller, H. Netel, A. Barfknecht, *Nucl. Instrum. Meth.* **A370**, 53, 1996.

55. [Nappi, 96] C. Nappi, R. Cristiano, L. Frunzio, S. Pagano, M. P. Lisitskii, *J. Appl. Phys.* **80**, 3401, 1996.

56. [Nappi, 97] C. Nappi and R. Cristiano, *Appl. Phys. Lett.* **70**, 1320, 1997.

57. [Nappi, 97] C. Nappi, *Phys. Rev.* **B 55**, 82 ,1997.

58. [Nappi, 98] C. Nappi, R. Cristiano and M.P. Lisitskii, *Phys. Rev.* **B58**, 685, 1998.

59. [Narayamurti, 78] V. Narayanamurti, R.C. Dynes, P. Hu, H. Smith and W.F. Brinkman, *Phys. Rev.* **B 16**, 6041, 1978.

60. [Poelaert, 99] A. Poelaert, A.K. Kozorezov, J.K. Wigmore, A. Peacock, *Phys. Rev. Lett.* **82**,1257, 1999.

61. [Peterson, 91] R.L. Peterson, Cryogenics **31**, 132, 1991.

62. [Press, 92] W.H. Press, S.A. Teukolsky, W.T. Vetterling and B.P. Flannery, *Numerical Recipes in C*, 2nd Edition, Cambridge University Press.

63. [Pressler, 00] H. Pressler, M. Ohkudo, M. Koike, M. Ukibe, T. Zama, T. Nakamura and M. Katagiri, *Appl. Phys. Lett.* **77**, 4055, 2000.

64. [Rando, 98] N. Rando, et al., Proc. SPIE 3445-25, 1998.

65. [Radparvar, 95] M. Radparvar, Cryogenics **35**, 535-540, 1995. The standard HYPRES Nb process flow and design rules are available via the HYPRES Inc. website: http://www.hypres.com.

66. [Segall, 99] K. Segall, C.M. Wilson, L. Li, A.K. Davies, R. Lathrop, M.C. Gaidis, D.E. Prober, A.E. Szymkoviak and S.H. Moseley, *IEEE Trans. on Appl. Supercond.* **9**, 3326, 1999.

67. [Segall, 00a] K. Segall, C.M. Wilson, L. Frunzio, L. Li, S. Friedrich, M.C. Gaidis, D.E. Prober, A.E. Szymkoviak, and S.H. Moseley, *Applied Physics Letters* **76**, 3998, 2000.

68. [Segall, 00b] K. Segall, Ph.D. thesis, Yale University, 2000.

69. [Shreiffer, 63] J.R. Schrieffer and J.W. Wilkins, *Phys. Rev. Lett.* **10**, 17, 1963.

70. [Tinkham, 96] M. Tinkham, *Introduction to Superconductivity*, 2nd Edition, McGraw-Hill, Inc, New York, 1996.

71. [Tobochnik, 89] J. Tobochnik, *Computers in Physics*, **3-4**, 181, 1989.

72. [Tucker, 01] W. Tucker and K. Tucker, *Revealing the Universe, the making of the Chandra x-ray observatory*, Harvard U. Press, 2001.

73. [Van Duzer, 81] T. Van Duzer and C.W. Turner, *Principles of Superconductive Devices and Circuits*, New York, Elsevier, 1981.

74. [Verhoeve, 98] P. Verhoeve, N. Rando, A. Peacock, A. van Dordrecht, B.G. Taylor, and D.J. Goldie, *Appl. Phys. Lett.* **72**, 3359, 1998.

75. [Vernik, 96] I.V. Vernik, N. Lazarides, M.P. Soerensen, A.V. Ustinov, N.F. Pedersen, V.A. Oboznov, *J. Appl. Phys.* **79**, 7054, 1996.

76. [Wilson, 00] C.M. Wilson, K. Segall, L. Frunzio, L. Li, D.E. Prober, D. Schiminovich, B. Mazin, C. Martin, R. Vasquez, *Nucl. Instrum. Meth.* **A444**, 449, 2000.

77. [Wilson, 01] C.M. Wilson, L. Frunzio, D.E. Prober, *Phys. Rev. Lett.* 87, 067004, 2001.

78. [Wilson, 02] C.M. Wilson, Ph.D thesis, Yale Uniersity, 2002.